3-2021

Cislunar Debris Propagation Following a Catastrophic Spacecraft Mishap

Nathan R. Boone

CISLUNAR DEBRIS PROPAGATION FOLLOWING A CATASTROPHIC SPACECRAFT MISHAP

THESIS

Nathan R. Boone

AFIT-ENY-MS-21-M-289

DEPARTMENT OF THE AIR FORCE
AIR UNIVERSITY

AIR FORCE INSTITUTE OF TECHNOLOGY

Wright-Patterson Air Force Base, Ohio

AFIT-ENY-MS-21-M-289

CISLUNAR DEBRIS PROPAGATION FOLLOWING A CATASTROPHIC SPACECRAFT MISHAP

THESIS

Presented to the Faculty

Department of Aeronautics and Astronautics

Graduate School of Engineering and Management

Air Force Institute of Technology

Air University

Air Education and Training Command

In Partial Fulfillment of the Requirements for the

Degree of Master of Science in Astronautical Engineering

Nathan R. Boone, B.S.

March 2021

AFIT-ENY-MS-21-M-289

CISLUNAR DEBRIS PROPAGATION FOLLOWING A CATASTROPHIC SPACECRAFT MISHAP

Nathan R. Boone, B.S.

Approved:

_____	_____
Robert A. Bettinger, Maj, USAF (Chairman)	Date
_____	_____
Bryan Little, Lt Col, USAF (Member)	Date
_____	_____
Joshuah Hess, Maj, USAF (Member)	Date
_____	_____
William Wiesel, Ph.D (Member)	Date

AFIT-ENY-MS-21-M-289

Abstract

This research involves theoretical analysis of the short- and long-term motion of space debris in cislunar trajectories following a spacecraft catastrophic mishap. Specifically, the research formulates a debris propagation model using four-body dynamics and determines debris trajectories following breakup events for a variety of different initial orbital positions. A spacecraft survivability model is then used to quantify the risks from the debris to other cislunar spacecraft. First, a study of the risks due to natural debris comprising the Kordylewski clouds at the Earth-Moon L_4 and L_5 Lagrange points is conducted as an introduction to cislunar debris propagation. Next, five artificial cislunar debris case studies are examined, which include the study of catastrophic spacecraft mishaps at the collinear Earth-Moon Lagrange points L_1 and L_2, during an Apollo-like Earth-Moon transfer, during a transfer between L_1 and Earth along the L_1 manifold, at the stable Lagrange points L_4 and L_5, and in lunar orbit. Risks to current operational spacecraft near Earth were found to be greatest for the Apollo-like transfer case study, and slight risks to spacecraft in cislunar orbits were found for the other case studies. The L_4 and L_5 points were found to be vulnerable to debris accumulation in the studies of mishaps at L_4 and L_5, and debris that circulates cislunar space indefinitely is the primary risk resulting from mishaps at L_1, L_2, and in the L_1 manifold. Overall, research into cislunar debris propagation enhances operational planning outside the traditional near-Earth paradigm of spacecraft mission operations and increases understanding of the debris-related consequences of mishaps within this orbital regime.

Acknowledgments

First, I would like to thank my research advisor, Maj. Bettinger, for his guidance and expertise. I greatly appreciate his help in selecting a fascinating research topic, teaching me how to conduct research, and encouraging me to publish my research.

I would like to thank my employer for providing me with the opportunity to pursue a degree at AFIT.

I would also like to thank my family and Xiuhan for their support during my academic pursuits.

Nathan R. Boone

Table of Contents

Page

List of Figures

Page

List of Tables

Page

List of Symbols

Roman

Symbol	Meaning
a	Distance between Earth-Moon barycenter and Earth
b	Distance between Earth-Moon barycenter and Moon
C	Jacobi Constant
E	Expected number of hits to a spacecraft
G	Gravitational Constant
H	Hamiltonian
$\hat{\mathbf{i}}$, $\hat{\mathbf{j}}$, $\hat{\mathbf{k}}$	Basis vectors of the Earth-Moon rotating frame
$\hat{\mathbf{I}}$, $\hat{\mathbf{J}}$, $\hat{\mathbf{K}}$	Basis vectors of the Sun-Earth-Moon inertial frame
M	Number of particles in Danger Zone
r	Radius
T	Kinetic Energy
t	Time, with epoch when the Sun, Earth, and Moon are all in a line
U	Modified Potential Energy
V	Potential Energy
ΔV	Change in velocity, Delta-v
v or v_R	Speed in the Earth-Moon rotating frame
x, y, z	Components in the Earth-Moon rotating frame

Greek

Symbol	Meaning
β	Ratio of solar radiation pressure to the gravitational force
μ	Constant equal to the mass of the Moon as a fraction of the total Earth-Moon mass, 0.01215
ρ	Density of particles within the Danger Zone
ω or ω_2	Angular velocity of the Earth-Moon rotating frame

Subscript Characters

Symbol	Meaning
A_1	Distance from the Sun to the Sun-Earth-Moon barycenter
A_2	Distance from the Sun-Earth-Moon barycenter to the Earth-Moon barycenter
a_S	Distance from the Earth-Moon barycenter to the Sun
L_1, L_2, L_3	Collinear (or Unstable) Lagrange points
L_4, L_5	Triangular (or Stable) Lagrange points
m_E	Mass of Earth
m_M	Mass of Moon
m_S	Mass of the Sun
m_{sc}	Mass of spacecraft
$N_{particles}$	Number of simulated particles
p_x, p_y, p_z	Components of momenta in the Earth-Moon rotating frame
P_{HZ}	Probability of hazard
P_K	Probability of kill
$P_{K\|H}$	Probability of kill with a hit
$\left(P_{K\|H}\right)_{max}$	Maximum possible probability of kill with a hit
P_S	Probability of survival
R^2	Coefficient of determination
$R_{initial}$	Scale factor for randomly generated initial conditions
$\vec{r}_E$	Radius vector from Earth-Moon barycenter to Earth
r_{ij}	Radius from i to j
$\vec{r}_M$	Radius vector from Earth-Moon barycenter to Moon
r_{sc}	Radius vector from the Earth-Moon barycenter to the spacecraft
t_0	Simulation start time
t_f	Simulation end time
v_R or v	Speed in the rotating Earth-Moon reference frame
V_S	Penetrator Spray (Danger Zone) Volume
$\vec{v}_{sc}$	Velocity of spacecraft in inertial frame
x_E, y_E, z_E	Coordinates of the Earth in Earth-Moon rotating frame
x_M, y_M, z_M	Coordinates of the Moon in the Earth-Moon rotating frame
x_S, y_S, z_S	Coordinates of the Sun in the Earth-Moon rotating frame
Z_i	Random number generated from the standard normal distribution
ρ_E	Distance from spacecraft to Earth
ρ_M	Distance from spacecraft to Moon
ρ_S	Distance from the spacecraft to the Sun
$\rho_{initial}$	Initial number density of particles in the simulated Kordylewski clouds
ω_1	Angular velocity of the Earth-Moon barycenter about the Sun-Earth-Moon barycenter
ω_2 or ω	Angular velocity of the Earth-Moon rotating frame

List of Acronyms

Acronym	Meaning
ASAT	Anti-Satellite
BCR4BP	Bi-circular Restricted Four-Body Problem
CR3BP	Circular Restricted Three-Body Problem
DU	Distance Unit
ECI	Earth-Centered Inertial
EGO	Eccentric Geophysical Observatory
GEO	Geostationary Orbit
JPL	Jet Propulsion Laboratory
LEO	Low Earth Orbit
LOI	Lunar Orit Insertion
LOP-G	Lunar Orbital Platform-Gateway
NRHO	Near Rectilinear Halo Orbit
RCS	Radar Cross Section
TEI	Trans-Earth Injection
TLE	Two-Line Element set
TLI	Trans-Lunar Injection
TU	Time Unit
USAF	United States Air Force
ZVC	Zero Velocity Curves

CISLUNAR DEBRIS PROPAGATION FOLLOWING A CATASTROPHIC SPACECRAFT MISHAP

I. Introduction

1.1. Background and Motivation

The United States Air Force (USAF) has increasingly expressed interest in the strategic opportunities presented by space between the Earth and the Moon. This space, known as cislunar space[1], offers to serve as a new "high ground" for space operations, allowing a positional and logistic advantage over other space-based assets. This interest is partially driven by recent international activity in cislunar space, such as the Chinese Chang'e-4 far-side Moon mission and the Queqiao relay satellite orbiting the Earth-Moon L_2 Lagrange point. China eventually intends to industrialize the Moon to make economic use of its resources, potentially creating an enormous advantage to Chinese operations in the cislunar region. Military competition in cislunar space is likely to increase the number of spacecraft operating in this region [1].

As more spacecraft operate in cislunar space, a catastrophic spacecraft mishap in this region becomes more likely, with each mishap generating a significant number of debris fragments. Many studies have investigated the threat of debris events in lower Earth orbits. These concerns have grown with recent anti-satellite (ASAT) tests performed by China in 2007 [2] and by India in 2019 [3], which generated debris clouds that continue to threaten

[1] The term "cislunar" refers to the spatial toroidal volume (approximately) extending from geosynchronous Earth orbit to and encompassing the Moon and its orbit. By comparison, the term "translunar" refers to specific trajectories and/or missions between the Earth and Moon. For the present research, "cislunar" will be used exclusively in conjunction will all analysis showcased herein.

other spacecraft. Several satellites have also suffered failures that led to breakup events, including the NOAA 16 weather satellite in 2015, the U.S. Air Force's Defense Meteorological Satellite Program (DMSP) satellite in 2016, and the Japanese Hitomi spacecraft in 2016 [4]. The 2009 collision of Cosmos 2251 and Iridium 33 also created two large fragment clouds [4]. These fragmentation events could lead to a cascading series of collisions, eventually leaving certain orbits so full of debris that they are unusable, a phenomenon known as "Kessler Syndrome" [5].

While the threat of debris in orbits near Earth has been heavily studied, few prior studies have investigated the effects of a debris event in cislunar space. The unique dynamics of this environment make it difficult to predict the motion of the debris over time. Namazyfard [6] discussed the effects of lunisolar perturbations on the Eccentric Geophysical Observatory (EGO) satellite, which was launched in 1964 and expected to return to Earth in 16 years but remains in space over 50 years later. This demonstrates the difficulties in properly modeling the perturbations in cislunar space, and the potentiality for objects to remain there indefinitely under certain conditions.

A catastrophic spacecraft mishap in cislunar space could pose risks to other operational spacecraft by creating a cloud of debris particles that intersect much lower orbits. For the present research, a "mishap" represents a battery explosion that causes a complete omni-directional breakup of the spacecraft into debris fragments. Bandyopadhyay, Sharma, and Twari [7] studied the effects of a fragmentation event near the collinear (unstable) Earth-Moon L_1 and L_2 Lagrange points. They found that for both points about 2% of the fragments intersected geosynchronous altitude, posing a small but measurable risk to other

spacecraft. Catastrophic spacecraft mishaps for spacecraft in other types of cislunar orbits could pose similar risks to operational spacecraft in lower orbits.

Similar to observed natural phenomena, debris particles produced by a catastrophic spacecraft mishap may begin to "pool" in certain orbits in cislunar space, potentially creating significant debris hazards in those orbits. Several papers have investigated the existence of "Kordylewski Clouds," which are accumulations of cosmic dust that have been observed near the stable Earth-Moon Lagrange points L_4 and L_5. The dynamics of these clouds could provide clues about the behavior of debris following a catastrophic spacecraft mishap and may suggest debris risks to spacecraft operating near these points. Slíz-Balogh, Barta, and Horváth noted in their study of the Kordylewski clouds that rock-sized particles should be able to circulate in the vicinity of the L_5 Lagrange point for a long time [8]. If debris from mishaps in cislunar space begins to collect near the stable Lagrange points, then it could threaten the ability for current and future space missions to take advantage of these useful locations.

1.2. Research Objectives

1.2.1. Thesis Prospectus

This research involves theoretical analysis to entail the short- and long-term modeling of space debris in cislunar trajectories following a catastrophic spacecraft mishap. Specifically, the research formulates a debris propagation model using four-body dynamics and determines the debris density at various time periods following the breakup event for both different initial orbital positions and total fragment number. For various initial orbit scenarios, the survivability of spacecraft relative to a catastrophic mishap is also

determined. Overall, research into cislunar debris propagation will enhance operational planning outside the traditional near-Earth paradigm of spacecraft mission operations and the debris-related consequences of mishaps within this orbital regime.

1.2.2. Research Objectives

- Generate cislunar spacecraft trajectories, first by ignoring the effects of solar gravity by solving the Circular Restricted Three-Body Problem (C3RBP), and then by including the effects of solar gravity by solving the Bi-circular Restricted Four-Body Problem (BCR4BP).
- Extend the trajectory model from a single spacecraft to a system of particles, each with variable initial velocities, and observe the trajectories at different propagation time snapshots.
- Determine the properties of a catastrophic spacecraft mishap in terms of number of particles generated, the size of the particles, and the ΔV imparted to each particle.
- Simulate the motion of particles resulting from a spacecraft catastrophic mishap in cislunar space over the following days and months. Repeat the simulation for different pre-explosion cislunar mission trajectories and locations along the trajectories and observe any intersections of the resulting particle orbits with the orbits of other spacecraft.
- Determine the long-term trajectories of the particles and analyze the possible effects on spacecraft that reside near these trajectories.
- Analyze the survivability of spacecraft moving in the debris field.

1.2.3. Research Questions

- What is the influence of solar gravity on cislunar trajectories?
- What are the effects of the initial pre-explosion spacecraft trajectory on the debris distribution?
- Will the debris particles intersect any orbits with notional operational spacecraft?
- How will the cislunar debris particles behave over the long-term? Will the particles end up "settling" into a particular obit? If so, do current or planned operational spacecraft reside in this orbit?
- What is the probability of survivability for an operational cislunar spacecraft when moving in the debris field or when impacted by one or more of these debris fragments?

1.3. Methodology

The motion of objects in cislunar space is determined using a trajectory model that incorporates the gravitational influences of the Earth, Moon, and Sun. The gravitational influence of the Sun is first neglected by solving the Circular Restricted Three-Body Problem (CR3BP), then incorporated by solving the Bi-circular Restricted Four-Body Problem (BCR4BP). After the trajectories of cislunar debris particles have been determined, a spacecraft survivability model is applied to examine the threats resulting from the debris particles to notional spacecraft operating elsewhere in cislunar space.

1.3.1. The Circular Restricted Three-Body Problem

The problem of determining the motion of a small object moving under the gravitational influence of two massive bodies is of particular interest in the Earth-Moon system. The

CR3BP may be used to model the motion, under the assumptions that the mass of the object is negligible compared to the two massive bodies and that the massive bodies move in coplanar circular orbits about their barycenter with a constant angular velocity [9]. These assumptions are valid for a small spacecraft moving in the Earth-Moon system. Unfortunately, unlike the two-body problem, the CR3BP has no analytical solution, and the trajectory must be determined using numerical integration techniques. Trajectories are also highly sensitive to initial conditions, and small changes in the initial conditions can produce large differences in motion over time. However, this added complexity over the two-body model provides a more accurate model of the dynamics in cislunar space. The CR3BP also provides insight into the Lagrange equilibrium points, locations where a spacecraft can remain fixed in a rotating reference frame due to the balance of gravitational forces between two bodies, and stable manifolds that can provide efficient transfers to the Moon. The features of the CR3BP dynamics are discussed in detail in Chapter III.

1.3.2. The Bi-circular Restricted Four-Body Problem

Although the CR3BP provides accurate results for many applications, it does not incorporate the gravitational influence of the sun, which can be an important consideration. As the distance from the Earth increases, the relative gravitational influence of the sun increases [6]. This perturbation could be especially significant over long time periods, so for this research, the effect of solar gravity is considered. The BCR4BP is an extension of the CR3BP that incorporates solar gravity. This problem is used to describe a spacecraft of negligible mass that moves under the gravitational influence of the Earth, Moon, and Sun. The Earth and Moon revolve in circular orbits about their barycenter, which revolves in a circular orbit about the Sun-Earth-Moon barycenter as shown in Figure 1. In many

formulations of this problem, the motion of the three massive bodies is assumed to be in the same plane. The BCR4BP problem was first studied in 1960 by Huang [10], and has been used by Koon [11] for cislunar trajectory generation, by Davis et al. [12] and Boudad [13] in studies of debris in lunar halo orbits, and by Salnikova [14] for modeling the Kordylewski clouds. A discussion of Kordylewski clouds is given in Chapter II, and the equations of motion for the BCR4BP are developed in Section 3.3.

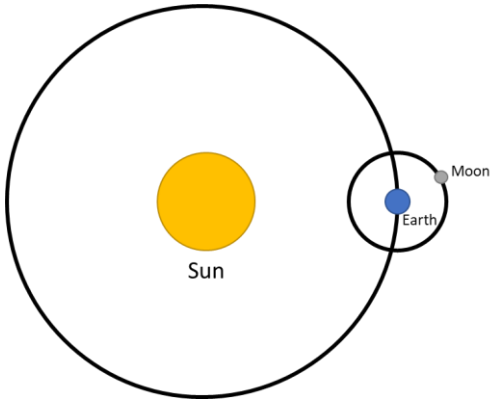

Figure 1. Bi-circular Four-Body Model (Spacecraft Not Shown)

1.3.3. Spacecraft Survivability

Application of a spacecraft survivability model enables a quantification of the risks resulting from the cloud of debris. The probability that a spacecraft will be threatened by debris depends on both the density of the debris cloud and the expected amount of damage that would be caused by particle impacts. In Section 3.5, these factors are combined in a probabilistic spacecraft survivability model. This survivability model is a variation of the Poisson model commonly used for aircraft survivability analysis.

1.4. Thesis Overview

Chapter I has provided the motivation for this research and outlines the research objectives. Chapter II reviews existing literature related to this area of research, including trajectory generation in the CR3BP and BCR4BP, the general debris environment in cislunar space, the Kordylewski clouds, and prior studies of fragmentation events in the vicinity of Lagrange points. Chapter II also includes a brief examination of spacecraft survivability literature, specifically related to vulnerability and the probability of spacecraft survivability. In Chapter III, the CR3BP and BCR4BP trajectory models are developed, and features of these models are analyzed. Next, a model to determine the number and size of particles generated from a catastrophic spacecraft explosion and the ΔV imparted to each particle is developed. Finally, a statistical model to determine spacecraft survivability is discussed. In Chapter IV, a case study of natural debris comprising the Kordylewski clouds at the Earth-Moon L_4 and L_5 Lagrange points is used to introduce the study of cislunar debris. Chapter V presents the results of the artificial debris case studies. A variety of artificial cislunar debris case studies, each with a different catastrophic mishap scenario, are studied in terms of the threats posed to other spacecraft. Finally, Chapter VI discusses the results of the completed research and presents avenues for future research to be conducted.

II. Literature Review

2.1. Chapter Overview

This chapter reviews prior literature related to the problem of determining the motion of a cloud of debris following a catastrophic spacecraft mishap in cislunar space and the resulting threats to spacecraft. Section 2.2 discusses models for determining spacecraft trajectories in cislunar space, including the patched conic method, perturbation theory, the three-body problem, the four-body problem, and the N-body problem. Section 2.3 covers topics related to debris distribution, including the general meteoroid environment in cislunar space, problems related to space debris, the Kordylewski cloud phenomenon, and prior research on fragmentation events in the vicinity of Lagrange points.

2.2. Spacecraft Trajectory Generation

The complex dynamics of cislunar space makes selecting an accurate trajectory model that includes all relevant gravitational forces and perturbations a crucial consideration. The gravitational influences of the Earth, Moon, and Sun; solar radiation pressure; Earth oblateness effects; atmospheric drag; and the gravity of other bodies in the solar system all influence the motion of a particle moving in cislunar space to some degree. In this section, past research is investigated to identify an appropriate trajectory model for the present research.

2.2.1. Patched Conics

The patched conic method is the simplest method for determining spacecraft trajectories in an environment with multiple gravitational influences. In this solution method, each massive body in space is assigned a “sphere of influence” within which its gravitational

effect dominates. Within this sphere of influence, only the gravitational effect of that body is considered. This reduces the problem to a simple two-body problem, which has an easily calculated analytical solution for the trajectory. As the spacecraft moves between spheres of influences, the central body is changed, so the trajectory generation involves simply patching together multiple two-body problems.

The patched conic method is used very frequently when planning missions to the Moon. The optimal patched conic trajectory involves entering a Hohmann transfer orbit that intersects the lunar sphere of influence, and then performing a capture burn at the closest approach to the Moon to enter lunar orbit. This technique was used to design the trajectory of the SELENE spacecraft, a Japanese Aerospace Exploration Agency (JAXA) lunar polar orbiter. The use of the two burns, one to move from a low Earth parking orbit to a Hohmann transfer orbit and then another to insert into lunar orbit, is described by Kawakatsu in [15] and applied to the design of the SELENE mission trajectory in [16].

Although the patched conic method can provide a good approximation for the trajectories of spacecraft traveling between the Earth and Moon, it suffers from many limitations when compared to higher-fidelity models. In particular, it does not model Lagrange points, the five stationary points in the Earth-Moon system that result from the three-body dynamics. The patched conic method also ignores invariant manifolds that exist in the Earth-Moon three-body problem, which can provide a transfer from the Earth to the Moon for less fuel than a standard Hohmann transfer [17]. Furthermore, low-energy orbits and transfers that take advantage of the Moon's gravity to design unique trajectories become impossible [18]. Higher-fidelity models are needed to more accurately account for the dynamics of cislunar space.

2.2.2. Perturbation Theory

Perturbation theory is another method commonly used to model the motion of spacecraft in cislunar space. This model begins with the equations of the two-body problem, then modifies them to account for "perturbations" from other factors that influence on the motion. This can include the gravitational effects of the Moon and Sun, atmospheric drag, Earth oblateness effects, solar radiation pressure, and the gravitational influence of other bodies in the solar system.

Perturbation theory is especially useful for high-altitude Earth orbits where the gravitational influences of the Moon and Sun can become significant. Namazyfard [6] used a perturbation model to discuss debris prevention through the use of natural instabilities in the Earth-Moon-Sun system to ensure satellites in highly elliptical orbits return to Earth within a reasonable amount of time. Luu and Sabol [19] used a similar perturbation model to examine the effects of lunar and solar gravity on space debris in the disposal orbits above geosynchronous altitude. Friesen et al. [20] also used this method to investigate disposal orbits and study the effects of a satellite breakup in a disposal orbit; finding that debris would extend well into the geosynchronous region. Finally, Rosengren, Scheeres, and McMahon [21] used the perturbation method to investigate stable "frozen" orbits for use in debris storage.

The perturbing functions used to describe the gravitational influence of a body require more higher order terms the closer the spacecraft is to the perturbing body. Therefore, in the Earth-Moon system, when the Moon is modeled as the perturbing body the model of the Moon's gravitational perturbation will tend to become less accurate as the spacecraft

moves farther from the Earth and closer to the Moon [6]. In addition, like the patched conic method, this model does not describe features that result from the three-body dynamics such as Lagrange points and invariant manifolds. These factors mean that other methods will be of more use in this research.

2.2.3. The Three-Body Problem

The Earth-Moon CR3BP models the motion of a spacecraft moving in the gravitational fields of both the Earth and the Moon. As discussed in Section 1.3.1, the CR3BP is a useful model for motion in cislunar space that provides many insights into the dynamical properties of the Earth-Moon system. These properties are explored in more detail in Chapter III.

Trajectories which utilize three-body dynamics to enable unique missions are an ongoing topic of research. A detailed study of optimal cislunar trajectories to the lunar Lagrange points, low lunar orbit, and the lunar surface using CR3BP dynamics has been conducted by Parker and Anderson [18]. Optimal cislunar trajectories were also discussed by Yuying Liang, Ming Xu, and Shijie Xu [24], including analysis of time-of-flight of optimal lunar transfers, applications to a deorbiting strategy for geosynchronous satellites, and periodic cislunar trajectories. Davis et al. [25] studied periodic orbits near the Moon for manned exploration of cislunar space, particularly Near Rectilinear Halo Orbits (NRHOs), which are a family of halo orbits around the L_1 and L_2 points that pass very close to the Moon. Optimization of trajectories in the CR3BP was also used in [22], [26] and [27] to develop low-energy transfers; in [28] and [29] with emphasis on transfers to other near-Earth orbits; in [30] in regards to periodic trajectories that encircle the Earth and

Moon, known as cycler trajectories; in [31] to develop cislunar logistics networks; and in [33] and [34] to analyze navigation for spacecraft rendezvous in halo orbits.

Several recent space missions have incorporated these techniques to operate in cislunar space. The SMART-1 spacecraft, launched in 2003, used a low-energy trajectory to enable a low-thrust mission to the Moon [18]. Two ARTEMIS spacecraft, launched in 2007, used lunar flybys to enable low-energy transfers to the Earth-Moon Lagrange points, becoming the first spacecraft to orbit the Earth-Moon L_1 and L_2 Lagrange points [18]. The Chinese Queqiao relay satellite was launched in May 2018 to a halo orbit around the Earth-Moon L_2 Lagrange point, where it serves as a communications relay for the Chang'e-4 lunar robotic lander. The Chang'e-4 achieved the first ever successful soft landing on the far side of the Moon in January 2019 [23]. Future missions that plan to exploit CR3BP dynamics include NASA's manned Lunar Orbital Platform-Gateway (LOP-G or Gateway), which will utilize the NRHOs discussed in [12], [13], [25], and [35]. Other potential manned missions in cislunar space could utilize long-period excursions that would serve as a "proving ground" to test technologies required for missions to Mars [36].

Some studies have used the Sun-Earth CR3BP to investigate the end-of-life disposal of spacecraft in the Sun-Earth Lagrange points to keep these points clear of debris and avoid encounters with Earth. Colombo et al. [37] suggested a variety of disposal options for the Herschel Space Observatory (formerly at the Sun-Earth L_2 point), the Solar and Heliospheric Observatory (SOHO, currently at the Sun-Earth L_1 point) and the Gaia spacecraft (currently at the Sun-Earth L_2 point). Armellin et al. [38] also investigated disposal methods for the SOHO and Gaia spacecraft. Alessi, Colombo, and Landgraf [39] discussed transfers from the Sun-Earth Lagrange points to near-Earth space in order to

dispose of spacecraft in the Earth's atmosphere. Similar techniques could eventually be used at the Earth-Moon Lagrange points as a growing number of spacecraft operate at those locations.

One limitation of the CR3BP is that it does not incorporate the gravitational influence of the sun. As noted in Section 1.3.2, solar gravity can significantly influence the motion of a spacecraft in cislunar space, especially over long periods, and will be incorporated into the trajectory model for this research. However, results from the CR3BP are still incredibly useful in identifying the dynamical properties of the Earth-Moon system, and trajectories generated using the CR3BP can provide a useful starting point for analysis.

2.2.4. The Four-Body Problem

Namazyfard's [6] study of the unexpected longevity of the EGO satellite provides an example of the importance of including solar gravity in the trajectory generation model. Due largely to lunar and solar perturbations, the perigee of EGO oscillates between about 285 km and over 50,000 km over about 3,000 days, and the spacecraft has yet to return to Earth. According to Namazyfard, the perturbing accelerations caused by the Sun and Moon are on about the same order of magnitude for spacecraft near Earth. Namazyfard also calculated that the rates of change of the longitude of the ascending node and argument of perigee due to the Sun's gravity are about half the rates of change due to the Moon's gravity, indicating that solar gravity plays a significant role in the evolution of the orbit over time. The CR3BP does not account for these dynamics, emphasizing the need for a model that includes the effects of solar gravity.

The BCR4BP extends the CR3BP to incorporate solar gravity, thus more accurately describing motion in cislunar space. The BCR4BP was studied by Huang in 1960 [10],

who developed a model that assumes that the Sun, Earth, and Moon are all coplanar and move in circular orbits. Under these assumptions, the motion of the three massive bodies is not coherent, meaning their motion is not consistent with Newton's laws of gravitation [11]. Because the Earth and Moon are assumed to move in invariant circular orbits, their motion is not a solution to the Sun-Earth-Moon 3-body problem. This lack of coherence can be fixed through the model developed by Andreu [40], but the standard BCR4BP is still quite useful for cislunar research [41].

Several of the most applicable existing studies to cislunar debris research use some variation of the BCR4BP. For example, literature on the Kordylewski dust clouds, which are discussed in detail in Section 2.3.2, generally uses some variation of the BCR4BP. The BCR4BP was also used to study the dynamics of objects disposed or deployed from spacecraft in NRHOs by Davis et al. [12] and Boudad [13]. Both papers used a non-planar BCR4BP model that incorporates the inclination of the Earth-Moon system with respect to the Sun. Wen et al. [42] used the planar BCR4BP along with a model for solar radiation pressure to analyze spacecraft with solar sails moving in formation with debris for debris capture and removal.

In addition, the BCR4BP is frequently used to model low-energy cislunar trajectories, often after using the CR3BP to identify candidate trajectories. Low-energy transfers to the Moon were investigated by in this manner by Ren and Shan [43], who identified candidate trajectories using the CR3BP, then modeled them using the planar BCR4BP. A similar analysis was conducted by Ming Xu, Yan Wei, and Shijie Xu [44], but using a non-planar BCR4BP model. Finally, Koon [11] developed the planar BCR4BP equations of motion

for use in cislunar trajectory generation. The many applications of the BCR4BP to cislunar trajectories suggest that it is a valid model for the present research.

2.2.5. High-Fidelity Models

High-fidelity numerical orbit propagators are often used to validate the results from analytical models. These models can account for perturbations such as N-body gravitational effects from other bodies in the solar system, non-spherical gravitational potentials, solar radiation pressure, and atmospheric drag. For example, The Jet Propulsion Laboratory's (JPL) DE421 Planetary Lunar Ephemerides, which models the positions and velocities of all planets, the Pluto/Charon system, and the Moon, is used by Parker [18] to correct results from the CR3BP by incorporating N-body effects. JPL ephemeris models were also used to incorporate N-body effects by [28], [29], [38], and [39]. Other resources for high-fidelity orbit propagation include THALASSA, used by Namazyfard [6], and the NAIF SPICE planetary ephemerides, used by Davis et al. [12] and Boudad [13] in conjunction with the GRAIL model for lunar gravity. However, such models lead to an increase in required computation time, which would become especially apparent when simulating many particles for long time periods, so these models were not used in the present research.

2.3. Debris Distribution

The second group of contemporary literature surveyed includes topics related to the background meteoroid environment in cislunar space, space debris issues, the behavior of clouds of debris, spacecraft survivability, and the properties of a spacecraft mishap. These referential sources have informed the formulation of various methods used to study a debris event in cislunar space.

2.3.1. General Debris Environment

The ambient meteoroid[2] environment in cislunar space has been a subject of study since the 1960s. These studies can provide a baseline to determine by what factor a cislunar debris event increases the particle flux in cislunar space. Burbank, Cour-Palais, and McAllum [45] developed expressions for the flux of meteoroid particles by mass in cislunar space in a 1965 NASA report. This paper noted that the size of meteoroid particles is always greater than 0.3 μm for metallic particles, because smaller particles are swept out of the solar system by solar radiation pressure. Davidson and Sandorff [46] studied the sources of meteoroids, the structural damage meteoroid impacts could cause to spacecraft, and spacecraft shielding methods in a 1963 NASA report. Singer [47] analytically predicted a dust shell around the Earth with a concentration of dust a few times higher than the concentration in interplanetary space in a 1961 paper. Hyde and Alexander [48] studied ejecta from the lunar surface and found that some intersected the Earth's magnetic field and obtained geocentric orbits. More recently, Altobelli, Grün, and Landgraf [49] studied data collected from the Helios spacecraft to analyze the density, composition, and

[2] Meteoroids are rocky or metallic objects in space that range in size from small, dust-sized grains to rock-sized objects less than about 1 meter in diameter.

interaction with solar radiation pressure of interstellar dust particles near Earth. In this paper, the ratio of solar radiation pressure to the gravitational force, β, was calculated as a function of particle mass. This ratio is extremely small for particles heavier than about 10^{-10} kg, indicating that gravity has a much more significant influence on the motion of larger particles.

The danger of debris from artificial sources first became a concern in the 1970s, particularly following Kessler's 1978 paper on the creation of an artificial debris belt around the Earth [5]. A detailed study of the history of debris mitigation efforts and international legal issues related to space debris is given by Taylor in [50]. Debris in geosynchronous orbits has become an especially large concern due to how crowded these orbits have become, leading to the creation of designated high-altitude disposal orbits. The recommended height above geosynchronous altitude for these disposal orbits has increased as understanding of lunar and solar perturbations has improved [51]. Debris in cislunar space was mentioned as a growing concern in 1988 by Keay [52], who expressed the need to also protect interplanetary space from potential debris sources such as particles from solid rocket propellants and nuclear waste in his 1998 paper. Friedlander [53] studied options for the safe disposal of nuclear reactors from lunar and interplanetary missions. Although artificial debris in cislunar space beyond geosynchronous altitude is currently not significant, these papers reflect the need to consider debris mitigation for all types of space missions.

2.3.2. Kordylewski Clouds

Of the five stationary Lagrange points where the gravitational forces balance in the CR3BP, two, L_4 and L_5, are stable. Objects at the L_4 or L_5 points, located 60º ahead and

behind the central body, respectively, are in stable equilibrium and will tend to return to those points if perturbed. Any object at one of the collinear Lagrange points L_1, L_2, or L_3 is in unstable equilibrium and will tend to fall away from these points if perturbed. Therefore, natural satellites at the L_4 and L_5 points are common. For example, over 7,000 asteroids have been discovered at the Sun-Jupiter L_4 and L_5 points [54].

Polish astronomer Kazimierz Kordylewski first began searching for large objects near the Earth-Moon L_4 and L_5 points with a telescope in 1951. After the initial search was unsuccessful, Kordylewski instead began looking for a cloud of small dust particles too small to be seen individually, but collectively visible with the naked eye on dark and clear nights. He first observed large patches (about four times the size of the Moon) near the L_5 point in 1956, then succeeded in photographing the dust patches in 1961. There have since been numerous attempts, both successful and unsuccessful, to observe these clouds, now known as the "Kordylewski clouds." The Japanese Hiten space probe intended to confirm the existence of the Kordylewski clouds when it passed through the L_4 and L_5 points in 1993, but no obvious increase in dust concentration was detected [54].

Several papers have sought to explain the dynamics of the hypothesized Kordylewski clouds and demonstrate that they can exist. Pohle used the CR3BP to analyze the motion of the clouds in 1962 [55][56], concluding that the dynamics allowed cloud shapes like those observed by Kordylewski. Salnikova and Stepanov in [14], [54], [57], and [58] have extensively studied the Kordylewski clouds using the planar BCR4BP and a model for the force exerted by solar radiation pressure, showing that dust is stable at the L_4 and L_5 points even with gravitational perturbations from the Sun. The optimal times for maximum visibility of the clouds as seen from Earth are discussed in [14], the motion of charged dust

particles in the clouds is studied in [54], a probabilistic model for the distribution of dust is developed in [57], and the possibility of multiple dust clouds is examined in [58].

In 2018, a detailed study by Slíz-Balogh, Barta, and Horváth [8][59] was reported to have confirmed the existence of the Kordylewski clouds. In the first part of the study [8], a three-dimensional restricted four-body problem was used to simulate the motion of particles in the vicinity of the L_5 Lagrange point. The positions and velocities of the Sun, Earth, and Moon were taken from the JPL HORIZONS database. To determine if interplanetary dust would become trapped near the L_5 point, 1,860,000 particles moving slowly relative to L_5 were simulated using four-body dynamics in the vicinity of L_5. Solar radiation pressure was also considered; however, because solar radiation ejects particles with sizes between 0.1 μm and 0.5 μm from the L_5 point while having a negligible effect on larger particles, it was not needed in the simulation. The resulting summed distribution of particle positions matched well with optical analysis conducted using ground-based imaging polarimetry in the second part of the study [59].

The existence of the Kordylewski clouds could suggest hazards to spacecraft operating near the L_4 and L_5 points, particularly if rock-sized particles can circulate in the L_4 and L_5 for long periods as suggested in [8]. This issue could be exacerbated if artificial debris begins to collect in these points. Methods very similar to those used to study the Kordylewski clouds are used in the present research to determine if large fragments of artificial debris from a catastrophic spacecraft mishap could begin to collect near the stable Lagrange points.

2.3.3. Collinear Lagrange Point Debris

Some prior literature exists on catastrophic spacecraft mishaps at collinear Lagrange points. Landgraf and Jehn [60] studied the effects of a spacecraft explosion in the Sun-Earth L_2 point. The explosion creates a cloud of debris in the stable manifold, and about 56% of the fragments in the simulation moved towards earth, with almost all approaching within the Moon's orbit. About 7% of the fragments came within geosynchronous altitude and about 2% reached the low Earth orbit (LEO) environment. Bandyopadhyay, Sharma, and Tewari [7] conducted a similar study on a fragmentation event at the Earth-Moon L_1 point, and found that about 1.6% of the fragments came within geosynchronous altitude. The authors emphasized the need for a more detailed study of fragmentation events at the collinear Earth-Moon Lagrange points.

2.3.4. Spacecraft Survivability

Survivability refers to the ability to remain mission capable in a hostile environment [61]. Although survivability is typically studied in the context of aircraft combat engagements, the same analysis techniques can be applied to spacecraft threatened by both manmade and natural space debris [62][63]. Ball [61] outlined a technique known as the "binomial approach" to determine the probability a system will become inoperable ("killed") when hit by a certain number of penetrators. This model was used by Bettinger and Hess [63] to analyze the survivability of spacecraft modules flying in a close fractionated formation if one of the modules suffers a catastrophic explosion. In this model, the vulnerability of a system to threats is defined in terms of either a probability of kill for the system, P_K, or probability of system survival, P_S, following hits by n penetrators. $P_{K|H}$ is the conditional probability of system kill given that the system is hit by a penetrator. In

[63], a “hit” was defined as a debris fragment trajectory that intersects or is tangential to the spacecraft “danger zone.” This “danger zone” was defined as a sphere around the spacecraft. All fragments that pass within this sphere were considered to have hit the spacecraft.

Another method for determining spacecraft survivability in an environment with debris is the Poisson approach [61]. In this approach, the number of hits is a random variable, with an expected number of hits E. This scenario would occur if a cloud of particles is impacting a spacecraft. The probability of kill depends on the density of particles (ρ) within a spherical danger zone and the chosen $P_{K|H}$. This method is the primary survivability model used for the present research, and the details of this model are described in more detail in Chapter III.

2.3.5. Spacecraft Mishaps

The propagation of debris following a catastrophic spacecraft mishap depends on the properties of the mishap. This research will focus on a catastrophic spacecraft mishap caused by a battery explosion, which has occurred previously with the DMSP and NOAA 16 satellites [4]. This type of debris event expels particles in all directions and imparts some additional ΔV to each particle. Events of this nature were studied by Chobotov [64], who provides methods for calculating the mass and velocity distributions for particles resulting from a spacecraft explosion. Similar techniques are used in Chapter III to determine the initial conditions for the propagation of debris.

2.4. Summary

This chapter has reviewed prior literature related to cislunar trajectory generation and debris in cislunar space. A graphical representation of the literature discussed in this chapter is shown in Figure 2 and Figure 3. Figure 2 shows all literature related to cislunar trajectory generation discussed in Section 2.2, and Figure 3 shows all literature related to cislunar debris distribution discussed in Section 2.3. In these diagrams, the black circles contain topic headings, which correspond to the subheadings in each section, and each topic heading is connected to the sources related to that topic. For the sources that involved trajectory generation, the perturbations included in the trajectory generation model are identified using the colored columns.

Based on the methods used in the literature described in this section, the most applicable trajectory generation model for the present research is the BCR4BP. A thorough review of past research has also indicated that certain perturbations may be neglected. Solar radiation pressure is neglected due to the focus of the present research on particularly large particles that could potentially damage spacecraft. The force due to solar radiation is negligible compared to gravitational forces for larger particles. Earth oblateness effects and atmospheric drag are also neglected, because these perturbation effects significantly decrease at large distances from Earth in cislunar space. In the next chapter, Chapter III, the BCR4BP equations of motion used to calculate debris particle trajectories are developed.

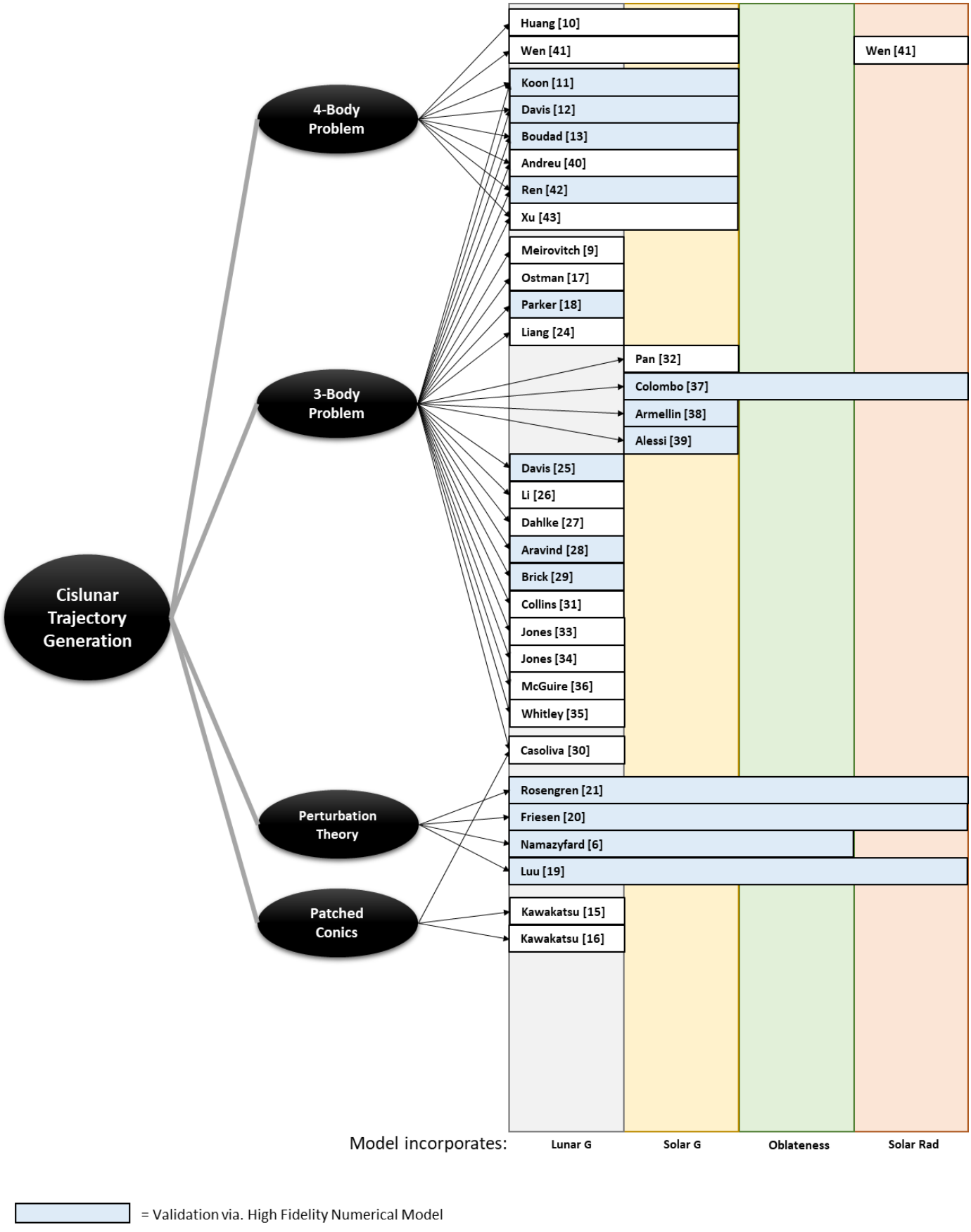

Figure 2. Cislunar Trajectory Generation Literature Diagram

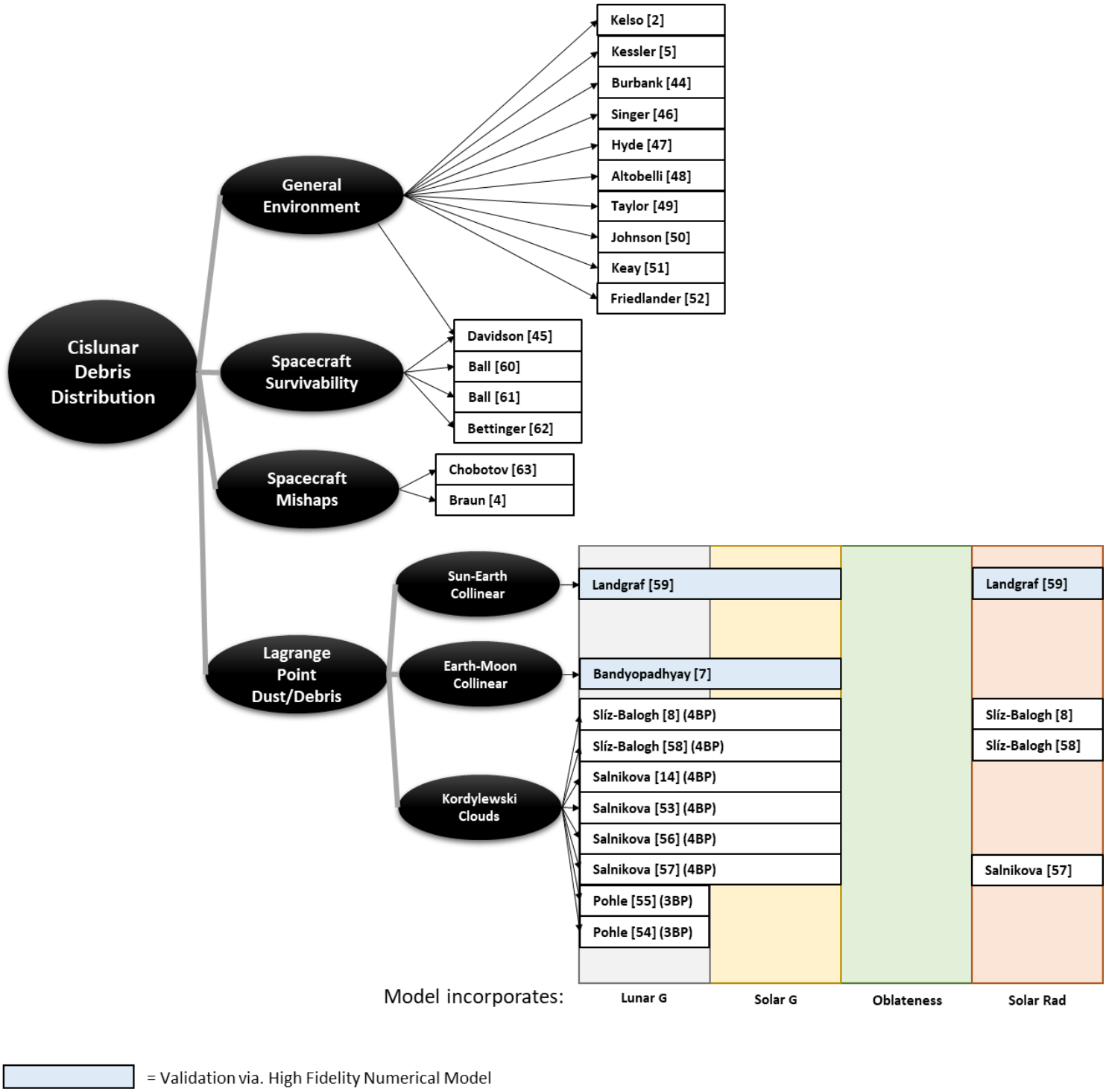

Figure 3. Cislunar Debris Distribution Literature Diagram

III. Methodology

3.1. Chapter Overview

This chapter develops the models used for trajectory generation, the spacecraft catastrophic mishap, and spacecraft survivability. The equations of motion for the CR3BP are developed and used to analyze the dynamical properties of the Earth-Moon system in Section 3.2. Although the CR3BP is not the main trajectory generation model for this research, the study of this problem provides significant insight into the dynamical behavior of objects in the Earth-Moon system. The BCR4BP, the primary trajectory model for the present research, is discussed in Section 3.3. Next, the model for the catastrophic mishap is given in Section 3.4. Finally, the spacecraft survivability model is developed in Section 3.5.

3.2. The Circular Restricted Three-Body Problem

A diagram of the CR3BP for the Earth-Moon system, with a rotating coordinate frame centered at the Earth-Moon barycenter, is shown in Figure 4. In this section, six first-order differential equations of motion are developed using a Hamiltonian formulation of the CR3BP, which are then reduced to three-second order equations of motion and non-dimensionalized. The Hamiltonian formulation is used because constants of the motion become apparent in this formulation, and the constant of the CR3BP motion is examined in Section 3.2.3. The Hamiltonian formulation can also be used to add in small perturbation forces, though these are not necessary for this research.

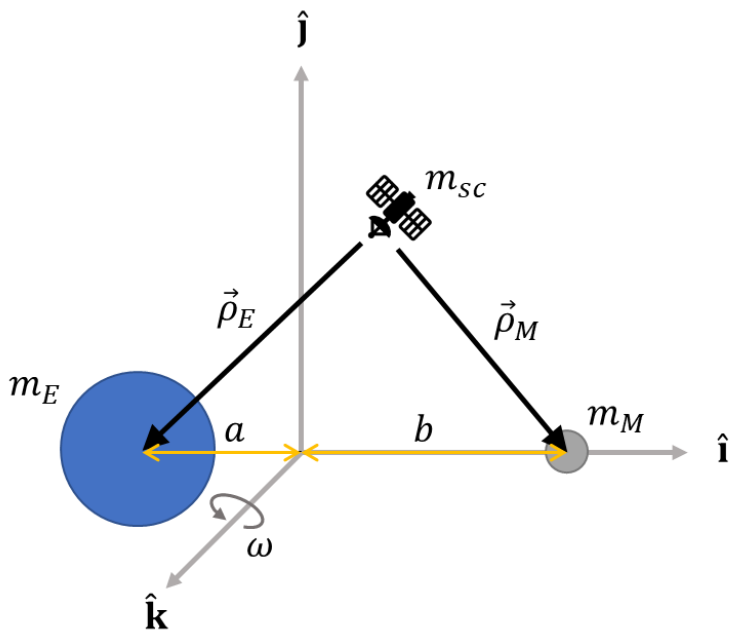

Figure 4. Earth-Moon-Spacecraft CR3BP in a Barycentric Rotating Reference Frame

From Figure 4, the Earth and Moon radius vectors are defined in the rotating frame as:

$$\vec{r}_E = -a\hat{\mathbf{i}} \tag{1}$$

$$\vec{r}_M = b\hat{\mathbf{i}} \tag{2}$$

Where $\vec{r}_E$ is the radius vector from the Earth-Moon barycenter to the Earth, and $\vec{r}_M$ is the radius vector from the barycenter to the Moon. The radius vector from the barycenter to the spacecraft is defined in the rotating frame as:

$$\vec{r}_{sc} = x\hat{\mathbf{i}} + y\hat{\mathbf{j}} + z\hat{\mathbf{k}} \tag{3}$$

The velocity of the spacecraft in the inertial frame, $\vec{v}_{sc}$, is calculated using the transport theorem, where $\dot{\vec{r}}_{sc}$ is the derivative of the spacecraft position in the rotating frame, and $\vec{\omega} = \omega\hat{k}$ is the angular velocity of the Earth-Moon rotating frame:

$$\vec{v}_{sc} = \dot{\vec{r}}_{sc} + \vec{\omega} \times \vec{r}_{sc} \tag{4}$$

The inertial spacecraft velocity is found to be:

$$\vec{v}_{sc} = (\dot{x} - \omega y)\hat{\mathbf{i}} + (\dot{y} + \omega x)\hat{\mathbf{j}} + \dot{z}\hat{\mathbf{k}} \tag{5}$$

In the Hamiltonian formulation, expressions for the kinetic and potential energy of the spacecraft are needed. The kinetic energy due to the velocity of the spacecraft is:

$$T = \frac{1}{2} m_{sc} |\vec{v}_{sc}|^2 \tag{6}$$

Substituting in $\vec{v}_{sc}$ and collecting velocity terms of like powers leads to:

$$\begin{aligned} T = {} & \frac{1}{2} m_{sc}(\dot{x}^2 + \dot{y}^2 + \dot{z}^2) + m_{sc}(\omega x\dot{y} - \omega y\dot{x}) \\ & + \frac{1}{2} m_{sc}(\omega^2 x^2 + \omega^2 y^2) \end{aligned} \tag{7}$$

The potential energy of the spacecraft results from the gravitational potential of the Earth and Moon and depends on the distance from each body. The expression for the gravitational potential energy in the CR3BP is:

$$V = -G m_{sc}\left(\frac{m_E}{\rho_E} + \frac{m_M}{\rho_M}\right) \tag{8}$$

where G is the gravitational constant, ρ_E is the distance from the spacecraft to the Earth, and ρ_M is the distance from the spacecraft to the Moon. Note that ρ_E and ρ_M may be calculated using:

$$\rho_E = |\vec{\rho}_E| = \sqrt{(x + a)^2 + y^2 + z^2} \tag{9}$$

$$\rho_M = |\vec{\rho}_M| = \sqrt{(x-b)^2 + y^2 + z^2} \tag{10}$$

In the Hamiltonian formulation of the CR3BP, the state of the particle is expressed in phase space, i.e., in terms of position and momentum variables. Therefore, the velocities in the kinetic energy expression must be transformed into expressions involving the position variables and newly defined momenta variables. These momenta are given by:

$$p_x = \frac{\partial T}{\partial \dot{x}} = m_{sc}(\dot{x} - \omega y) \tag{11}$$

$$p_y = \frac{\partial T}{\partial \dot{y}} = m_{sc}(\dot{y} + \omega x) \tag{12}$$

$$p_z = \frac{\partial T}{\partial \dot{z}} = m_{sc}\dot{z} \tag{13}$$

Solving for $\dot{x}$, $\dot{y}$, and $\dot{z}$ in terms of the momenta results in:

$$\dot{x} = \frac{p_x}{m_{sc}} + \omega y \tag{14}$$

$$\dot{y} = \frac{p_y}{m_{sc}} - \omega x \tag{15}$$

$$\dot{z} = \frac{p_z}{m_{sc}} \tag{16}$$

Substituting these into the expression for kinetic energy, Equation (7), and simplifying gives the kinetic energy in terms of momenta:

$$T = \frac{1}{2m_{sc}}\left(p_x^2 + p_y^2 + P_z^2\right) \tag{17}$$

The next step is to formulate the Hamiltonian. The Hamiltonian function represents an energy-like quantity, and because the system is conservative, it can be considered a constant of the motion. The Hamiltonian, which is used to derive Jacobi's Constant in Section 3.2.3, is:

$$\begin{aligned} H &= \sum_{i=1}^{n} p_i \dot{q}_i - T + V \\ &= \frac{p_x^2}{m_{sc}} + \omega p_x y + \frac{p_y^2}{m_{sc}} - \omega p_y x + \frac{p_z^2}{m_{sc}} - T + V \end{aligned} \tag{18}$$

Substituting in the expression for kinetic energy, Equation (17), and simplifying gives:

$$H = \frac{1}{2m_{sc}}\left(p_x^2 + p_y^2 + p_z^2\right) - \omega\left(p_y x - p_x y\right) + V \tag{19}$$

Applying Hamilton's Equations, $\dot{p}_i = -\frac{\partial H}{\partial q_i}$ and $\dot{q}_i = \frac{\partial H}{\partial p_i}$, gives the equations of motion:

$$\dot{p}_x = \omega p_y + G m_{sc}\left(\frac{m_M(b-x)}{\rho_M^3} - \frac{m_E(a+x)}{\rho_E^3}\right) \tag{20}$$

$$\dot{p}_y = -\omega p_x - G m_{sc}\left(\frac{m_E y}{\rho_E^3} + \frac{m_M y}{\rho_M^3}\right) \tag{21}$$

$$\dot{p}_z = -G m_{sc}\left(\frac{m_E z}{\rho_E^3} + \frac{m_M z}{\rho_M^3}\right) \tag{22}$$

$$\dot{x} = \frac{1}{m_{sc}} p_x + \omega y \tag{23}$$

$$\dot{y} = \frac{1}{m_{sc}} p_y - \omega x \tag{24}$$

$$\dot{z} = \frac{1}{m_{sc}} p_z \tag{25}$$

Equations (20)-(25) represent the six first-order differential equations that describe the motion of the spacecraft. These equations can be reduced to three second-order differential

equations by substituting the expressions for momenta, given by Equations (11)-(13), and their time derivatives into Equations (20)-(22):

$$\ddot{x} = \omega^2 x + 2\omega\dot{y} + G\left(\frac{m_M(b-x)}{\rho_M^3} - \frac{m_E(a+x)}{\rho_E^3}\right) \tag{26}$$

$$\ddot{y} = \omega^2 y - 2\omega\dot{x} - G\left(\frac{m_E y}{\rho_E^3} + \frac{m_M y}{\rho_M^3}\right) \tag{27}$$

$$\ddot{z} = -G\left(\frac{m_E z}{\rho_E^3} + \frac{m_M z}{\rho_M^3}\right) \tag{28}$$

The values of all parameters used in the preceding development are given in Table 1.

Table 1. Values of Parameters in the CR3BP Equations of Motion

Parameter	Value
m_E	5.972×10^{24} kg
m_M	7.342×10^{22} kg
a	4,671 km
b	379,731 km
ω	2.662×10^{-6} rad/s
G	6.674×10^{-11} m^3 / kg s^2

3.2.1. Conversion to Non-dimensional Equations

To reduce numerical error during integration, it is best to ensure that the numerical values of all terms in the equations of motion are about the same order of magnitude. This may be accomplished through non-dimensionalization of the equations of motion. Defining a parameter μ to represent the mass of the Moon in terms of the mass of the Earth-Moon system, the masses of the Earth and Moon are replaced with the non-dimensional values:

$$m_M = \frac{m_M}{m_E + m_M} = 0.01215 = \mu \tag{29}$$

$$m_E = \frac{m_E}{m_E + m_M} = 0.98787 = 1 - \mu \tag{30}$$

The distance between the Earth and Moon may also be non-dimensionalized such that $a + b = 1$. The values of a and b from Figure 4 are then determined by solving the following equation, knowing that the center of mass is located at $x = 0$:

$$\begin{aligned} \frac{r_E m_E + r_M m_M}{m_E + m_M} &= \frac{-a * (1-\mu) + b * \mu}{1} = -a(1-\mu) + (1-a)\mu \\ &= -a + a\mu + \mu - a\mu = 0 \end{aligned} \tag{31}$$

which gives $a = \mu$. The non-dimensional distance between the Earth and Moon is:

$$b = 1 - a = 1 - \mu \tag{32}$$

Selecting non-dimensional time units such that the time required for the Moon to complete one orbit around the Earth is 2π gives $\omega = 1$. Solving for G using the mean motion equation shows that $G = 1$:

$$\omega^2 = 1 = \frac{G(m_M + m_E)}{(a+b)^3} = \frac{G(\mu + 1 - \mu)}{(\mu + 1 - \mu)^3} = G \tag{33}$$

The new non-dimensionalized second-order equations of motion are:

$$\ddot{x} = x + 2\dot{y} - \frac{(1-\mu)(x+\mu)}{\rho_E^3} - \frac{\mu(x - 1 + \mu)}{\rho_M^3} \tag{34}$$

$$\ddot{y} = y - 2\dot{x} - \frac{(1-\mu)y}{\rho_E^3} - \frac{\mu y}{\rho_M^3} \tag{35}$$

$$\ddot{z} = -\frac{(1-\mu)z}{\rho_E^3} - \frac{\mu z}{\rho_M^3} \tag{36}$$

These equations of motion are now in terms of the characteristic quantities given in Table 2. The non-dimensionalized time and distance units in these equations are referred to as Time Units (TU) and Distance Units (DU), respectively.

Table 2. Characteristic Quantities for the Earth-Moon System [17]

Parameter	Value
Characteristic Length (l^*)	384400 km
Characteristic Mass (m^*)	6.0458×10^{24} kg
Characteristic Time (t^*)	4.3425 days

3.2.2. Equilibrium Points

Equilibrium points in the CR3BP are determined by setting all velocity and acceleration terms in the equations of motion equal to zero. Solving for position gives points where a spacecraft can remain fixed in a rotating reference frame. The five points that satisfy these conditions, known as Lagrange points, have two-dimensional coordinates given in Table 3, and these points are plotted in Figure 5.

Table 3. Coordinates of Lagrange Points in the Earth-Moon System

Lagrange Point	x Position (DU)	y Position (DU)
L_1	0.8369	0
L_2	1.1557	0
L_3	-1.005	0
L_4	0.4878	0.8660
L_5	0.4878	-0.8660

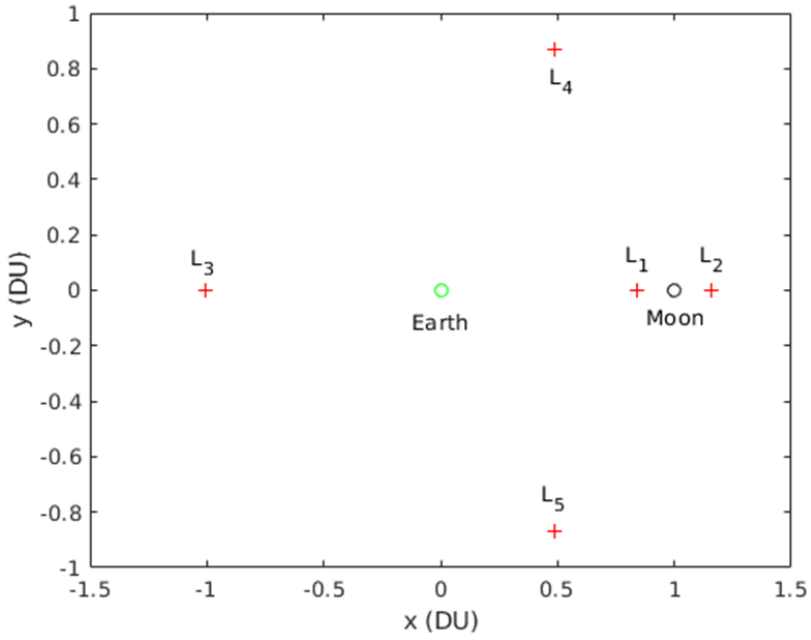

Figure 5. Equilibrium Points in the Earth-Moon CR3BP

3.2.3. Jacobi's Constant

Although total energy is not constant in the Earth-Moon rotating frame in the CR3BP, the Hamiltonian represents an "energy-like" integral of the motion. Representing the Hamiltonian, Equation (19), in terms of position and velocity variables, with the total velocity in the rotating frame given by $v_R = \sqrt{\dot{x}^2 + \dot{y}^2 + \dot{z}^2}$:

$$H = \frac{1}{2} m_{sc} v_R^2 - \frac{1}{2} m_{sc} \omega^2 (x^2 + y^2) + V \tag{37}$$

The position terms can be incorporated into a modified potential energy, U, defined as:

$$U = G\left(\frac{m_E}{\rho_E} + \frac{m_M}{\rho_M}\right) + \frac{1}{2}\omega^2 (x^2 + y^2) \tag{38}$$

The Hamiltonian becomes:

$$H = \frac{1}{2} m_{sc} v_R^2 - m_{sc} U \tag{39}$$

Dividing by spacecraft mass m_{sc} and multiplying both sides by -2 gives the constant of the motion referred to as Jacobi's Constant, C:

$$C = 2U - v_R^2 \tag{40}$$

This value is constant throughout a trajectory in the CR3BP. Jacobi's Constant can be tracked during numerical integration to ensure that it remains constant to within a desired numerical tolerance.

3.2.4. Zero-Velocity Curves

The Jacobi Constant provides insight into the accessible and forbidden regions in the CR3RP. Regions that are accessible with a given value of the Jacobi Constant are bounded by curves where $v_R = 0$, called Zero-Velocity Curves (ZVC). The spacecraft cannot cross these curves unless a ΔV is performed, so regions beyond the ZVC are called "forbidden regions." The ZVC and for varying values of the Jacobi Constant are shown in Figure 6. The forbidden regions are shaded in gray. Starting at approximately $C = 3.18$, a spacecraft can transfer between the Earth and the Moon. As the Jacobi Constant decreases, more regions of cislunar space become accessible.

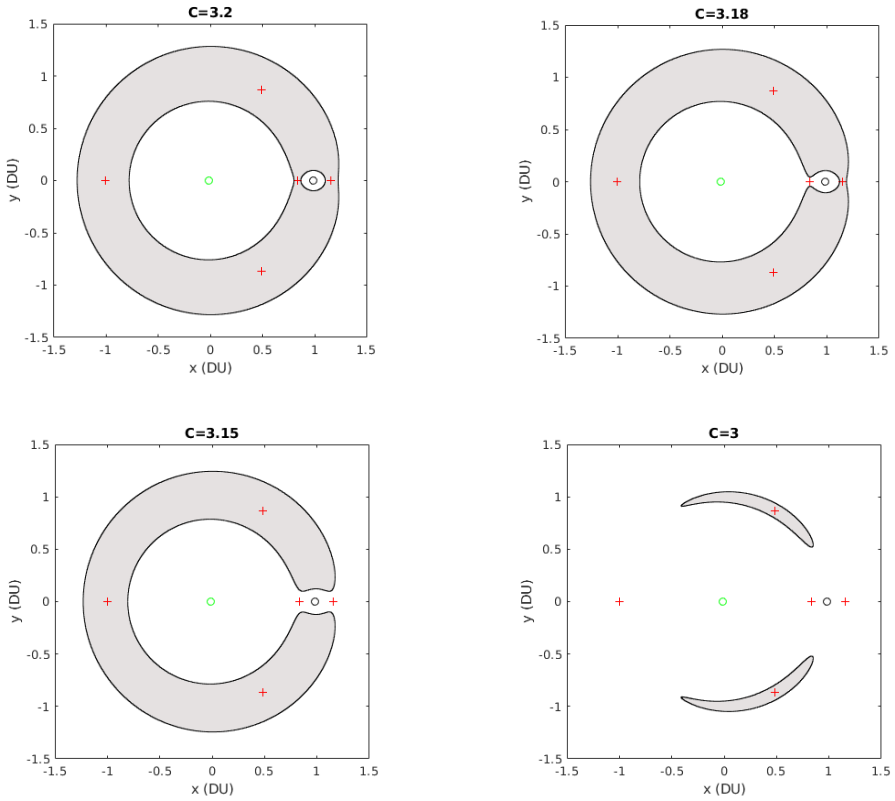

Figure 6. ZVC for Varying Jacobi Constants, Forbidden Regions Shaded Gray

3.3. The Bi-circular Restricted Four-Body Problem

The BCR4BP is the main trajectory generation model used for the present research, and a diagram of this problem is shown in Figure 7. The orbits of the Sun, Earth, and Moon are all assumed to lie in the same plane. The equations of motion are again derived in the Earth-Moon barycentric rotating reference frame shown in Figure 4.

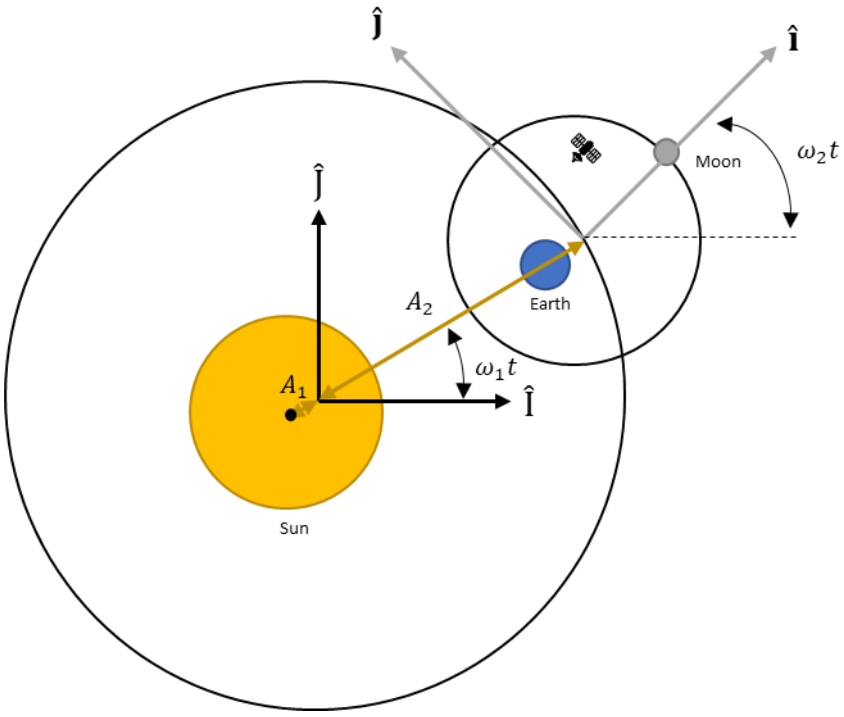

Figure 7. Reference Frames in the BCR4BP

The procedure to derive the BCR4BP equations of motion using the Hamiltonian is very similar to that used to derive the CR3BP equations of motion. The radius vector from the Sun-Earth-Moon barycentric inertial reference frame, shown in Figure 7, to the spacecraft in terms of the basis vectors for Earth-Moon barycentric rotating frame is:

$$\vec{r}_{sc} = [y + A_2 \cos(\omega_1 t - \omega_2 t)]\hat{\mathbf{i}} + [x + A_2 \sin(\omega_1 t - \omega_2 t)]\hat{\mathbf{j}} + z\hat{\mathbf{k}} \tag{41}$$

Applying the transport theorem (Equation 4), the inertial velocity in terms of the basis vectors of the Earth-Moon barycentric rotating frame is:

$$\begin{aligned} \vec{v}_{sc} = {} & (\dot{x} - \omega_2 y - A_2 \omega_1 \sin(\omega_1 t - \omega_2 t))\hat{\boldsymbol{\imath}} \\ & + (\dot{y} + \omega_2 x + A_2 \omega_1 \cos(\omega_1 t - \omega_2 t))\hat{\boldsymbol{\jmath}} + \dot{z}\hat{\boldsymbol{k}} \end{aligned} \tag{42}$$

The kinetic energy is:

$$T = \frac{1}{2} m_{sc} |\vec{v}_{sc}|^2$$

$$= \frac{1}{2} m_{sc} ((\dot{x} - \omega_2 y - A_2 \omega_1 \sin(\omega_1 t - \omega_2 t))^2 \tag{43}$$

$$+ (\dot{y} + \omega_2 x + A_2 \omega_1 \cos(\omega_1 t - \omega_2 t))^2 + \dot{z}^2$$

Calculating the momenta:

$$p_x = \frac{\partial T}{\partial \dot{x}} = m_{sc}(\dot{x} - \omega_2 y - A_2 \omega_1 \sin(\omega_1 t - \omega_2 t)) \tag{44}$$

$$p_y = \frac{\partial T}{\partial \dot{x}} = m_{sc}(\dot{y} + \omega_2 x + A_2 \omega_1 \cos(\omega_1 t - \omega_2 t)) \tag{45}$$

$$p_z = \frac{\partial T}{\partial \dot{z}} = m_{sc} \dot{z} \tag{46}$$

Solving each equation for the velocities in terms of the momenta, then substituting the velocities back into the kinetic energy equation gives kinetic energy in terms of momenta:

$$T = \frac{1}{2m_{sc}} \left(p_x^2 + p_y^2 + p_z^2\right) \tag{47}$$

Next, the gravitational potential energy due to the gravitational fields of the Sun, Earth, and Moon is given by:

$$V = -G m_{sc} \left(\frac{m_S}{\rho_S} + \frac{m_E}{\rho_E} + \frac{m_M}{\rho_M}\right) \tag{48}$$

where the radius vectors to each body are:

$$\rho_i = \sqrt{(x - x_i)^2 + (y - y_i)^2 + (z - z_i)^2}$$

$$i = S, E, M \tag{49}$$

The Hamiltonian is:

$$H = \sum_{i=1}^{n} p_i \dot{q}_i - T + V$$

$$= \frac{1}{2m_{sc}}\left(p_x^2 + p_y^2 + p_z^2\right) - \omega_2\left(p_y x - p_x y\right) + V \tag{50}$$

$$- A_2 \omega_1 p_y \cos(\omega_1 t - \omega_2 t)$$

$$+ A_2 \omega_1 p_x \sin(\omega_1 t - \omega_2 t)$$

Note that this expression is identical to the Hamiltonian for the CR3BP, except for the additional two time-dependent terms. Unlike the CR3BP, the Earth-Moon frame Hamiltonian in the BCR4BP is not a constant of the motion. Applying Hamilton's Equations, $\dot{p}_i = -\frac{\partial H}{\partial q_i}$ and $\dot{q}_i = \frac{\partial H}{\partial p_i}$, gives the equations of motion:

$$\dot{p}_x = \omega_2 p_y - G m_{sc}\left(\frac{m_S(x - x_s)}{\rho_S^3} + \frac{m_E(x - x_E)}{\rho_E^3} + \frac{m_M(x - x_M)}{\rho_M^3}\right) \tag{51}$$

$$\dot{p}_y = -\omega_2 p_x - G m_{sc}\left(\frac{m_S(y - y_s)}{\rho_S^3} + \frac{m_E(y - y_E)}{\rho_E^3} + \frac{m_M(z - z_M)}{\rho_M^3}\right) \tag{52}$$

$$\dot{p}_z = -G m_{sc}\left(\frac{m_S(z - z_s)}{\rho_S^3} + \frac{m_E(z - z_E)}{\rho_E^3} + \frac{m_M(z - z_M)}{\rho_M^3}\right) \tag{53}$$

$$\dot{x} = \frac{p_x}{m_{sc}} + \omega_2 y + A_2 \omega_1 \sin(\omega_1 t - \omega_2 t) \tag{54}$$

$$\dot{y} = \frac{p_y}{m_{sc}} - \omega_2 x - A_2 \omega_1 \cos(\omega_1 t - \omega_2 t) \tag{55}$$

$$\dot{z} = \frac{p_z}{m_{sc}} \tag{56}$$

These six first-order equations may be converted to three second-order equations by substituting the expressions for p_x, p_y, p_z, and their derivatives into the $\dot{p}_x$, $\dot{p}_y$, and $\dot{p}_z$ equations of motion. Substitution yields the following:

$$\ddot{x} = 2\omega_2\dot{y} + \omega_2^2 x + A_2\omega_1^2\cos(\omega_1 t - \omega_2 t) - G\left(\frac{m_S(x - x_S)}{\rho_S^3} + \frac{m_E(x - x_E)}{\rho_E^3} + \frac{m_M(x - x_M)}{\rho_M^3}\right) \tag{57}$$

$$\ddot{y} = -2\omega_2\dot{x} + \omega_2^2 y + A_2\omega_1^2\sin(\omega_1 t - \omega_2 t) - G\left(\frac{m_S(y - y_S)}{\rho_S^3} + \frac{m_E(y - y_E)}{\rho_E^3} + \frac{m_M(y - y_M)}{\rho_M^3}\right) \tag{58}$$

$$\ddot{z} = -G\left(\frac{m_S(z - z_S)}{\rho_S^3} + \frac{m_E(z - z_E)}{\rho_E^3} + \frac{m_M(z - z_M)}{\rho_M^3}\right) \tag{59}$$

These equations may also be non-dimensionalized in the same manner as the CR3BP equations of motion. Non-dimensionalization of these equations yields:

$$\ddot{x} = x + 2\dot{y} + A_2\,\omega_1^2\cos\big(t(\omega_1 - 1)\big) - \frac{m_S(x - x_S)}{\rho_S^3} - \frac{(1-\mu)(x+\mu)}{\rho_E^3} - \frac{\mu(x - 1 + \mu)}{\rho_M^3} \tag{60}$$

$$\ddot{y} = y - 2\dot{x} + A_2\omega_1^2\sin\big(t(\omega_1 - 1)\big) - \frac{m_S(y - y_S)}{\rho_S^3} - \frac{(1-\mu)y}{\rho_E^3} - \frac{\mu y}{\rho_M^3} \tag{61}$$

$$\ddot{z} = -\frac{m_S z}{\rho_S^3} - \frac{(1-\mu)z}{\rho_E^3} - \frac{\mu z}{\rho_M^3} \tag{62}$$

All values in these equations are again in terms of the characteristic quantities in Table 2. The angular velocity of the Earth-Moon system about the system barycenter, ω_1, is:

$$\omega_1 = \sqrt{\frac{m_S + 1}{(A_1 + A_2)^3}} \tag{63}$$

The coordinates of the sun are:

$$x_S = -(A_1 + A_2)\cos\big(t(\omega_1 - 1)\big)$$
$$y_s = -(A_1 + A_2)\sin\big(t(\omega_1 - 1)\big) \tag{64}$$

The numerical values of all constants in the non-dimensionalized equations of motion are given in Table 4.

Table 4. Parameters in the BCR4BP Equations of Motion

Parameter	Value
A_1	0.0012
A_2	389.145
m_S	328910
μ	0.01215
ω_1	0.07471

The debris particle trajectories are determined by numerically integrating the BCR4BP equations of motion. In this research, MATLAB's ODE45 numerical integrator was used with absolute and relative tolerances of 2.5×10^{-10} DU (9.61 cm). These tolerances are well below the sizes of the regions used for survivability analysis (discussed in Section 3.5).

3.3.1. Analysis of Perturbations

The equations of motion may be used to analyze the relative magnitudes of the perturbing accelerations in the BCR4BP model. Representing the accelerations due to the gravity of the Earth, Moon, and Sun as $\vec{a}_E$, $\vec{a}_M$, and $\vec{a}_S$ respectively, the accelerations in the rotating Earth-Moon reference frame due to each body are:

$$\vec{a}_E = \frac{(1-\mu)(x+\mu)}{\rho_E^3}\hat{\mathbf{i}} - \frac{(1-\mu)y}{\rho_E^3}\hat{\mathbf{j}} - \frac{(1-\mu)z}{\rho_E^3}\hat{\mathbf{k}}$$

$$\vec{a}_M = -\frac{\mu(x-1+\mu)}{\rho_M^3}\hat{\mathbf{i}} - \frac{\mu y}{\rho_M^3}\hat{\mathbf{j}} - \frac{\mu z}{\rho_M^3}\hat{\mathbf{k}} \tag{65}$$

$$\vec{a}_S = -\frac{m_S(x-x_S)}{\rho_S^3}\hat{\mathbf{i}} - \frac{m_S(y-y_S)}{\rho_S^3}\hat{\mathbf{j}} - \frac{m_S z}{\rho_S^3}\hat{\mathbf{k}}$$

The rotating Earth-Moon reference frame is non-inertial, so there are additional non-inertial accelerations. These are the non-inertial accelerations due to the rotation of the Earth-Moon frame, represented as $\vec{a}_{EM}$, and due to the revolution of the Earth-Moon barycenter about the Sun-Earth-Moon barycenter, represented as $\vec{a}_{SEM}$:

$$\vec{a}_{EM} = (x+2\dot{y})\hat{\mathbf{i}} + (y-2\dot{x})\hat{\mathbf{j}}$$

$$\vec{a}_{SEM} = A_2\,\omega_1^2\cos\big(t(\omega_1-1)\big)\,\hat{\mathbf{i}} + A_2\omega_1^2\sin\big(t(\omega_1-1)\big)\,\hat{\mathbf{j}} \tag{66}$$

The accelerations $\vec{a}_E$, $\vec{a}_M$, $\vec{a}_{EM}$, and $\vec{a}_{SEM}$ are constant in magnitude over time at any given location, while the magnitude of $\vec{a}_S$ varies over time due to the changing location of the Sun relative to the Earth-Moon rotating reference frame.

Two case studies in this research analyze motion at the L_4 and L_5 Lagrange points. The magnitudes of the accelerations at L_4 and L_5 in the Earth-Moon frame over one complete revolution of the Earth-Moon-Sun system about its barycenter are shown in Figure 8. The only time-varying acceleration is the acceleration due to solar gravity a_s, which varies

according to a period of 2π TU, the same as the period of rotation of the Earth-Moon rotating reference frame. The solar accelerations at L_4 and L_5 differ only in phase, indicating that the behavior of particles at both Lagrange points should be very similar. The particle motion should also exhibit periodic behavior that results from the periodic solar acceleration. The x, y, and z components of the solar acceleration at L_4 and L_5 are shown in Figure 9. The acceleration is periodic in both the x and y directions. Since the inclination of the Earth-Moon system with respect to the Sun was not incorporated in the equations of motion, the acceleration in the z direction is zero. Incorporating the real 5º inclination of the Earth-Moon frame with respect to the Sun would lead to a small periodic component of acceleration in the z direction and small changes to the x and y accelerations when compared to Figure 9.

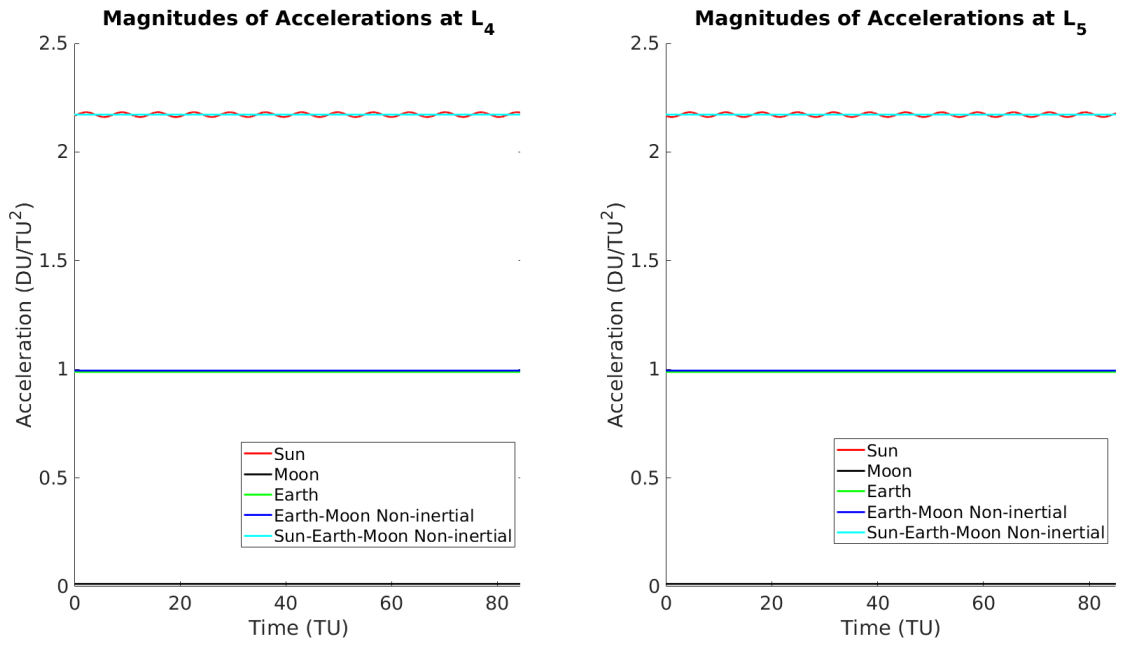

Figure 8. Magnitudes of Accelerations at L_4 and L_5 in the Earth-Moon Reference Frame

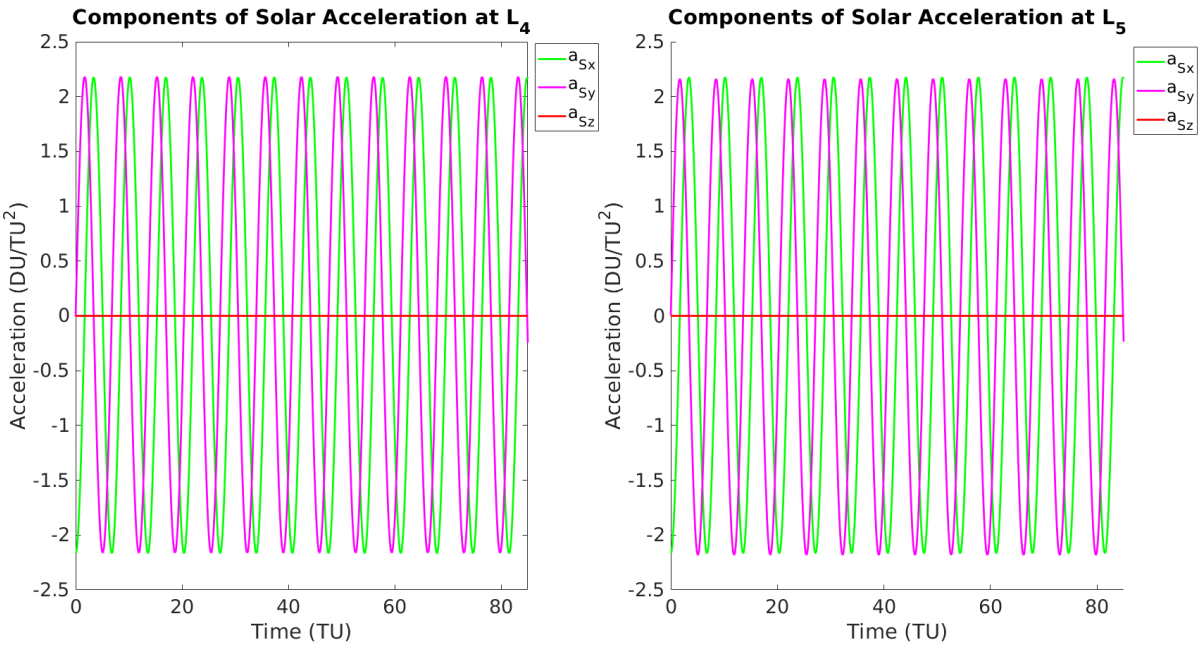

Figure 9. Components of Solar Acceleration at L_4 and L_5 in the Earth-Moon Reference Frame

3.4. Catastrophic Mishap Model

The NOAA 16 satellite battery explosion was used as the model for the catastrophic spacecraft mishap [4]. The two parameters of interest in the simulation are the mass distribution of particles released in the explosion and the change in velocity (ΔV) given to each particle by the explosion. These parameters are determined in the simulation according to the statistical models discussed in this section.

The particle masses were determined in the simulation by fitting a probability distribution to the observed mass distribution in the NOAA 16 explosion, then selecting random numbers from this distribution to assign each particle mass. Each tracked debris particle contains a measure of the size of the particle, the Radar Cross Section (RCS). The

approximate masses of the particles were calculated based on the following formula from [65] for the mass of a debris particle given the RCS:

$$M = 62 \times 10^3 (RCS)^{1.13} \tag{67}$$

The masses of 135 tracked debris particles were calculated and plotted in a histogram, and then a lognormal distribution was fit to the data. The parameters of the resulting lognormal distribution are $\mu = -1.7286$ and $\sigma = 1.4511$. The mass histogram, with the lognormal probability distribution overlaid, is shown in Figure 10.

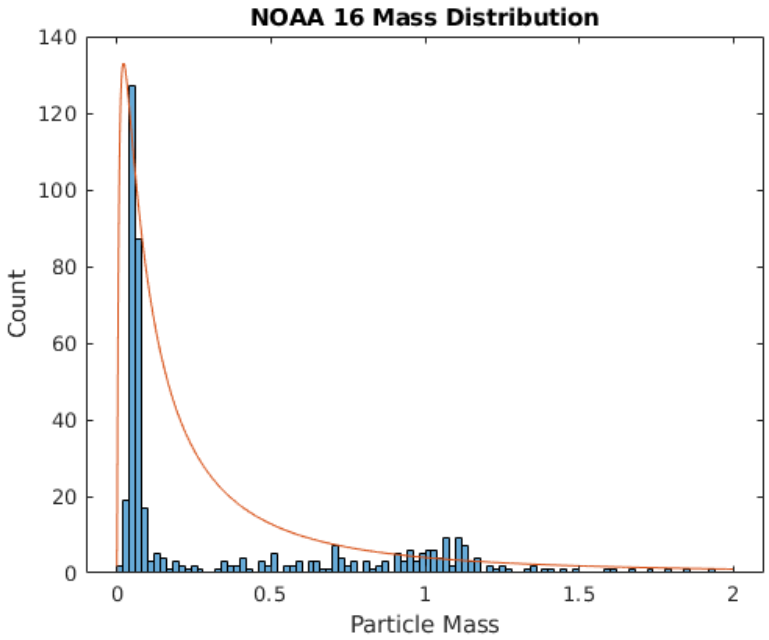

Figure 10. Particle Mass Histogram (blue), with Fitted Probability Distribution (orange)

In the simulation, particle masses were selected randomly from the lognormal distribution until the combined mass of the particles matched the mass of the original NOAA 16 satellite, 1457 kg. Therefore, the total number of particles simulated is random and changes with each simulation.

After determining the masses of each debris particle, the ΔV given to each particle was calculated by determining the amount of kinetic energy released in the NOAA 16 explosion. The Two-Line Element sets (TLEs) for 135 debris particles tracked within a month of the explosion were used to propagate the particles back to the explosion time, approximately 07:20 UTC on 25 November 2015 [66]. The velocity vectors in the Earth-Centered Inertial (ECI) reference frame were calculated at the time of the explosion, and then subtracted from the velocity vector of the NOAA 16 satellite to determine the relative velocities of the debris particles. This relative velocity was then used to calculate relative kinetic energies of all particles. The average kinetic energy per particle was 6678 J. For the simulation, all particles are assumed to be given the same amount of kinetic energy by the explosion. Therefore, given a particle's mass, the scalar change in velocity of that particle is given by:

$$v = \sqrt{\frac{2}{m} KE} = \sqrt{\frac{2}{m} (6678 \text{ J})} \tag{68}$$

Example histograms of particle mass and ΔV determined using this method for one run of the simulation are shown in Figure 11. Note that each run of the simulation will involve slightly different particle masses and velocities due to the random selection of particle masses. The simulated mass and velocity distributions match well with the data from the NOAA 16 satellite. The average particle ΔV for the simulation and the actual NOAA 16 explosion are both approximately 100 m/s.

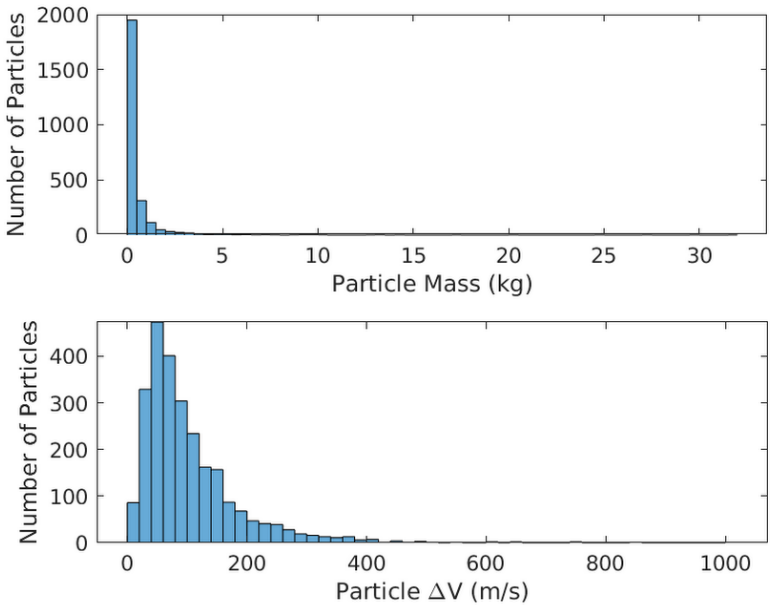

Figure 11. Example Histogram of Simulated Particle Masses and Changes in Velocity

A direction for the velocity vector was assigned by picking a random direction on a sphere to represent an omnidirectional explosion. The velocity vectors obtained using this method from one run of the simulation are shown in Figure 12. Again, note that each simulation run will result in a slightly different explosion velocity distribution due to the random selection of particle masses and the random assignment of velocity directions.

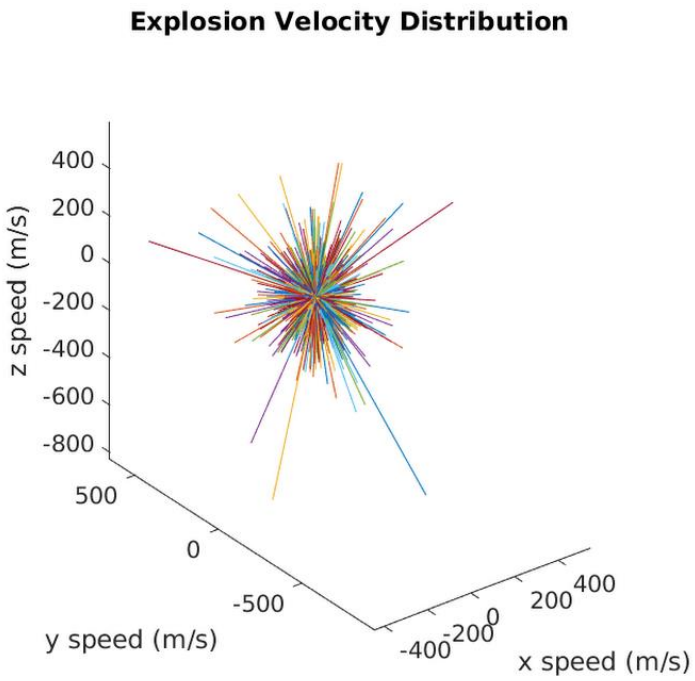

Figure 12. Example Simulated Explosion Velocity Vectors

3.5. Survivability Model

The trajectories of debris particles generated using the BCR4BP form the input to the spacecraft survivability model. The primary spacecraft survivability model used for the present research is a variation of the Poisson approach discussed in Section 2.3.4. The Poisson method developed by Ball [61] is extended to the study of the survivability of a cislunar spacecraft moving in a field of debris. If the cloud of debris fragments is treated as a spray of M penetrators within a volume V_S, then the penetrator spray density ρ is:

$$\rho = M/V_S \tag{69}$$

where V_S is the volume of a spherical "danger zone" that surrounds the spacecraft, within which the particle density is calculated. For the present research, this danger zone has a radius of 10,000 km unless otherwise stated. Once ρ has been calculated through debris

propagation modeling, the expected number of hits on a spacecraft's "hazard zone," with hazard zone volume V_{HZ}, is given by:

$$E = \rho V_{HZ} \tag{70}$$

Like the spacecraft fragmentation study by Bettinger and Hess [63], V_{HZ} defines a sphere around the spacecraft such that any particle that enters this volume is considered to have hit the spacecraft. The geometry of the spacecraft will be ignored for the present research and spacecraft survivability is determined with a hazard zone radius of 500 m. This volume is like an error ellipsoid around the spacecraft and avoids numerical precision issues related to determining the exact location of the spacecraft and debris particles at cislunar scales in the computer simulation.

With a probability of kill with a hit of $P_{K|H}$, or the probability that a particle will cause critical damage to the spacecraft given that it strikes it, the instantaneous probability of spacecraft hazard is given by:

$$P_{HZ} = 1 - e^{-EP_{K|H}} \tag{71}$$

The probability of spacecraft hazard P_{HZ} represents the probability that a particle that would cause critical damage to the spacecraft will enter the 500 m hazard zone sphere. In a real-world application, this may represent the probability that a spacecraft will be significantly threatened by debris and should perform an avoidance maneuver. For each simulation, the value of P_{HZ} is tracked over time. The total probability of hazard during a time interval t_0 to t_f is the area under the P_{HZ} curve with respect to time:

$$\int_{t_0}^{t_f} P_{HZ}\,(t)\,dt \tag{72}$$

This expression gives the total probability that a particle will strike the spacecraft and cause critical damage during the simulation.

As shown in Equation (71), the probability of hazard P_{HZ} depends on the chosen probability of kill with a hit, or $P_{K|H}$. Once the relative velocities of particles have been determined through simulation, an appropriate value for $P_{K|H}$ can be chosen based on the expected damage to spacecraft. Studies of damage caused by particle impacts can be used to inform the choice of $P_{K|H}$. Different models for $P_{K|H}$ are applied for the natural and artificial case studies due to differences in the debris properties, which would lead to different levels of risk with a debris particle impact. The models for $P_{K|H}$ used for analyzing risks from natural debris are discussed in Section 3.5.1, and the models for $P_{K|H}$ used for analyzing the risks from artificial debris are discussed in Section 3.5.2.

3.5.1. Probability of Kill with a Hit, Natural Debris

Chapter IV studies the risks to a spacecraft at L_4 or L_5 from natural particle accumulations in the Kordylewski clouds. For this study, a $P_{K|H}$ model that depends on particle velocity was applied. Since the mass properties of the Kordylewski clouds have been largely unstudied, debris particle mass was not included as a variable in the $P_{K|H}$ model. Instead, several $P_{K|H}$ models with different levels of assessed risk were developed to represent uncertainty in the mass distribution of particles in the Kordylewski Clouds.

Studies of damage caused by particle impacts can be used to inform the choice of $P_{K|H}$. The study by Elvidge [67] simulated hypervelocity hits to a spacecraft from different particle sizes and calculated the probability of a hit causing critical damage to the spacecraft. For particles 1 cm in size, this probability is 14.286%. The Kordylewski cloud

natural debris case study involves particles at lower relative speeds and slightly larger sizes, but this number may still serve as a rough estimate for $P_{K|H}$ at higher velocities. The study of low-velocity impacts conducted by Yasaka, Hanada, and Hirayama [68] is also useful due to the relatively low relative velocities of Kordylewski cloud particles about the stable Lagrange points. In this study, steel balls 9 mm in diameter were experimentally shot at aluminum honeycomb mesh targets at between about 50 and 200 m/s. These impacts all punctured the honeycomb mesh, thereby generating thousands of additional fragments. The particles only lost about 10-20% of their kinetic energy in the collision with the mesh, indicating that the particles would likely be able to travel deeper into the internal spacecraft structure after penetrating the outer wall.

Due to the wide range of particle relative speeds at the stable Lagrange points, a variable $P_{K|H}$ was used. A logistic curve was used to model this dependence of $P_{K|H}$ on the speed of particles relative to a spacecraft fixed at the Lagrange point. Low particle velocities that cannot penetrate the spacecraft's outer panels are extremely unlikely to cause severe damage, while the likelihood of kill for any particle that is moving fast enough to penetrate the spacecraft depends on factors other than speed, including the size of the particle, the location of the hit, and the angle of impact. This leads to a $P_{K|H}$ curve that increases slowly while the particle speed is low, begins to increase rapidly once particles become capable of penetrating the spacecraft, and eventually levels off as particles are moving fast enough to consistently penetrate the spacecraft. Similar logistic curves are often used to measure vulnerabilities for other applications, such as software vulnerability discovery [69], software security patch management [70], and the vulnerability of bridges to earthquakes [71][72].

The logistic model parameters used in this simulation are as follows:

$$P_{K|H} = \frac{\left(P_{K|H}\right)_{max}}{1 + e^{-k(v - v_m)}} \tag{73}$$

where $\left(P_{K|H}\right)_{max}$ is the maximum probability of kill with a hit at high impact speeds, v_m is the midpoint of the logistic curve (the speed where it is increasing the fastest), and k, is the growth rate of the curve.

Multiple estimates of the variation of $P_{K|H}$ with relative speed were generated by modifying the parameters of the logistic curve. With multiple logistic models for $P_{K|H}$, the effects of changing the model on P_{HZ} can then be determined. The logistic models include "upper bound" and "lower bound" cases to create an envelope within which the true $P_{K|H}$ at any given relative speed is likely to lie. These bounds are based on the studies by Elvidge [67] and Yasaka, Hanada, and Hirayama [68], and reflect the uncertainty in the true amount of damage that would be caused by particle impacts at various speeds. Factors including the masses of particles in the Kordylewski clouds, their shapes, and the orientation at which they impact the spacecraft surface are largely unknown; therefore, they were not incorporated in the survivability model and all act to increase the uncertainty of the $P_{K|H}$. The parameters of all logistic curves are shown in Table 5, and the logistic curves are plotted in Figure 13.

Table 5. Velocity-Dependent Logistic Model Parameters

Logistic Model Name	$(P_{K\|H})_{max}$	v_m	k
Lower Bound	0.05	150	0.04
Mid Lower	0.15	125	0.04
Baseline	0.2	100	0.04
Mid Upper	0.25	75	0.05
Upper Bound	0.35	50	0.07

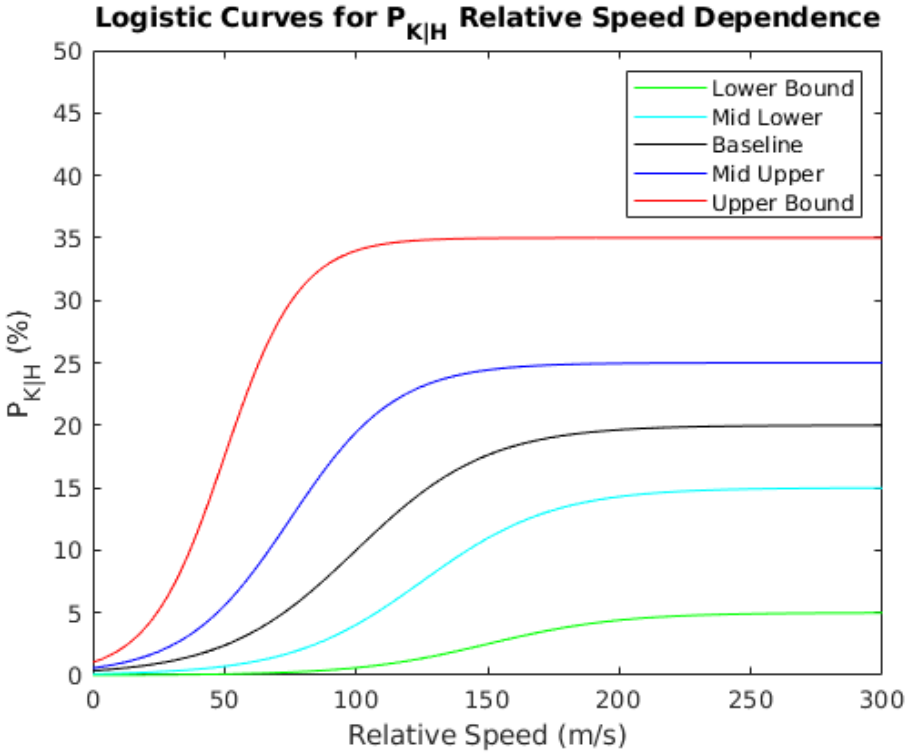

Figure 13. Plotted Velocity-Dependent Logistic Models

3.5.2. Probability of Kill with a Hit, Artificial Debris

For the artificial debris case studies, masses of debris particle are included in the simulation, and particles of different masses will pose different threats to spacecraft. To incorporate the variable risk posed by particles of different masses, a $P_{K|H}$ model that

depends on particle mass was applied in the artificial debris case studies. Velocity was not included as a variable in the artificial debris case studies, since particle mass is assumed to have a stronger relationship with collision damage; however, future research could incorporate a $P_{K|H}$ model that depends on both mass and velocity.

The study by Elvidge [67] was again used to inform the choice of the logistic curve parameters. $P_{K|H}$ was assumed to trend towards 100% as particle mass approaches 2 kg, which is the approximate upper limit of particle masses generated in the simulation. The equation for the mass-dependent logistic curve used in the artificial debris case studies is:

$$P_{K|H} = A + \frac{K - A}{(C + Qe^{-B*m})^{1/v}} \tag{74}$$

where m is particle mass, and the values chosen for the parameters A, B, C, K, Q, and v are given in Table 6. The resulting logistic model for $P_{K|H}$ is shown in Figure 14.

Table 6. Mass-Dependent Logistic Model Parameters

Parameter	Value
A	0
B	3
C	1
K	1
Q	0.1
v	0.05

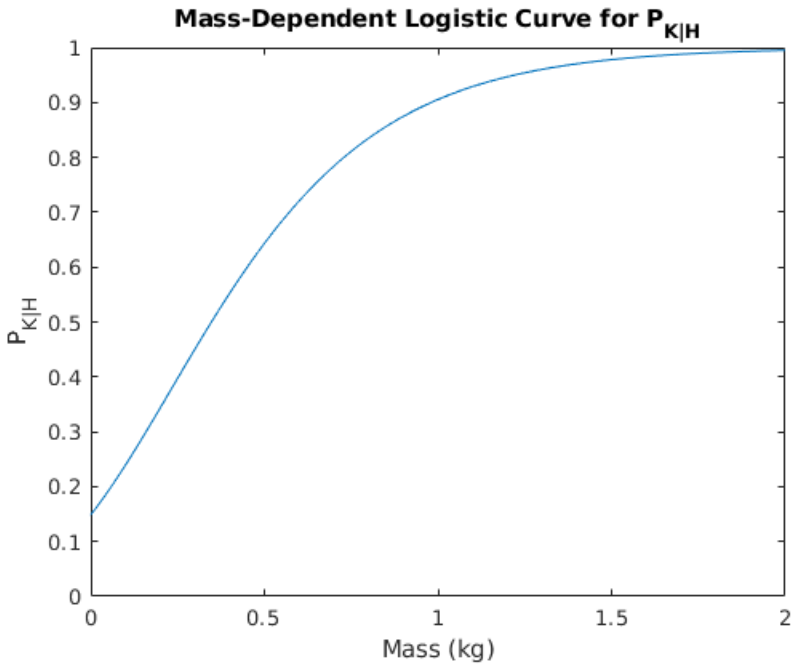

Figure 14. Mass-Dependent Logistic Curve Model

3.6. Summary

This chapter has provided the models for generating particle trajectories, simulating spacecraft catastrophic mishaps, and determining the survivability of spacecraft threatened by debris. Following a catastrophic spacecraft mishap, the trajectory of debris is calculated using the BCR4BP equations of motion, Equations (60)-(64), and the resulting trajectory is used to evaluate the risks to spacecraft using the Poisson survivability model. This process is completed for a variety of case studies, each with a unique set of initial conditions. The next two chapters, Chapter IV and Chapter V, present the results of these case studies.

IV. Analysis and Results: Natural Space Debris

4.1. Chapter Overview

A case study involving natural debris introduces the simulation of cislunar debris particles. The first case study in this research involves the simulation of particle accumulations in the Kordylewski clouds near the stable Earth-Moon Lagrange points L_4 and L_5 and an analysis of the resulting debris risks to spacecraft operating near these points. This research was accepted for publication in the *Advances in Space Research* journal.[3]

4.2. Case Study: Spacecraft Survivability in the Natural Debris Environment near the Stable Earth-Moon Lagrange Points

4.2.1. Motivation

The L_4 and L_5 points have been discussed as a potential location for long-term human colonization since at least 1974 [73]. With the increasing interest in cislunar space, L_4 and L_5 could gain more attention due to their ability to support a variety of unique civilian and military applications [74]. The L_4 and L_5 points are especially attractive locations for communications satellites due to their ability to enable complete coverage of both the Earth and Moon with low stationkeeping requirements [75]. The station-keeping requirements of L_4 and L_5 are lower than Earth orbits like GEO, enabling longer mission durations [74], and these points could be an alternative to GEO as the GEO environment becomes more crowded [76]. L_4 and L_5 have also been suggested as a location for future positioning, navigation, and timing (PNT) systems and cislunar Space Situational Awareness (SSA)

[3] Boone, N. R., Bettinger, R. A., "Spacecraft Survivability in the Natural Debris Environment near the Stable Earth-Moon Lagrange Points," *Advances in Space Research*, 2021.

platforms [74]. Furthermore, L_4 and L_5 have been proposed as possible locations for detection of solar magnetic storms, asteroid early warning systems, and relay communications spacecraft for deep space missions [76]. As interest in cislunar space architecture grows, the variety of potential uses for L_4 and L_5 increases the need to understand the space environment in the vicinity of these points.

While L_4 and L_5 could be useful to space operations due to their stability, this stability could also lead to an accumulation of natural or artificial debris. Debris collision risk has already been shown to increase near geopotential wells in geosynchronous orbit due to a higher concentration of debris at these locations [77], and a similar phenomenon may increase collision risk at the stable L_4 and L_5 points due to debris accumulation. The source of this debris could come from previously identified naturally occurring particle accumulations at L_4 and L_5. Several studies have investigated the existence of "Kordylewski clouds," which are natural accumulations of cosmic dust that have been observed near the Earth-Moon L_4 and L_5 points. Slíz-Balogh, Barta, and Horváth [8] noted in their study of the Kordylewski clouds that rock-sized particles should be able to circulate in the vicinity of the L_5 Lagrange point for a long time. The potential risk to spacecraft from these naturally occurring objects has been largely unstudied. In addition, while the present case study focuses on natural debris, artificial debris could also eventually become problematic if debris from spacecraft operating in cislunar space begins to collect near the stable Lagrange points, similar to the trapping of cosmic dust observed in the Kordylewski clouds. This could potentially reduce the reliability of future space missions that seek to take advantage of these useful locations, much like the "Kessler Syndrome" of lower Earth orbits [5].

This case study examines the collision risks to spacecraft due to natural particle accumulations in the Kordylewski clouds at the Earth-Moon L_4 and L_5 points. Using a trajectory model that incorporates the gravitational influences of the Earth, Moon, and Sun, the motion of particles trapped near the L_4 and L_5 points is observed over time and used to examine the collision risks to nearby spacecraft. Research into the motion of particles near the stable Earth-Moon Lagrange points will enable an improved understanding of the potential collision risks posed by the Kordylewski clouds and enhance operational planning for future Lagrange point space missions.

4.2.2. Initial Conditions

The natural debris particles comprising the Kordylewski clouds are assumed to be initially moving very slowly relative to the L_4 and L_5 Lagrange points and positioned in the vicinity of these points for this research. This is similar to the initial conditions used by Slíz-Balogh, Barta, and Horváth [8] in their study of the Kordylewski clouds. Particles are distributed randomly in position and velocity using random numbers generated from a standard normal distribution as shown in Table 7. Z_i represents a random number generated from the standard normal distribution, and these random numbers are scaled by 0.01 for positions and by 10^{-6} for velocities.

Table 7. Initial Conditions for Particles in the Vicinity of L_4 or L_5

Initial Condition	Value
x_0	$x_{0,L4/5} \pm Z_1 \times 0.01$
y_0	$y_{0,L4/5} \pm Z_2 \times 0.01$
z_0	$z_{0,L4/5} \pm Z_3 \times 0.01$
v_{x0}	$v_{x0,L4/5} \pm Z_4 \times 10^{-6}$
v_{y0}	$v_{y0,L4/5} \pm Z_5 \times 10^{-6}$
v_{z0}	$v_{z0,L4/5} \pm Z_6 \times 10^{-6}$

The simulation starts with a small number of particles, then moves to progressively greater numbers of particles, while tracking the density of the resulting particle cloud at the L_4 or L_5 point as more initial particles are simulated. Densities of the particle cloud for different initial numbers of particles are used to determine the probability of impact with a spacecraft, as discussed in the next section. The present research primarily focuses on larger particles that could cause significant damage in the event of an impact; on the order of about 1 cm in diameter and larger. Although the size distribution of particles in the Kordylewski clouds has not been identified in prior research, it is assumed that the particle size distribution is similar to the relative size distribution of interplanetary dust, meaning that there should be much fewer particles larger than 1 cm in diameter than there are very fine-grained dust particles. Therefore, the number of particles simulated is kept within a range of 500 to 10,000 particles. All particles are assumed to mass between about 10^{-10} kg and 10^{6} kg, since smaller particles are significantly affected by solar radiation pressure, and larger particles may have a non-negligible gravitational field [49].

4.2.3. Simulation Results

The following sections provide the results of the spacecraft survivability study for particles simulated using four-body dynamics at the L_4 and L_5 Lagrange points. For each Lagrange point, a baseline case of 500 particles simulated for one year is presented and used to analyze the general behavior of the particle motion and the survivability over time of a spacecraft fixed at L_4 or L_5. The variation of spacecraft survivability with initial particle number is then presented.

Spacecraft at L_4

The distribution of 500 particles about the L_4 Lagrange point according to the initial conditions in Table 7 is shown in Figure 15. The particles are initially generated according to a normal distribution and, as a result, 95% of the randomly generated particle initial positions will lie within a sphere of radius 6,323 km centered at L_4. The initial density of particles in particles/km^3 of the approximately 95% of particles within this sphere in terms of the number of particles simulated is given by:

$$\rho_{initial} = \frac{0.95 * N_{particles}}{\frac{4}{3}\pi(Z_{0.95} * R_{initial})} = \frac{0.95 * N_{particles}}{\frac{4}{3}\pi(1.645 * 0.01 * 384400 \text{ km})^3} \tag{75}$$

where $R_{initial}$ is the scale factor for the initial conditions as shown in Table 7 and $Z_{0.95}$ is the Z-score for the 95th percentile. The factor of 384,400 converts the distance measurement to kilometers from canonical units. For a simulation of 500 particles, the initial number density of the particles is approximately 4.5×10^{-10} / km^3.

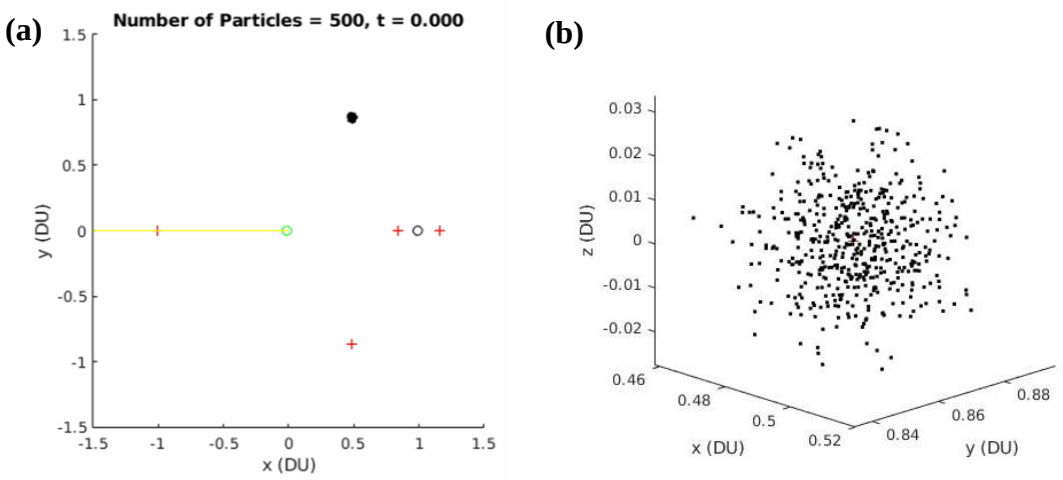

Figure 15. (a) Initial Particle Positions in Cislunar Space, (b) Zoomed Three-dimensional View of Initial Particle Positions about the L_4 Lagrange Point

The simulation begins with the Sun, Earth, and Moon initially positioned in a line ($\omega_1 t$ and $\omega_2 t$ in Figure 7 are zero). Particles are simulated using the BCR4BP trajectory model for one year, and the positions of particles are tracked at each time step. The positions of particles at several times during the simulation are shown in Figure 16. The yellow line indicates the direction of the Sun at the current time. These results appear very similar to those obtained by Slíz-Balogh, Barta, and Horváth [8] in terms of particle cloud shape. As solar perturbations act on the cloud, pinwheel-like structures form that rotate with the reference frame about the Lagrange point. These structures expand and collapse as solar perturbations act to move particles from one side of the Lagrange point to the other. Although the particles are stretched out from their initial position about the Lagrange point, 57% of the particles remain in the vicinity of the Lagrange point (considered to be within a 200,000-km radius of the point) after one year. At the end of the simulation, 80% of the particles remained in the Earth-Moon system, while 20% had either escaped the system or impacted the Earth or Moon.

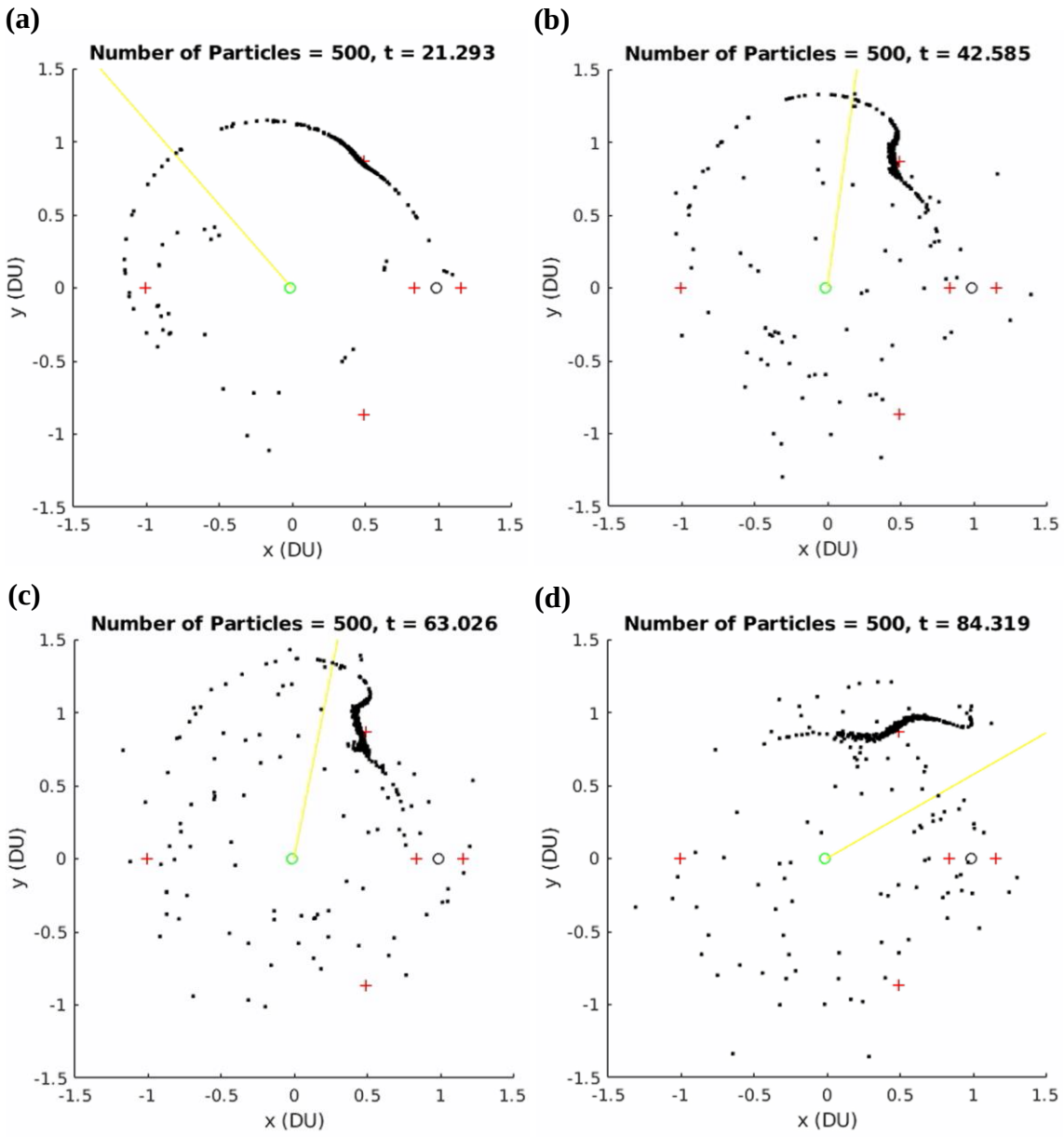

Figure 16. Particles at L_4 after (a) 92 days, (b) 185 days, (c) 274 days, (d) 366 days

After determining the trajectories of particles, the next step is to analyze the survivability of a spacecraft fixed at L_4. Figure 17 shows the number of particles inside the 10,000-km radius danger zone throughout the simulation along with the average relative speed of these particles. Although fewer particles enter the danger zone as solar perturbations spread out the particles, the relative speeds of the particles that do enter

greatly increase as the simulation progresses. These factors are combined in the spacecraft survivability model. The resulting probability of hazard (P_{HZ}) for each logistic model for $P_{K|H}$ is shown in Figure 18. As expected, the P_{HZ} is higher for logistic models from Figure 13 that use higher estimates for the $P_{K|H}$. The greatest dangers to spacecraft usually occur on a cycle. When solar perturbations act to pull particles from one side of the Lagrange point to the other, the pinwheel-like structures in the cloud collapse, causing more particles to enter the danger zone and at higher relative speeds. The largest spikes in probability of hazard were observed at 2 days, 46 days, 82 days, and 210 days after the simulation begins.

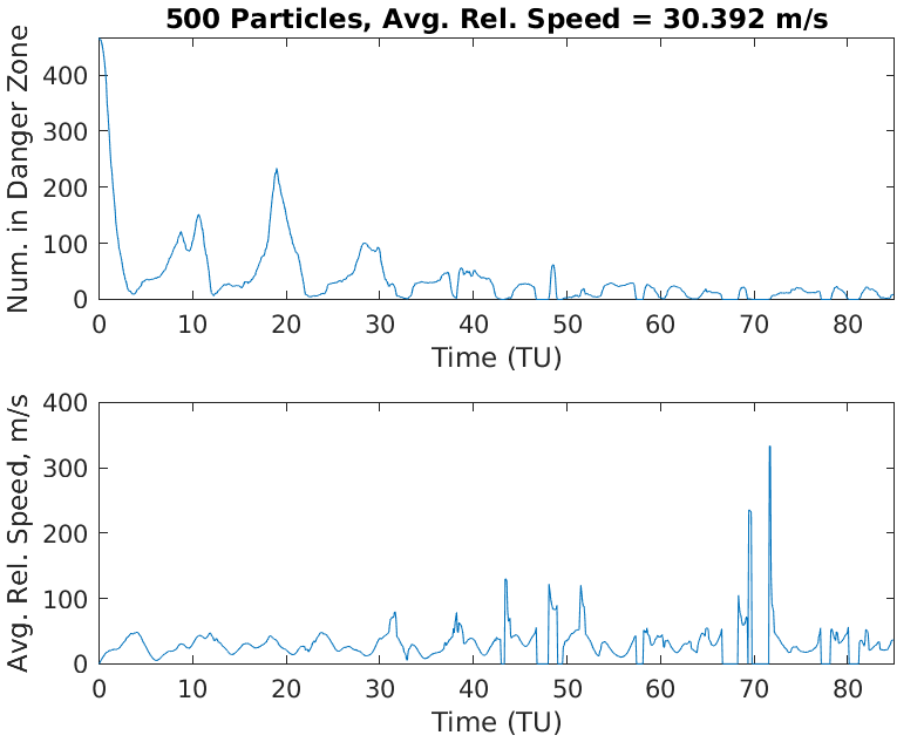

Figure 17. Number of Particles in the Danger Zone, and Average Relative Speed of those Particles (Spacecraft at L_4)

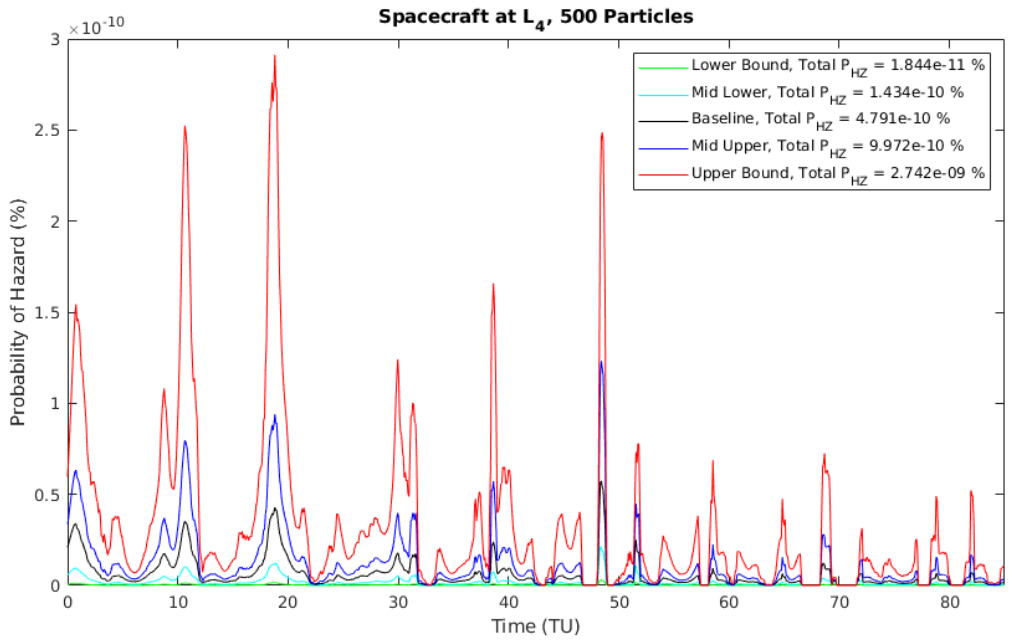

Figure 18. Probability of Hazard for 500-Particle Simulation (Spacecraft at L_4)

Analysis indicates that even with the effects of solar perturbations on particle motion, the probability of spacecraft hazard is incredibly low. Over the one-year simulation, the probability that the spacecraft is threatened by a particle is just 4.791×10^{-10} %. This low percentage is due to the vast distances in cislunar space and the small number of particles simulated. However, if more particles are simulated, then this probability of hazard will increase.

The P_{HZ} over one year from the simulation of 10,000 particles is shown in Figure 19. The total probability of hazard is an order of magnitude higher than the 500-particle simulation, but the trends in the probability of hazard over time are nearly identical. The largest spikes in probability of hazard are again observed at 2 days, 46 days, 82 days, and 210 days after the simulation begins.

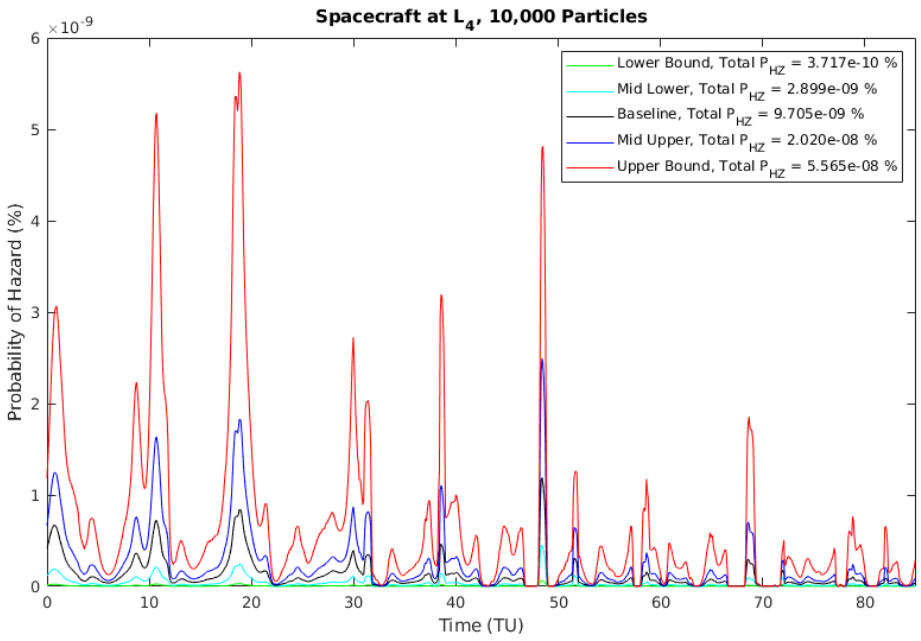

Figure 19. Probability of Hazard for 10,000-Particle Simulation (Spacecraft at L_4)

Figure 20 shows the change in the total probability of hazard over one year for different numbers of simulated particles, from 100 particles to 10,000 particles. For this range of simulated particles, the relationship between number of particles and probability of hazard is linear. A least-squares fit of the data yields the following linear model with a coefficient of determination (R^2) of 0.9999:

$$P_{HZ} = (9.704 \times 10^{-13})N_{particles} + 2.403 \times 10^{-11} \quad (76)$$

However, the relationship between P_{HZ} and the number of particles likely changes for simulations with more particles, likely becoming nonlinear at certain points; future studies featuring larger numbers of particles could analyze this behavior.

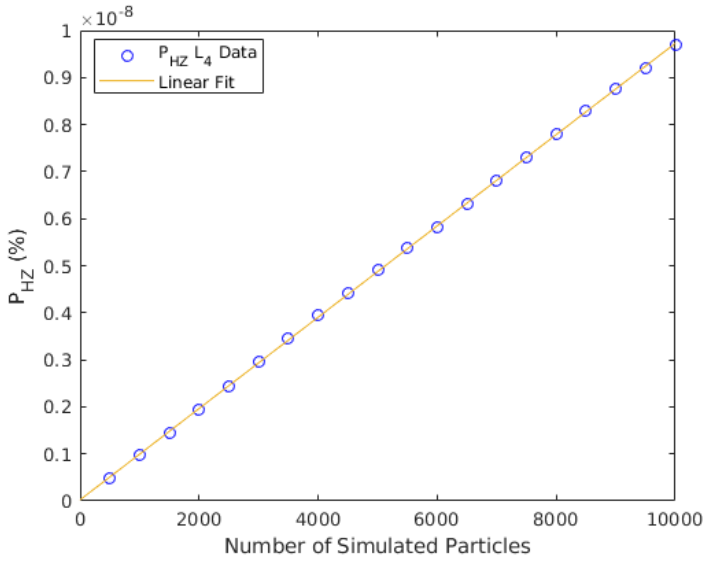

Figure 20. Probability of Hazard for Different Simulated Particle Numbers (Spacecraft at L_4)

Spacecraft at L_5

To analyze threats due to particles at the L_5 Lagrange point, particles are distributed about L_5 according to the initial conditions shown in Table 7. As with the simulation of particles about L_4, the motion of the particle cloud is propagated for one year according to the BCR4BP equations of motion, and the positions of the particles at various times during the year are shown in Figure 21. The shape of the cloud at various time points differs slightly from the behavior of the L_4 cloud, but the general pinwheel-like motion, with periodic collapses of the cloud structure, is still present in the L_5 cloud. A similar percentage of the particles remain within a 200,000-km radius of L_5 (59%) as were present in the vicinity of L_4 in the previous simulation. The percentage of particles that have not left the Earth-Moon system or impacted the Earth or Moon is also similar (85%).

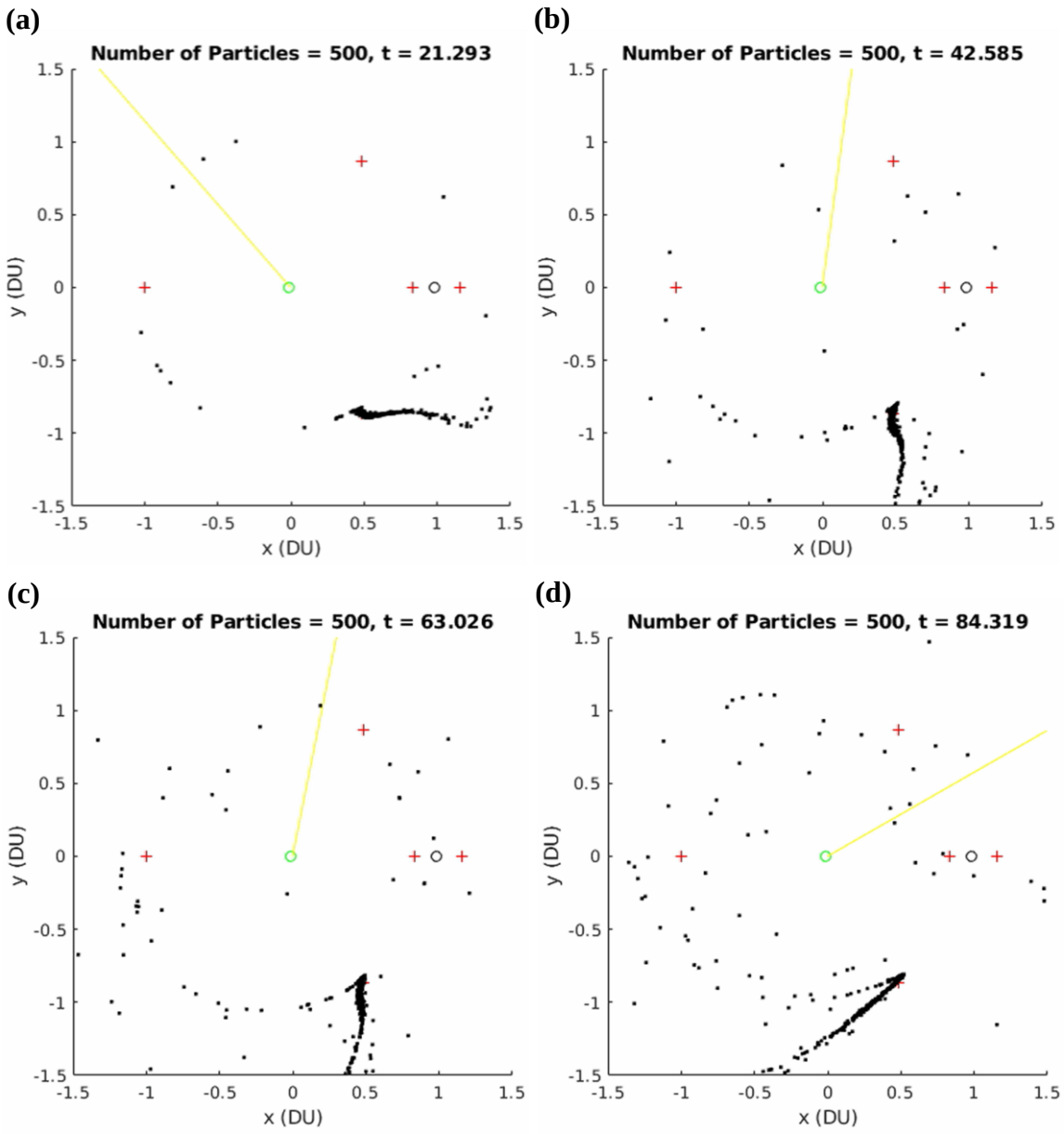

Figure 21. Particles at L_5 after (a) 92 days, (b) 185 days, (c) 274 days, (d) 366 days

The same parameters used to assess survivability at L_4 are applied at L_5 to examine the threats to a spacecraft operating at L_5. The number of particles inside the 10,000 km radius danger zone and the average relative speed of those particles throughout the simulation is shown in Figure 22. The probability of hazard is shown in Figure 23. The total probability of hazard is extremely low (4.860×10^{-10} %), but slightly larger than the probability of

hazard at L_4. The largest probabilities of hazard are again observed whenever the cloud collapses in on itself due to solar perturbations. However, these peaks occur at different times when compared to the simulation at L_4. The largest probabilities of hazard occur 3 days, 73 days, 159 days, 204 days, and 293 days after the start of the simulation.

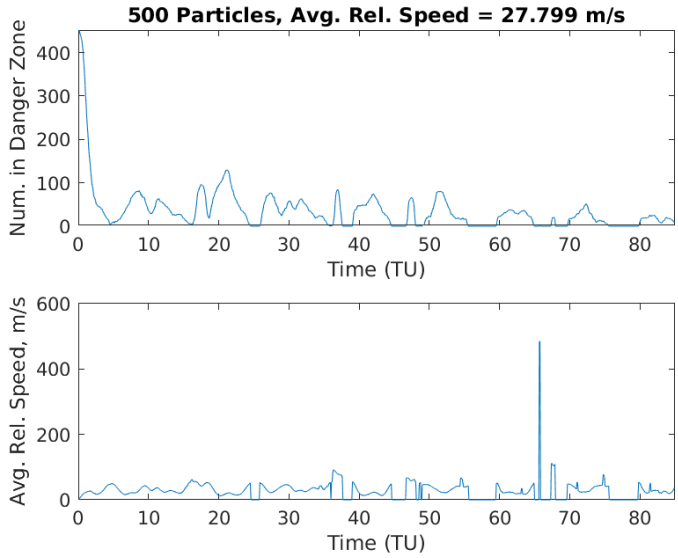

Figure 22. Number of Particles in the Danger Zone, and Average Relative Speed of those Particles (Spacecraft at L_5)

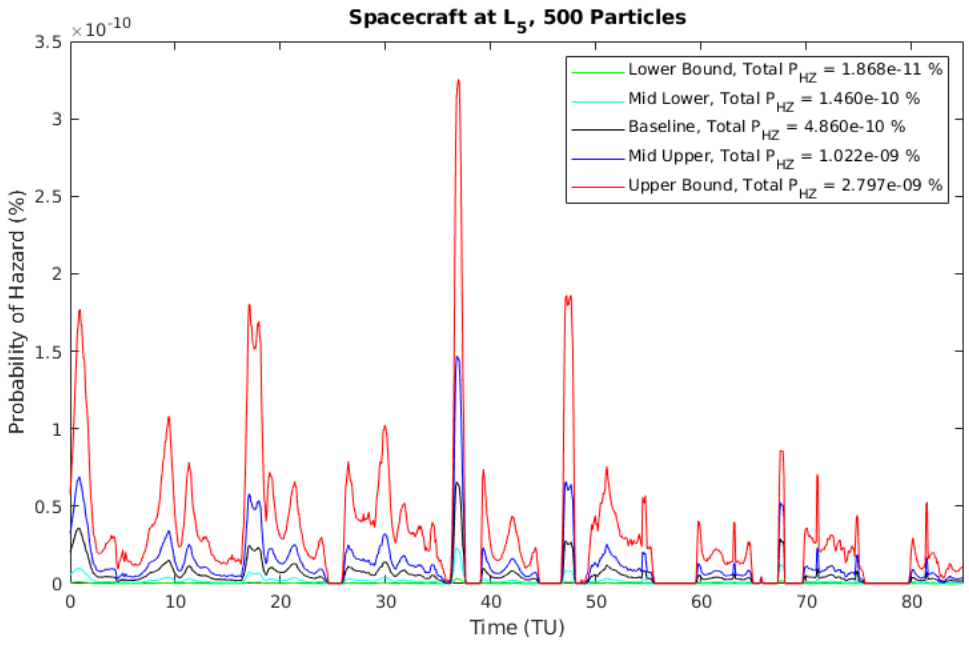

Figure 23. Probability of Hazard for 500-Particle Simulation (Spacecraft at L_5)

The P_{HZ} for the simulation of 10,000 particles is shown in Figure 24, and the variation of probability of hazard with number of particles is shown in Figure 25. The data from the L_4 simulation (shown in Figure 20) is included for reference. The linear curve of best fit for the L_5 data is given by:

$$P_{HZ} = 9.958 \times 10^{-13} N_{particles} - 1.606 \times 10^{-11} \tag{77}$$

The R^2 value is equal to 1 to within four decimal places.

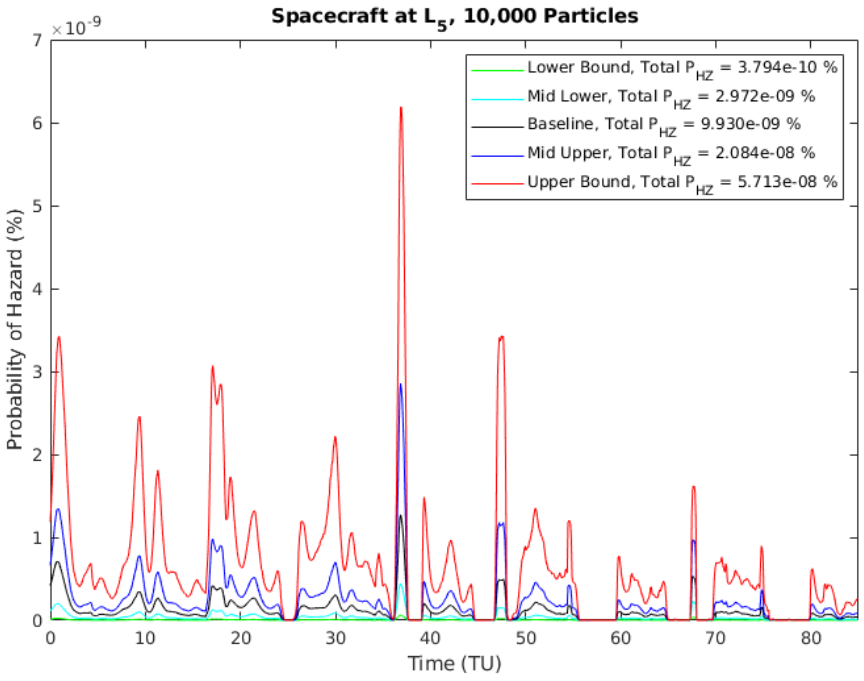

Figure 24. Probability of Hazard for 10,000-Particle Simulation (Spacecraft at L_5)

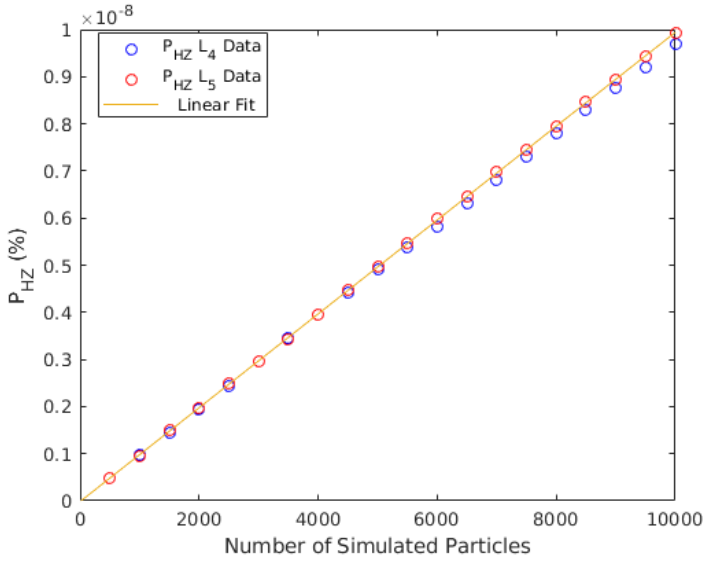

Figure 25. Probability of Hazard for Different Simulated Particle Numbers (Spacecraft at L_5)

4.2.4. Conclusion

With the particle densities assumed in this case study, the risk of damage from collision with natural debris comprising the Kordylewski clouds to a spacecraft operating at L_4 or L_5 is very low. For 10,000 particles simulated at the L_4 Lagrange point, the baseline survivability model resulted in a 9.702×10^{-9} % chance that one of those particles will substantially threaten the spacecraft; for 10,000 particles at L_5, the probability of hazard is 9.927×10^{-9} %. The logistic models that used lower estimates for $P_{K|H}$ resulted in lower total P_{HZ} than the baseline, and the logistic models that used higher estimates for $P_{K|H}$ resulted in higher total P_{HZ} than the baseline, as expected. This forms an envelope for the expected true P_{HZ}.Within the range of simulated particles (500 to 10,000) the collision risk scales linearly with particle density. An improved understanding of the particle density and size distribution in the Kordylewski clouds, studies with larger numbers of particles, as well as including natural debris mass flux along the boundaries of the Earth-Moon system would improve overall risk quantification. Longer simulations could also determine if equilibrium particle clouds begin to form as the number of particles escaping the vicinity of L_4 or L_5 approaches zero. Additionally, the logistic curve models for $P_{K|H}$ could be further refined, potentially with more studies of the damage caused by particle impacts at speeds up to 200 m/s. Particle mass could also be added as a component of the logistic model to analyze the effects of particles of different sizes in the Kordylewski clouds.

Although the collision risk to spacecraft is very low, steps may be taken to further lower this risk. Protection could be added to sensitive components on spacecraft to ensure that impacts from particles of various sizes moving at relative speeds of around 30-100 m/s

cannot penetrate the shielding. This research has also identified particularly high risks at certain times of the year when solar perturbations act to pull the particles through the Lagrange point at high relative speeds. The spacecraft could be maneuvered to a safer location near the Lagrange point to avoid damage from particle impacts during those time periods. Future research could determine the optimal trajectory of a spacecraft about the stable Lagrange points to minimize particle impacts.

4.3. Summary

This chapter has provided a case study in the risks from natural cislunar debris accumulation at L_4 and L_5 as an introduction to cislunar debris propagation. In the next chapter, the full catastrophic spacecraft mishap model is applied to examine a variety of cislunar artificial debris case studies.

V. Analysis and Results: Artificial Debris

5.1. Chapter Overview

This chapter presents the results of the artificial debris case studies. Each case study examines a catastrophic spacecraft mishap in a particular pre-explosion trajectory. The effects of the catastrophic mishap are analyzed in terms of the trajectories of the resulting debris particles and the threats to one or more notional spacecraft operating elsewhere in cislunar space. The risk is quantified according to the survivability model discussed in Chapter III, using the $P_{K|H}$ model for artificial debris. The five case studies presented include simulation of catastrophic mishaps at the collinear Earth-Moon Lagrange points, during an Apollo-like transfer, in the L_1 manifold, at the stable Earth-Moon Lagrange points, and in lunar orbit. The collinear Lagrange point study has been accepted as an IEEE 2021 conference paper; the Apollo-like transfer, the L_1 manifold, and stable Earth-Moon Lagrange point studies were accepted as a SciTech 2021 conference paper; and the lunar orbit debris study is a DCASS 2021 conference presentation.[4]

5.2. Case Study: Mishap at the Collinear Earth-Moon Lagrange Points

5.2.1. Motivation

Several recent missions in cislunar space have sought to utilize the collinear Earth-Moon Lagrange points to complete their missions. For example, China's recent Chang'e-4 far side lunar lander was accompanied by the Queqiao relay satellite orbiting the Earth-Moon L_2 Lagrange point [1]. The L_2 point is an appealing location for communications spacecraft

[4] For a complete listing of scholarly efforts related to this Thesis, see Section 6.2.1.

because it enables constant communication with both the far side of the Moon and the Earth. The manned Lunar Orbital Platform-Gateway (LOP-G, or Gateway) station will also utilize the dynamics of the Earth-Moon Lagrange points when it becomes operational. The Gateway is a crucial part of NASA's Artemis program to return humans to the Moon and will utilize a Near Rectilinear Halo Orbit (NRHO) to enable exploration of the Moon. NRHOs are families of halo orbits about the L_1 and L_2 Lagrange points that are nearly stable, enable constant communication with the Earth, and pass close to the Moon [78][79].

As more spacecraft operate near the Lagrange points, an accurate understanding of the debris-related consequences of a spacecraft mishap in this orbital regime is needed. The complex dynamics of cislunar space, especially near the unstable Lagrange points L_1 and L_2, make it difficult to predict the motion of debris particles and the threat they could pose to operational spacecraft, including the proposed Gateway. Although the threat of artificial debris in lower Earth orbits has been heavily studied, few studies have investigated the effects of similar fragmentation events in cislunar orbits. With plans to build a manned space station in this region, it becomes even more important to understand the threats from debris in cislunar space.

This case study involves the theoretical analysis of the short- and long-term motion of artificial space debris generated by a catastrophic spacecraft mishap in the vicinity of the collinear Earth-Moon Lagrange points L_1 and L_2 and an analysis of the risks the mishap would pose to notional spacecraft elsewhere in cislunar space. These notional spacecraft include the Lunar Gateway, a spacecraft near L_1, a spacecraft near L_2, and a spacecraft conducting a low-energy transfer to the Moon. The survivability of each spacecraft is

analyzed for the case where the catastrophic mishap occurs at L_1 and the case where the catastrophic mishap occurs at L_2.

5.2.2. Initial Conditions

Prior to suffering the catastrophic mishap, the spacecraft at L_1 and L_2 are assumed to be exactly at those points. Although a real spacecraft would likely be orbiting L_1 or L_2 in a halo orbit prior to the explosion, the spacecraft are assumed to be located exactly at L_1 or L_2 for the purposes of this simulation for simplicity. This assumption reduces the number of simulations that must be conducted and should accurately approximate a spacecraft in a small halo orbit.

5.2.3. Notional Spacecraft Trajectories

The BCR4BP trajectory model was used to generate the trajectories of the notional spacecraft (the spacecraft for which the debris risks are determined) for the simulation. The notional spacecraft studied in the present research are the Gateway, a spacecraft fixed at L_1, a spacecraft fixed at L_2, and a spacecraft that transfers between the Earth and Moon using the Earth-Moon stable manifold. No trajectory simulation was conducted for the spacecraft at L_1 and L_2, since they were assumed to be fixed at the Lagrange points, but the BCR4BP trajectory model was applied to generate trajectories for the Gateway and the transfer spacecraft.

The initial conditions for the Gateway were obtained from the CR3BP periapsis condition in Williams et al. [80]. These initial conditions were propagated for one complete orbit. This orbit, shown in Figure 26, was used as the trajectory of the Gateway for the simulation. This orbit belongs to the L_2-South family of NRHO orbits. This orbit is a likely

choice for the Gateway due to its long period over the lunar south pole, enabling it to support colonization efforts in that region of the Moon [79][80].

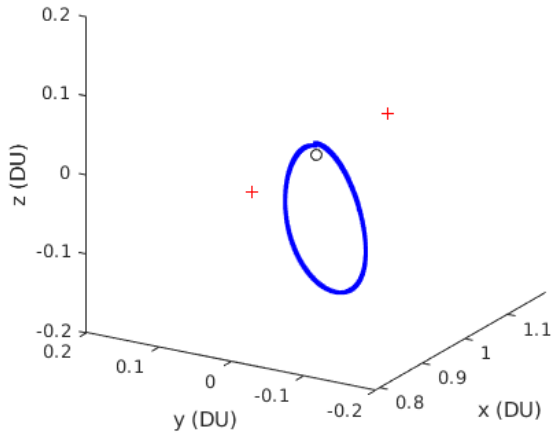

Figure 26. Gateway Reference Trajectory

The Gateway was assumed to be positioned at one of four locations along its orbit at the time of the catastrophic spacecraft mishap. For each debris case study involving the Gateway, the simulation was conducted four times to study the changes in survivability with the initial position of the Gateway. The four initial positions of the Gateway that were considered are shown in Figure 27.

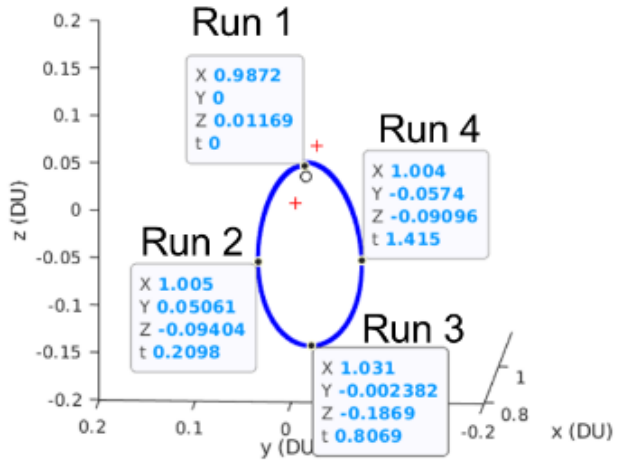

Figure 27. Initial Positions of the Gateway

The second notional spacecraft for which the BCR4BP trajectory model was applied is a theoretical future spacecraft that transfers from the Earth to the Moon along the stable manifold of the Earth-Moon CR3BP. The manifolds of the Earth-Moon system can enable transfers between Earth orbits and Lagrange point or lunar orbits for less fuel than a conventional Hohmann transfer and are an ongoing topic of research [17][18]. Manifolds have been used before for missions to the Sun-Earth Lagrange points, and the L_1 manifold of the Sun-Earth system is especially useful because intersects the Earth. Unlike the Sun-Earth L_1 manifold, the Earth-Moon L_1 manifold does not intersect the Earth, requiring the use of a trajectory segment that connects low Earth orbits to the manifold [18].

The stable and unstable manifolds that extend from L_1 towards Earth are shown in Figure 28. In this figure, the arrows extending from L_1 represent the stable/unstable eigenvectors of the CR3BP plant matrix linearized about the L_1 point. The manifolds are then determined by propagating the trajectory of a particle displaced slightly along the stable/unstable eigenvectors. The unstable manifold extending towards Earth (red) is found by propagating forwards in time, while the stable manifold (blue) that brings particles towards the L_1 point is found by propagating backwards in time. The arrows on the manifold lines indicate the direction of travel in forward time. These manifold lines form the center of manifold tubes that bring spacecraft to and from the L_1 point. Note that the stable and unstable manifolds connect.

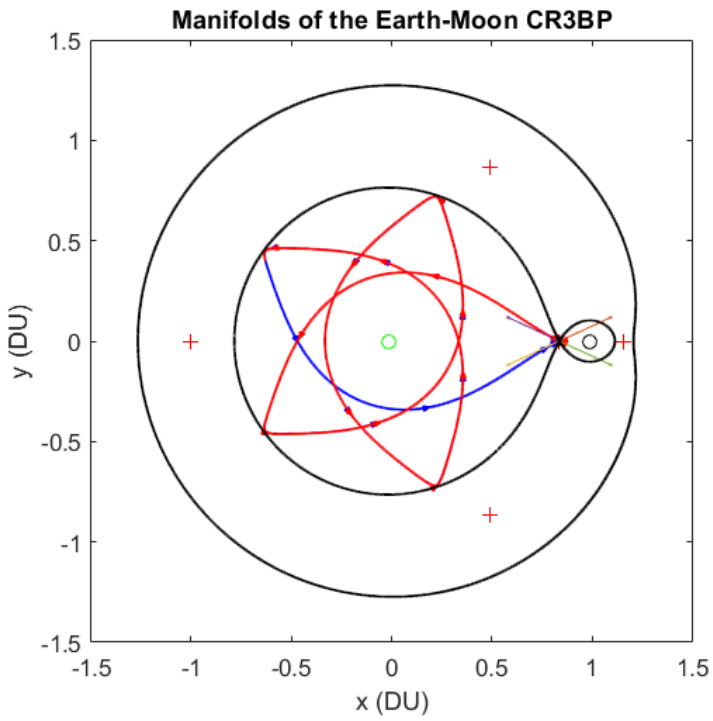

Figure 28. Manifolds of the L_1 Lagrange Point in the Earth-Moon System

To simulate the trajectory of a spacecraft that transfers between the Earth and the Moon, the direct transfer method to L_1 described by Parker and Anderson [18] was used as a guide. This trajectory involves the use of a "bridge" segment that connects a parking orbit around the Earth to the stable manifold. Two burns are required; the first to exit the parking orbit, and the second to enter the stable manifold. For the present research, only the manifold segment was simulated to study the effects of the cislunar debris field on the spacecraft. Therefore, the trajectory for the transferring spacecraft starts with the spacecraft on the stable manifold at the stable manifold's lowest y-position and ends when the spacecraft has reached its closest approach to the Moon.

5.2.4. Simulation Results, Mishap at L_2

The simulations of an L_2 catastrophic spacecraft mishap begin with the Sun, Earth, and Moon all in a line, and the debris particles are simulated for 50 days following the explosion unless otherwise stated. The Gateway simulation was conducted four times, with the Gateway initially positioned at the four positions shown in Figure 27. The simulations for the other notional spacecraft were only conducted once.

Lunar Gateway Run 1

Plots of the positions of debris particles at selected times following the catastrophic mishap are shown in Figure 29. The green circle marks the location of the Earth, the black circle marks the location of the Moon, the blue star marks the current location of the Gateway, the red crosses mark the Lagrange points, the yellow line represents the Sun vector, and the black dots are debris particles.

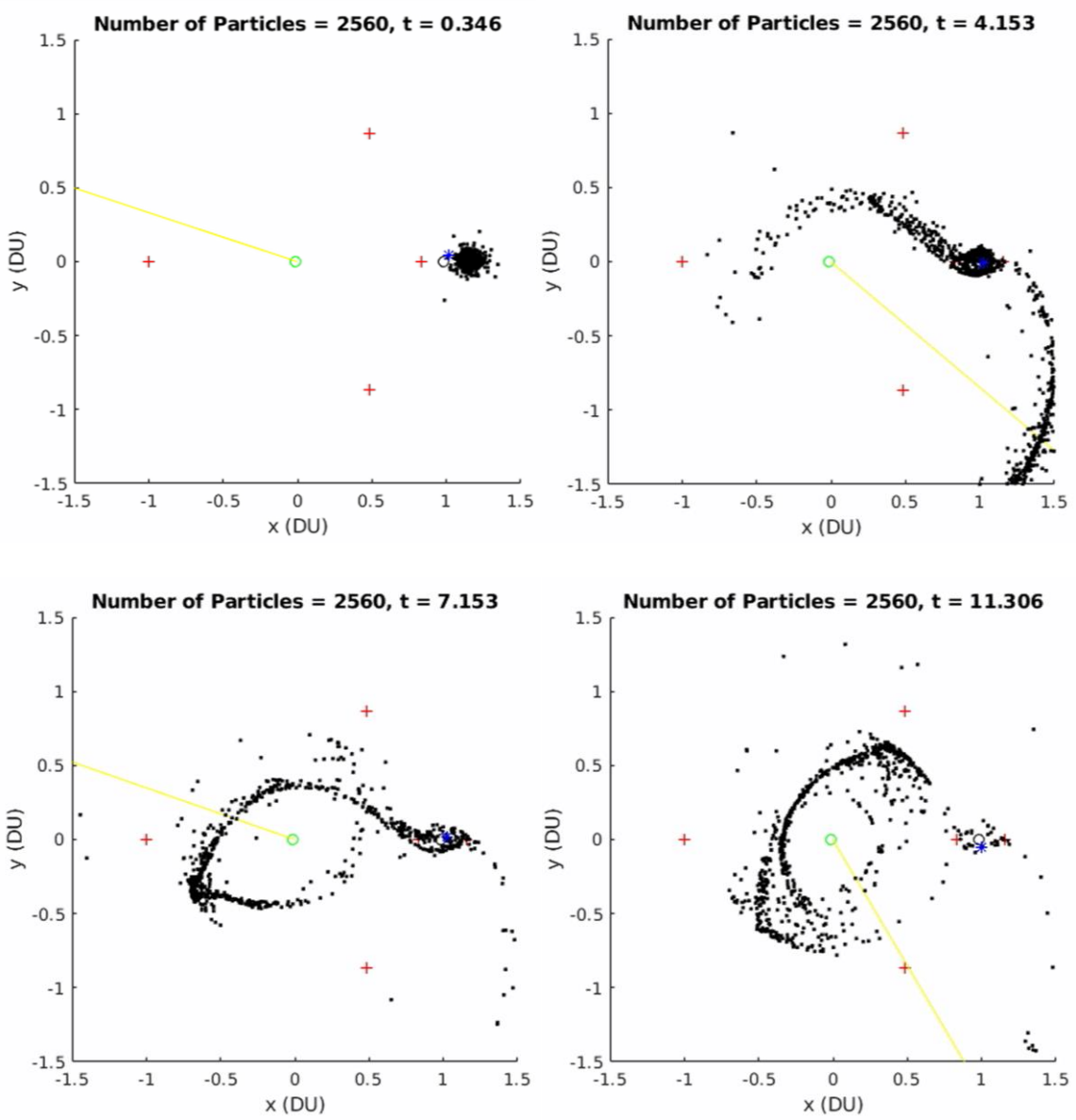

Figure 29. Positions of Debris Particles During Simulation: Mishap at L_2, Gateway Run 1

The simulated debris particles expand rapidly from the Lagrange point at the start of the simulation due to the violent nature of the explosion, then are quickly pulled away from the Lagrange point as they are affected by the gravitational forces of the Moon, Earth, and Sun. The particles stream away from the Lagrange point along the unstable manifold tubes of the CR3BP. The unstable manifold tubes carry particles that have about the same energy

level as the Earth-Moon Lagrange points away from those points, creating a cloud of debris particles in the manifold, similar to what was noted in the Sun-Earth CR3BP by Landgraf and Jehn [60]. This transfers particles either towards lower Earth-centered orbits or away from the Earth-Moon system. At the end of the simulation, most particles have either entered Earth orbit or escaped from the system. All particles that leave a cube with side lengths 5 DU centered at the Earth-Moon barycenter are considered to have escaped the system.

The final status of all particles in the simulation is shown in Table 8. Most particles have either escaped the Earth-Moon system or entered the Earth sphere of influence, where they do not threaten the Gateway. For the particles that have entered Earth orbits, the orbital elements of the particles at the simulation end time are shown in Figure 30. Note that these orbital elements are with respect to an Earth-Centered Inertial (ECI) frame aligned with the rotating frame at $t = 0$, so the inclination given is with respect to the Earth-Moon line, not the Earth's equator. All particles are in similar orbits since all particles have approximately the same Jacobi Constant. These Jacobi Constants are the same as that of the L_2 Lagrange point, plus a random factor due to the velocities given by the catastrophic mishap. The average particle perigee is 126,000 km (33% to the Moon), and the average particle apogee is 298,000 km (77% to the Moon). For reference, geosynchronous altitude is 42,164 km. Note that no particles pass within geosynchronous altitude.

Table 8. Status of Particles at the End of Simulation: Mishap at L_2, Gateway Run 1

Status at Simulation End	Count	Percentage
Escaped the Earth-Moon System	1651	64.49%
Impacted the Moon	138	5.39%
Impacted the Earth	0	0%
In the Lunar Sphere of Influence	28	1.09%
In the Earth Sphere of Influence	743	29.02%

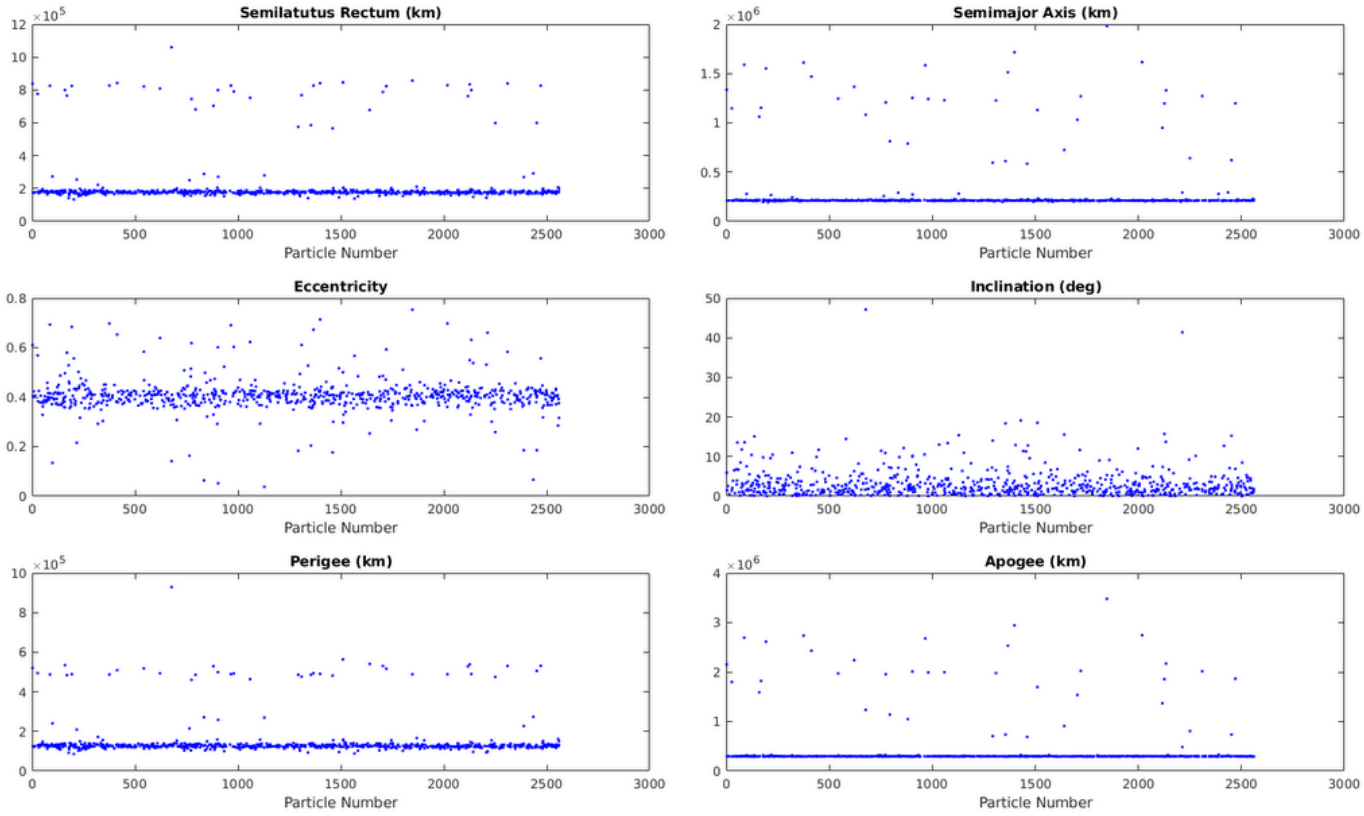

Figure 30. Orbital Elements of Earth-Orbiting Particles: Mishap at L_2, Gateway Run 1

Applying the Poisson survivability model enables a quantification of the debris risks to the Gateway during this simulation. The number of particles that pass within the Gateway's danger zone, the average speed of those particles relative to the Gateway, and the average mass of those particles is plotted throughout the simulation in Figure 31. The probability of hazard calculated throughout the simulation is shown in Figure 32. These results show

that the risk to the Gateway is extremely low. Due to the vast distances in cislunar space, and how quickly the particles escape the vicinity of the Moon, the chances of a debris particle striking the Gateway and causing critical damage are near zero. The closest approach by a particle to the Gateway was 1,435 km.

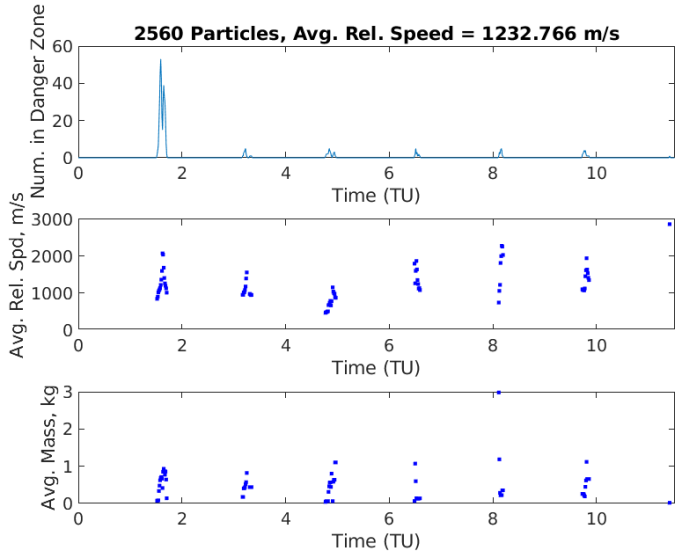

Figure 31. Statistics for Particles in Danger Zone: Mishap at L_2, Gateway Run 1

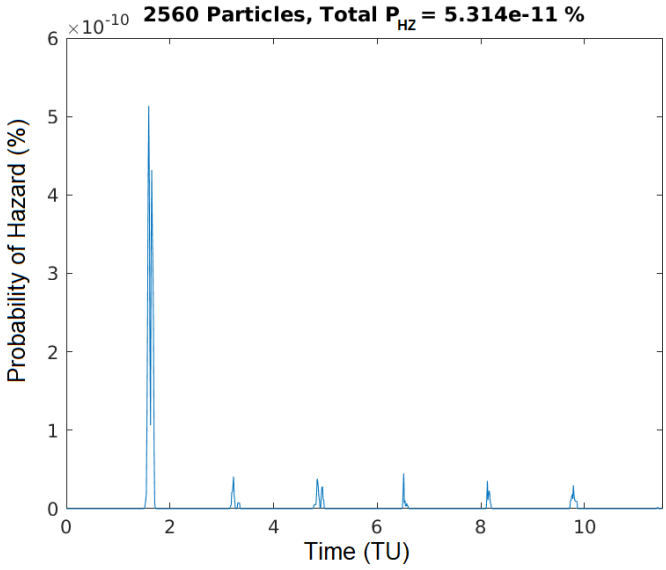

Figure 32. Probability of Hazard for the Gateway: Mishap at L_2, Gateway Run 1

Lunar Gateway Runs 2-4

The results for the remaining simulations, with the Gateway at different initial positions, are very similar. The closest particle approaches to the Gateway and the total probability of hazard are shown in Table 9. The greatest risk to the Gateway occurs for Run 4, since the spacecraft is moving up into the debris field when the catastrophic mishap occurs.

Table 9. Results for L_2, Gateway Runs 1-4

Run	Closest Approach to Gateway	Total P_{HZ}
1	1,435 km	5.314e-11 %
2	1,193 km	5.808e-11 %
3	1,295 km	7.455e-11 %
4	1,095 km	9.221e-11 %

Spacecraft at L_1

The particles that stream through the unstable manifold and cross the L_1 point suggest possible risks to a spacecraft operating near L_1 if a mishap occurs at L_2. In the next simulation, the notional spacecraft was assumed to be fixed at L_1, and the spacecraft that suffers the catastrophic mishap was assumed to be initially fixed at L_2.

The statistics for the particles that enter the danger zone are shown in Figure 33. Once particles begin streaming through the L_1 Lagrange point, the number of particles in the Danger Zone begins to sharply increase. Average particle mass steadily increases as the particles pass through the L_1 point, because smaller particles were given more ΔV from the explosion and reach the Lagrange point more quickly. The average relative speeds are far lower in this case, since the L_1 point is stationary relative to L_2.

The probability of hazard for the spacecraft at L_1 is shown in Figure 34. The total probability of hazard is much higher than what was observed in the Gateway simulation,

and the risk to a spacecraft at L_1 is about 13 to 23 times higher than the risk to the Gateway when the mishap occurs at L_2. The closest approach by a particle to the spacecraft is 161 km.

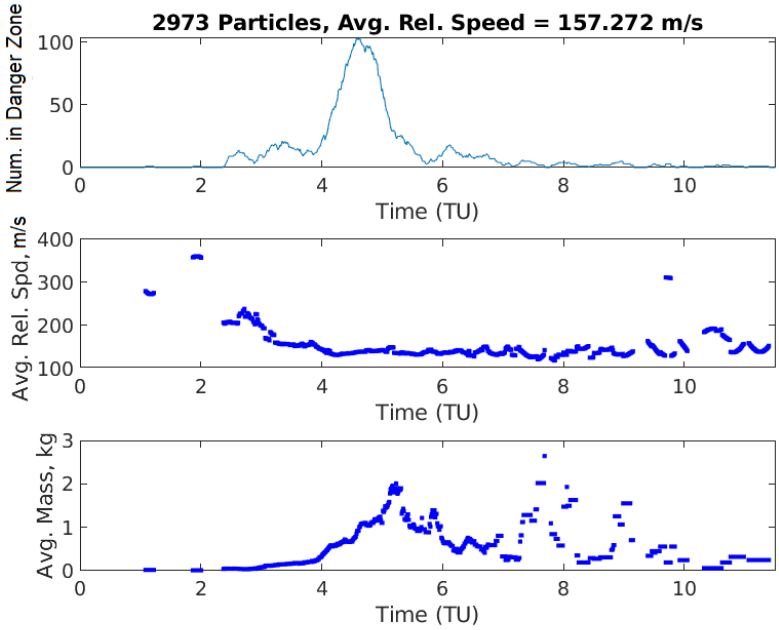

Figure 33. Statistics for Particles in Danger Zone: Mishap at L_2, Spacecraft at L_1

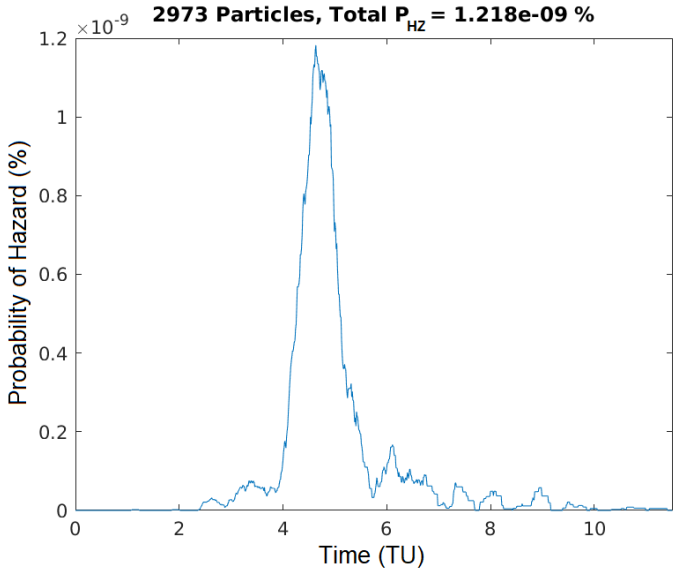

Figure 34. Probability of Hazard: Mishap at L_2, Spacecraft at L_1

Spacecraft in Earth-Moon Transfer

The particles that accumulate in the manifolds of the Earth-Moon CR3BP could create hazards to spacecraft that utilize these manifolds for transfers. In the next simulation, the threats to a notional spacecraft traveling along the stable manifold between the Earth and the Moon are analyzed.

The simulation begins at -19 TU, and the transfer spacecraft begins traveling along the unstable manifold at 0 TU. Starting the simulation 19 TU before the spacecraft transfers provides enough time for the debris particles to spread through the manifolds. The simulation is then conducted for an additional 3 TU, which is enough time for the spacecraft to transfer to the Moon. A snapshot of the debris simulation, showing the spacecraft transferring along the stable manifold, is shown in Figure 35.

The statistics for particles that enter the danger zone are shown in Figure 36, and the probability of hazard for the transferring spacecraft is shown in Figure 37. The risk to the spacecraft is on the same order of magnitude as the risk to the Gateway. The closest approach by a particle to the spacecraft is 1,425 km.

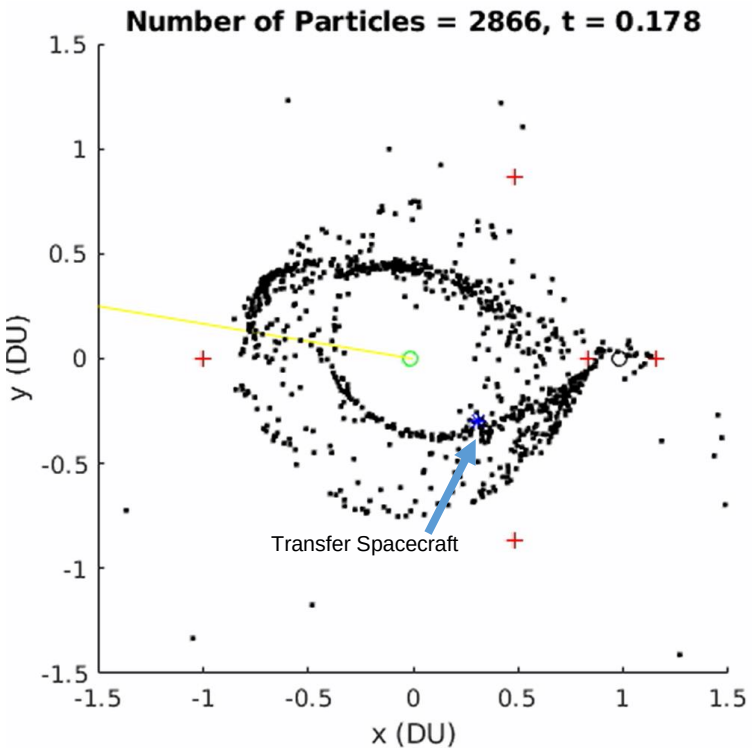

Figure 35. Snapshot of Debris Particles Relative to Spacecraft During Simulation: Mishap at L_2, Spacecraft Transferring

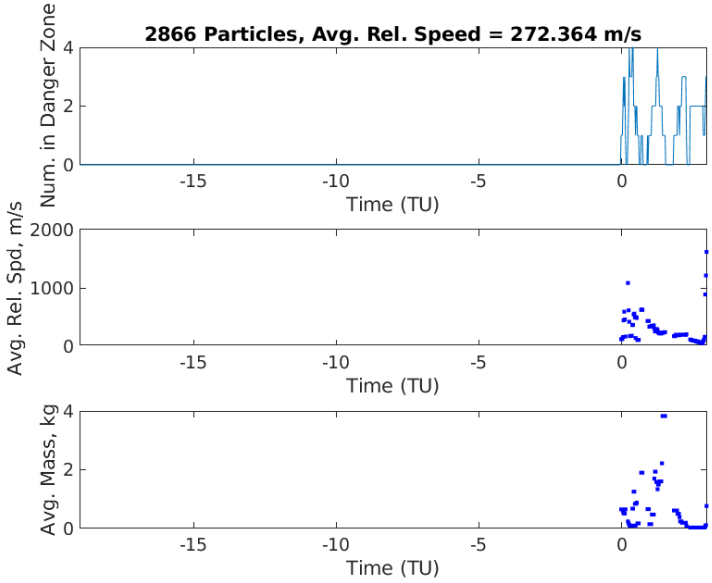

Figure 36. Statistics for Particles in Danger Zone: Mishap at L_2, Spacecraft Transferring

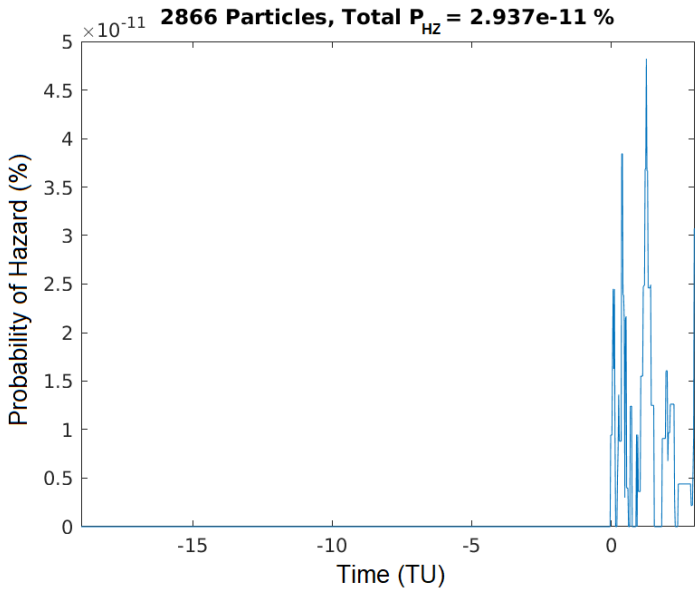

Figure 37. Probability of Hazard: Mishap at L_2, Spacecraft Transferring

5.2.5. Simulation Results, Mishap at L_1

The analysis conducted at L_2 was repeated for a catastrophic spacecraft mishap that occurs at L_1. The simulation again begins with the Sun, Earth, and Moon all in a line, and the debris particles are simulated for 50 days following the explosion unless otherwise stated. The Gateway simulation was conducted four times, with the Gateway initially positioned at the four positions shown in Figure 39.

Gateway Run 1

Plots of the positions of debris particles during the simulation are shown in Figure 38. The trajectories of the debris particles are very similar to the L_2 case, with debris filling the unstable manifold. However, particles enter the manifold much more quickly, far more particles become trapped near the Moon, and far fewer particles exit the Earth-Moon system.

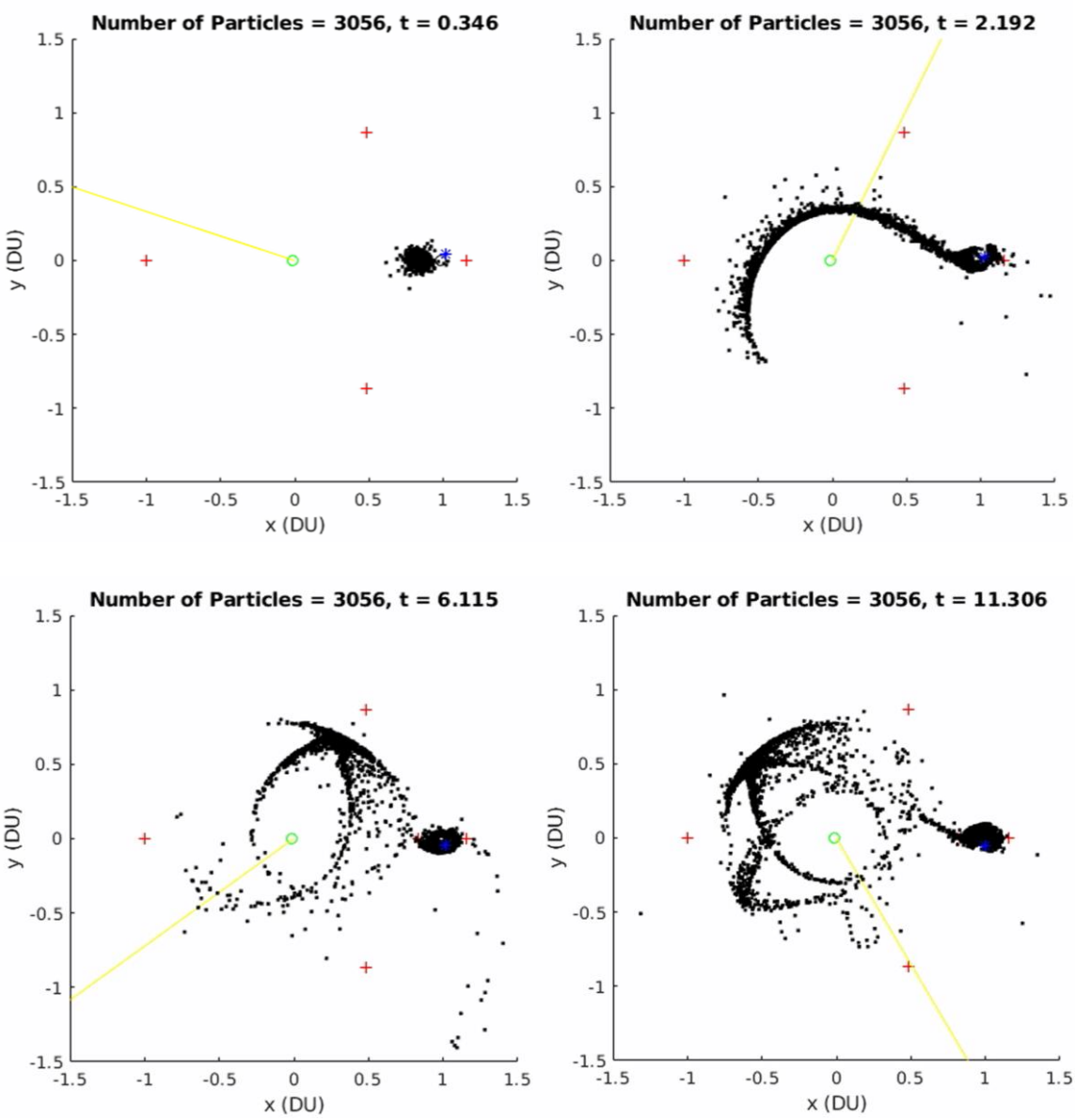

Figure 38. Positions of Debris Particles During Simulation: Mishap at L_1, Gateway Run 1

The status of all particles at the end of the simulation is shown in Table 10. The particles that remain in the lunar sphere of influence are potentially problematic for the Gateway since these particles could threaten the Gateway on each orbit. For the Earth-orbing particles, the orbital elements of the particles are very similar to the L_2 case and are shown

in Figure 39. With all particles featuring similar Jacobi Constants to the Lagrange points, all particles then achieve very similar Earth orbits after exiting the Lagrange points. Once again, no particles pass within geosynchronous altitude.

Table 10. Status of Particles at End of Simulation: L_1, Gateway Run 1

Status at Simulation End	Count	Percentage
Escaped the Earth-Moon System	49	1.60%
Impacted the Moon	190	6.22%
Impacted the Earth	0	0%
In the Lunar Sphere of Influence	794	25.98%
In the Earth Sphere of Influence	2023	66.20%

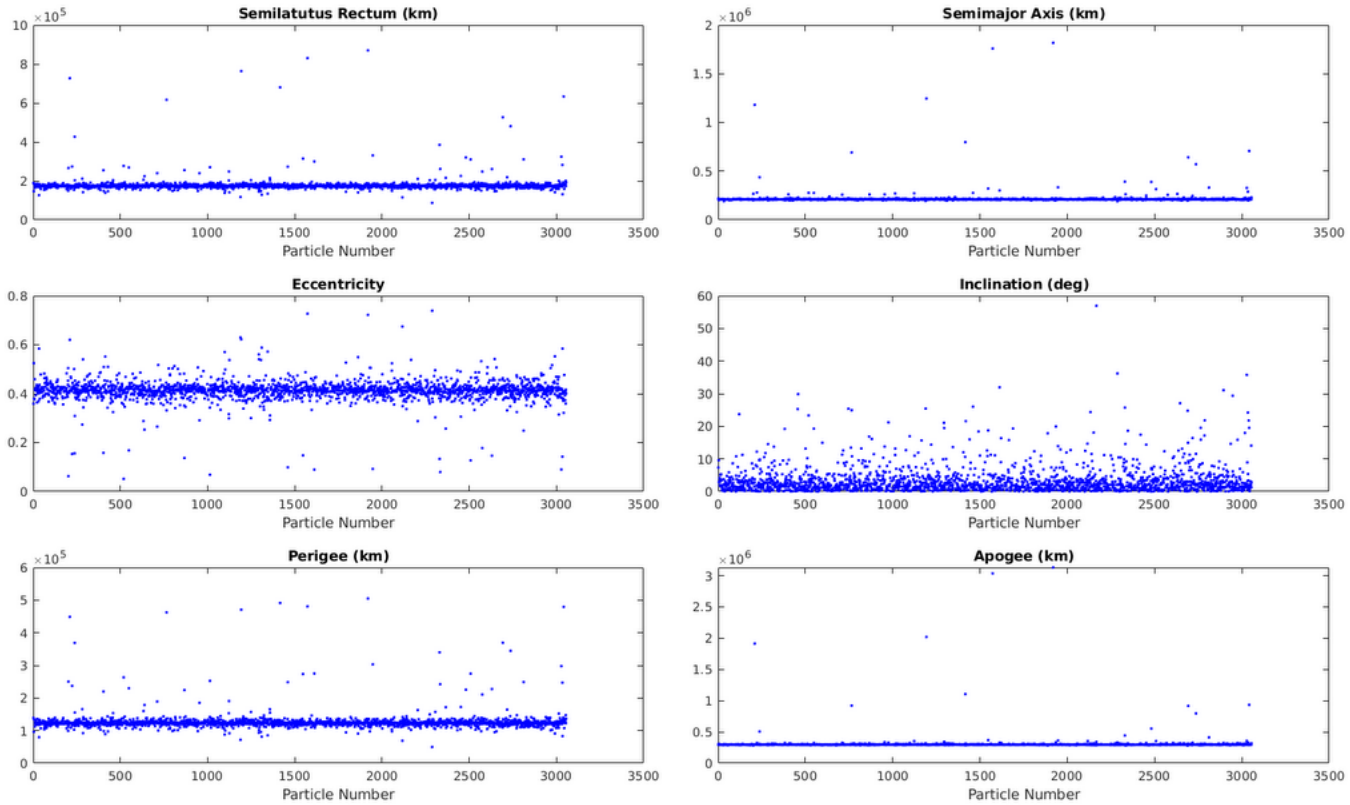

Figure 39. Orbital Elements of Earth-Orbiting Particles: Mishap at L_1, Gateway Run 1

The number of particles that pass within the Gateway's danger zone, the average speed of those particles relative to the Gateway, and the average mass of those particles is plotted throughout the simulation in Figure 40. The probability of hazard calculated throughout the simulation is shown in Figure 41. The probability of hazard for the Gateway is again very low; however, the probability of hazard is higher than when the mishap occurred at L_2. This is due to the particles that remain in lunar orbit and threaten the Gateway each time it passes through its periapsis. Particles also passed significantly closer to the Gateway, and the closest approach to the Gateway was 480 km.

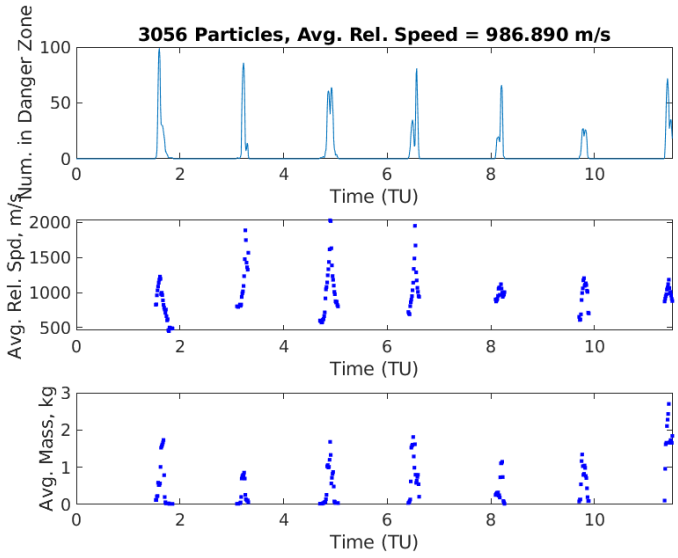

Figure 40. Statistics for Particles in Danger Zone: Mishap at L_1, Gateway Run 1

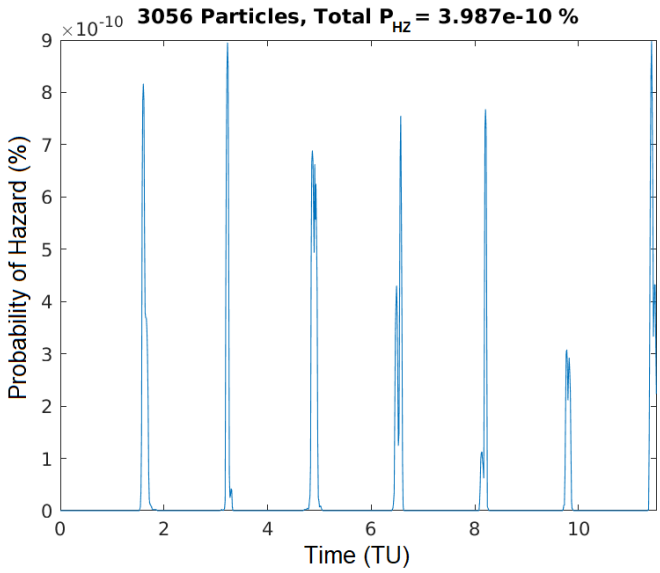

Figure 41. Probability of Hazard for the Gateway: Mishap at L_1, Gateway Run 1

Gateway Runs 2-4

The Gateway remaining runs for the catastrophic mishap at L_1, with the Gateway starting positions shown in Figure 27, are shown in Table 11. Unlike the L_2 case, Run 1 at L_1 results in the highest probability of hazard for the Gateway. This is due to the large number of objects that remain near the Moon. Since the primary threats to the Gateway come from these objects, and not from the debris streaming through the unstable manifold, the total probability of hazard is greatest for runs where the spacecraft is near the Moon for a larger portion of the 50-day simulation.

Table 11. Results for L_2, Gateway Runs 1-4

Run	Closest Approach to Gateway	Total P_{HZ}
1	480 km	3.987e-10 %
2	451 km	3.717e-10 %
3	808 km	2.728e-10 %
4	480 km	1.701e-10 %

Spacecraft at L_2

Some particles intersect the L_2 point when a spacecraft catastrophic mishap occurs at L_1, suggesting potential risks to spacecraft operating there. For the next simulation, a spacecraft was assumed to be fixed at L_2 while the catastrophic spacecraft mishap occurs at L_1. For this debris case, the statistics for particles that enter the danger zone are shown in Figure 42, and the probability of hazard is shown in Figure 43. As these figures show, the risk to a spacecraft at L_2 from an explosion at L_1 is very low, and far lower than the risk of the reverse scenario discussed previously. This is because fewer particles have reached the L_2 point by 50 days following the explosion when an explosion occurs at L_1. Even for longer simulations, the risk would likely stay low since particles should still cross L_2 gradually. The closest approach by a particle to the spacecraft is 1,655 km.

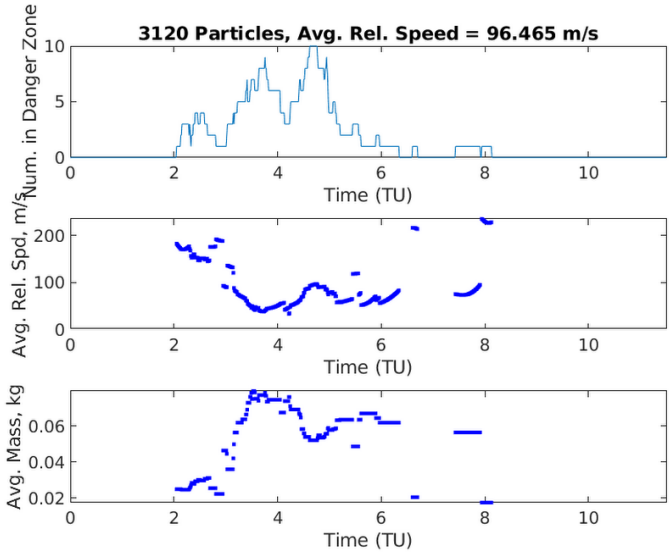

Figure 42. Statistics for Particles in Danger Zone: Mishap at L_1, Spacecraft at L_2

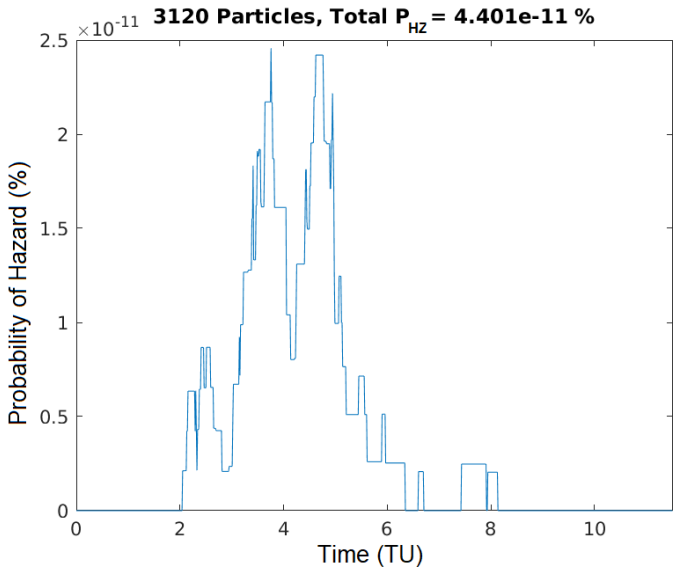

Figure 43. Probability of Hazard: Mishap at L_1, Spacecraft at L_2

Spacecraft in Earth-Moon Transfer

Finally, the Earth-Moon transfer simulation was repeated, but for an explosion at L_1. Since particles fill the manifolds more quickly when the explosion occurs at L_1, the simulation was started at -12.5 TU for this case, or 12.5 TU before the transfer spacecraft enters the stable manifold. The spacecraft again enters the stable manifold at 0 TU. The statistics for particles that enter the spacecraft's danger zone are shown in Figure 44, and the probability of hazard is shown in Figure 45. Due to the larger number of particles that enter the manifolds when the catastrophic mishap occurs at L_1, the risk to a spacecraft is about 23 times higher in this case when compared to the transfer case where the mishap occurs at L_2. The closest approach by a particle to the spacecraft is 620 km.

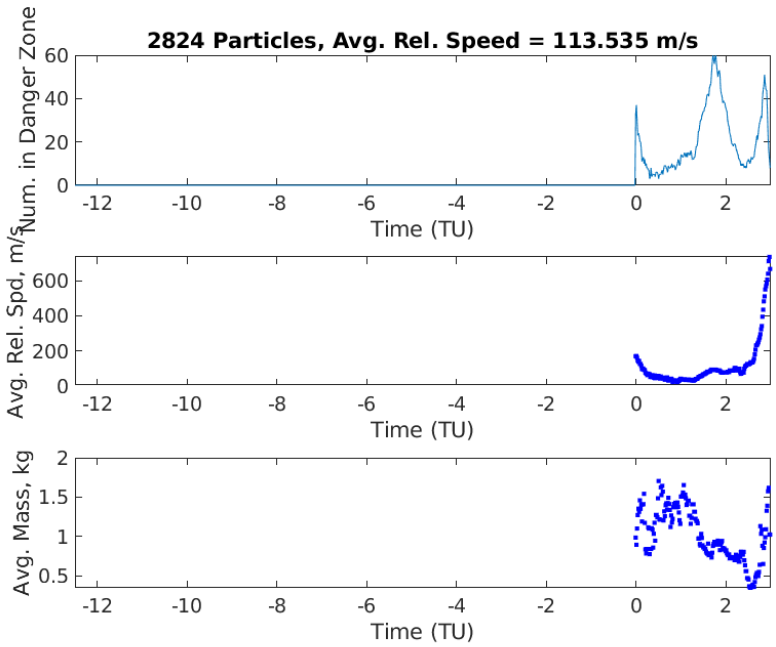

Figure 44. Statistics for Particles in Danger Zone: Mishap at L_1, Spacecraft Transferring

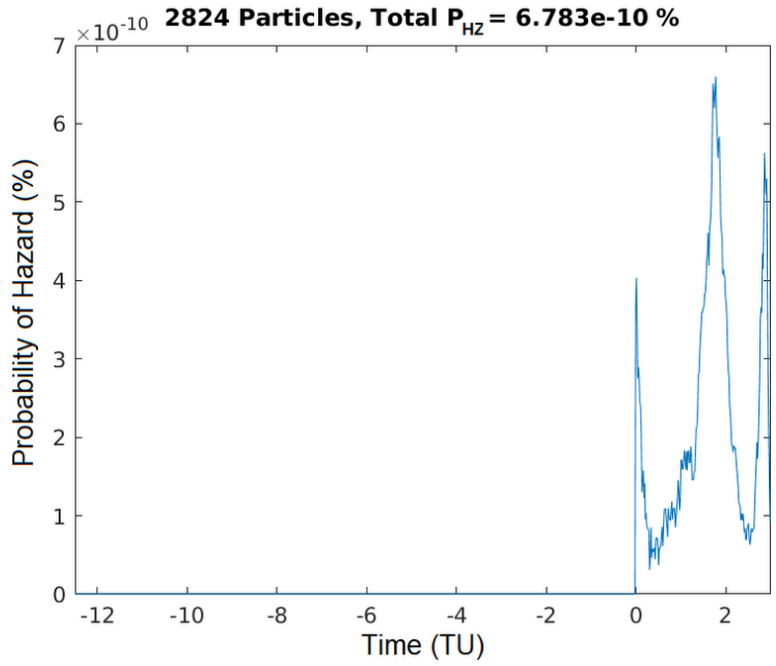

Figure 45. Probability of Hazard: Mishap at L_1, Spacecraft Transferring

5.2.6. Conclusions

Overall, the risks to other cislunar spacecraft from a catastrophic spacecraft mishap at L_1 or L_2 are very low. This is due to the vast distances enclosed in cislunar space. However, the risk is still measurable, and generally higher risks in the 50-day period following the explosion were found when a mishap occurs at L_1. Less debris moves beyond the Earth-Moon system, and instead accumulates in the Earth-Moon manifolds and Lunar orbit. This could be problematic for spacecraft that utilize the Earth-Moon manifolds for transfers, and for the Gateway, which could be threatened each orbit by debris near the Moon. A mishap at L_2 also resulted in relatively high risks to a spacecraft at L_1 due to the debris that crosses this point as it travels on the manifolds.

The risks to the Gateway are of particular concern since this spacecraft will be manned. The closest approach by a particle to the Gateway was 1,095 km for a mishap at L_2 and 480 km for a mishap at L_1. Existing NASA guidelines for the International Space Station classify debris that enters a box 1.5 km deep, 50 km wide, and 50 km long with the spacecraft in the center as potentially requiring an avoidance maneuver [81], so using this guidance, no maneuver would be required by the Gateway. However, tracking difficulties in cislunar space could increase the required safe distance from the Gateway. This fact could make a debris event at L_1 or L_2 problematic for the Gateway, even though the risk is low.

5.3. Case Study: Mishap During an Apollo-like Transfer

5.3.1. Motivation

One spacecraft mishap has already occurred in cislunar space, namely the explosion of the oxygen tank onboard the Apollo 13 spacecraft during its transfer to the Moon. This explosion generated so many fragments that the swarm of debris surrounding the spacecraft made navigation by the stars impossible, forcing mission control to instead rely on navigation using the sun [82]. The debris field could also be imaged from the ground, and images following the explosion show a debris cloud extending about 60 km from the spacecraft [83]. Following the explosion, the debris likely moved back towards Earth, possibly intersecting lower Earth orbits at very high relative velocities. A similar debris event today could potentially threaten spacecraft in the crowded Low Earth Orbit (LEO) and Geostationary (GEO) environments if the debris intersects those orbits. Therefore, this case study involves the analysis of a catastrophic spacecraft mishap during a transfer to the Moon much like the Apollo 13 scenario.

5.3.2. Initial Conditions

The Apollo spacecraft utilized a three-day transfer to reach the Moon. This transfer is slightly less efficient than a standard Hohmann transfer, but shortens the mission by about 1.5 days, requiring less consumables for the humans on board. The Apollo missions began with a parking orbit in LEO, followed by a Trans-Lunar Injection (TLI) burn that placed the spacecraft on a free-return trajectory. The free-return trajectory enables a return to Earth in the event of a problem. As the Moon approached, a series of small mid-course correction burns were conducted to lower the spacecraft's perilune. Finally, a Lunar Orbit Insertion (LOI) burn was conducted at perilune to bring the spacecraft to a parking orbit around the

Moon. Following the completion of the lunar landing mission, a Trans-Earth Injection (TEI) burn was conducted to bring the spacecraft back to Earth, where it splashed down in the Pacific Ocean [84]. The approximation of the Apollo trajectory used for the simulations is shown in the rotating Earth-Moon reference frame in Figure 46. The blue circles mark the locations of the simulated catastrophic mishap for each run of the simulation and the red dots mark the locations of burns. Note that only one mid-course correction burn was modeled for simplicity, and the time spent in lunar orbit was not modeled.

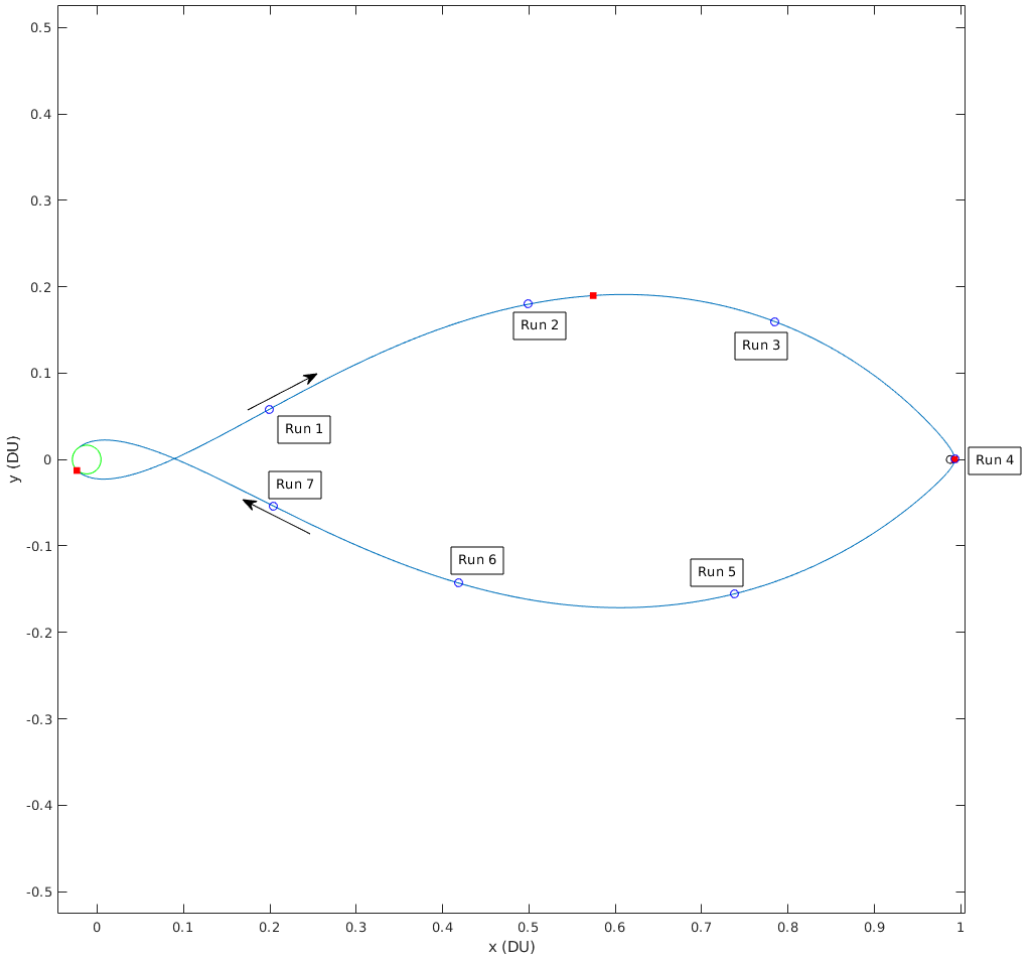

Figure 46. Apollo Trajectory Model in the Rotating Earth-Moon Reference Frame

5.3.3. Simulation Results

For each run location along the Apollo-like transfer, particles were simulated from the time of the catastrophic spacecraft mishap to $t = 50$ days. There was no notional spacecraft for this case, and the survivability model was not applied. Instead, the risks to spacecraft near Earth are evaluated based on the number of particles that have a perigee that is within GEO altitude at the end of the simulation. The number of particles that have a perigee within GEO altitude for each run of the simulation are shown in Table 12. The locations of all particles in the Earth-Moon system at the end of the simulation are shown in Table 13. Note that Run 3 is most like the Apollo 13 mishap, since the Apollo 13 incident took place about two days into the mission, following the maneuver to exit the free-return trajectory [82].

Table 12. Number of Particles with Perigee within GEO Altitude, Apollo Transfer Simulations

Run Locations	Run	Mishap Time (Days)	Number of Particles with Final Perigee within GEO Altitude
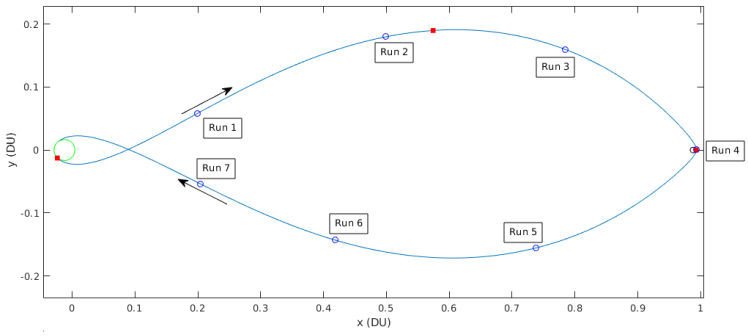	1	0.25	655
	2	1.00	657
	3	2.00	566
	4	2.97	657
	5	4.00	630
	6	5.00	364
	7	5.49	156

Table 13. Status of Particles at Simulation End, Apollo Transfer Simulations

Run Number	Escaped Earth-Moon System	Impacted Moon	Impacted Earth	End in Lunar Sphere of Influence	End in Earth Sphere of Influence
1	9.62%	5.27%	25.89%	0%	59.21%
2	8.22%	6.72%	23.21%	0%	61.85%
3	6.14%	16.43%	15.46%	0%	61.97%
4	5.36%	0.66%	41.43%	0%	52.26%
5	1.68%	0%	73.49%	0%	24.80%
6	2.67%	0%	82.98%	0%	14.25%
7	5.94%	0%	87.73%	0%	6.25%

Snapshots of the simulation during selected runs are shown in Figure 47. In these snapshots, the green circle marks the location of the Earth, the black circle marks the location of the Moon, the red crosses mark the locations of the Lagrange points, the yellow line indicates the current direction to the Sun, and the black dots represent debris particles.

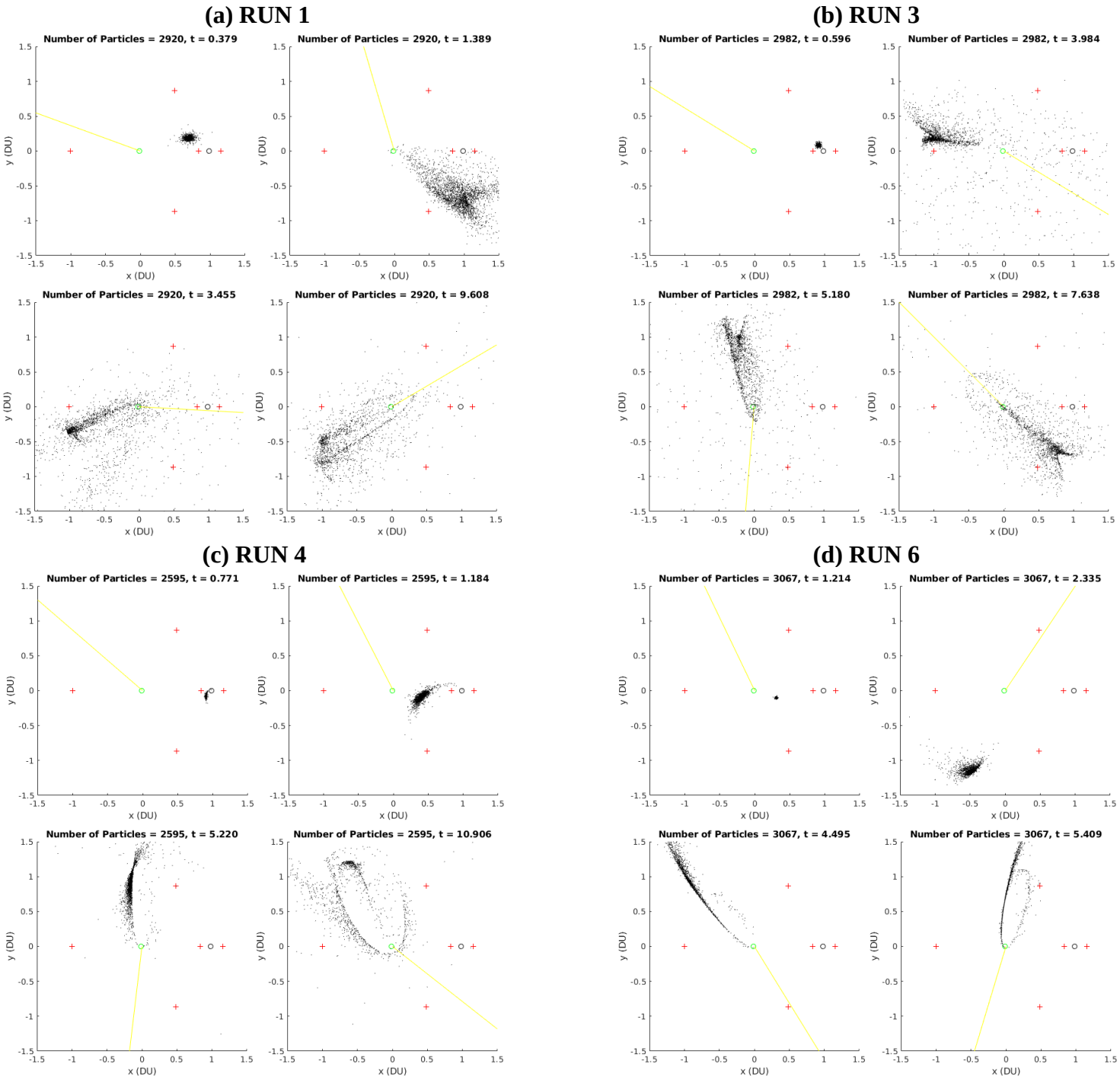

Figure 47. Snapshots of Selected Runs, Apollo Transfer Simulations: (a) Run 1; (b) Run 3; (c) Run 4; (d) Run 6

In Run 1 (shown in Figure 47(a)), Run 2, and Run 3 (shown in Figure 47(b)), most of the debris particles are thrown out of the Earth-Moon plane after passing the Moon and begin orbiting at an angle of approximately 90º relative to the Earth-Moon line. In addition, a cardioid-like shape forms at apogee as particles on the outer edges of the particle cloud orbit are farther from the Earth. This shape is especially apparent in Run 3 in Figure 47(b), and may be due to the effects of the Moon on the particle cloud as the particle cloud passes the Moon. Because the orbits for Runs 1 and 2 prior to the explosion started in a LEO parking orbit, many particles return to within GEO when they reach their perigee following the explosion. These particles would likely continue to intersect lower Earth orbits at each perigee passage for a very long time following the explosion due to the high apogee height, which would make it difficult for atmospheric drag to decay the orbits of the particles enough for the particles to re-enter the Earth's atmosphere. This could cause long-term debris threats to Earth-orbiting spacecraft.

In Run 3, shown in Figure 47(b), the catastrophic mishap occurs at a similar location along the spacecraft's trajectory as the Apollo 13 disaster. Run 3 is also the first run that takes place following the course-correction maneuver that lowers the spacecraft's perilune. As expected, this causes many more particles to impact the Moon. Overall, the results are very similar to Runs 1 and 2 due to the small ΔV in the course-correction maneuver. The particles enter an orbit that is at an angle of approximately 90º from the Earth-Moon line and many have a perigee within GEO altitude. This may provide an indication of the motion of the debris from the Apollo 13 incident in the 50 days following the explosion and suggest risks to spacecraft near Earth if a similar event occurred today.

The spacecraft mishap in Run 4, shown in Figure 47(c), occurs at perilune, resulting in different behavior from the previous three runs. After passing the Earth for the first time, the particles enter a highly elliptical orbit with an apogee well beyond the Moon. Unlike the previous runs, the motion is mostly in the Earth-Moon plane. However, after passing the Moon again, many of the particles enter an orbit at an angle of about 90º to the Earth-Moon line, like the previous runs. Another particle cloud that has an apogee well beyond the Moon also forms. This behavior is shown in the bottom right corner of Figure 47(c). Particles in each of the two main particle cloud orbits still pass close to the Earth, potentially creating long-term threats to Earth-orbiting spacecraft.

Significantly more particles impact the Earth in Runs 5-7 because the spacecraft is on a trajectory that would bring it into the Earth's atmosphere prior to the explosion. The debris particles that avoid the Earth's atmosphere then travel well beyond the Moon's distance before returning to a perigee close to Earth. Particles in these runs would intersect the LEO environment at each perigee passage. However, the threat would diminish within about 50 days as particles return to Earth. Progressively fewer particles survive each perigee passage as more and more particles enter the Earth's atmosphere. The thinning of the particle cloud as the particles enter the atmosphere is shown for Run 6 in the bottom right corner of Figure 47(d). Note that atmospheric drag was not modeled in this simulation, and particles are terminated when they pass within 80 km of the Earth.

5.3.4. Conclusion

Of the case studies examined in this research, a catastrophic spacecraft mishap during an Apollo-like transfer results in the greatest risk to spacecraft near Earth, with hundreds of debris particles coming within geosynchronous altitude at high relative velocities during each perigee passage. The particles would likely remain in space for a very long time (much longer than the 50-day simulation) due to their very high apogees that would decay slowly due to atmospheric drag. Therefore, this type debris event may be the most concerning of the case studies due to the potential for long-term risks to crowded orbits near Earth.

5.4. Case Study: Mishap in the L_1 Manifold

5.4.1. Motivation

The next case study involves a catastrophic spacecraft mishap during a transfer to the Moon using a low-energy trajectory. Trajectories that utilize three-body dynamics are an ongoing topic of research and can enable transfers between Earth orbits and the Moon or the Lagrange points for less fuel than conventional direct transfers. These types of transfers are discussed in detail by Parker and Anderson [18]. The Gravitational Recovery and Interior Laboratory (GRAIL) mission, launched in 2011, was the first spacecraft to utilize a low-energy transfer to reach the Moon [18]. These types of trajectories are expected to become more common due to their fuel savings as lunar exploration increases, increasing the need to understand the motion of debris following a catastrophic spacecraft mishap that occurs while a spacecraft is utilizing these techniques. The stable nature of these trajectories, and their great distance from Earth that negates the effect of atmospheric drag, could lead to long-term debris threats in cislunar space.

5.4.2. Initial Conditions

To simulate the pre-explosion trajectory of a spacecraft that transfers between the Earth and the Moon along the L_1 stable manifold, the direct transfer method to L_1 described by Parker and Anderson [18] was used as a guide. This method was already used to generate the trajectory of a transferring spacecraft in Section 5.2.3, and the same method is applied again. The trajectory of the spacecraft that suffers the catastrophic mishap begins with the spacecraft on the stable manifold at the stable manifold's lowest y-position and ends after the spacecraft has passed L_1 and returned the vicinity of Earth as shown in Figure 48. The blue circles mark the locations of the simulated catastrophic mishap for each simulation run. Note that a small maneuver at or before reaching L_1 would enable a spacecraft that follows this trajectory to continue through the L_1 point towards the Moon.

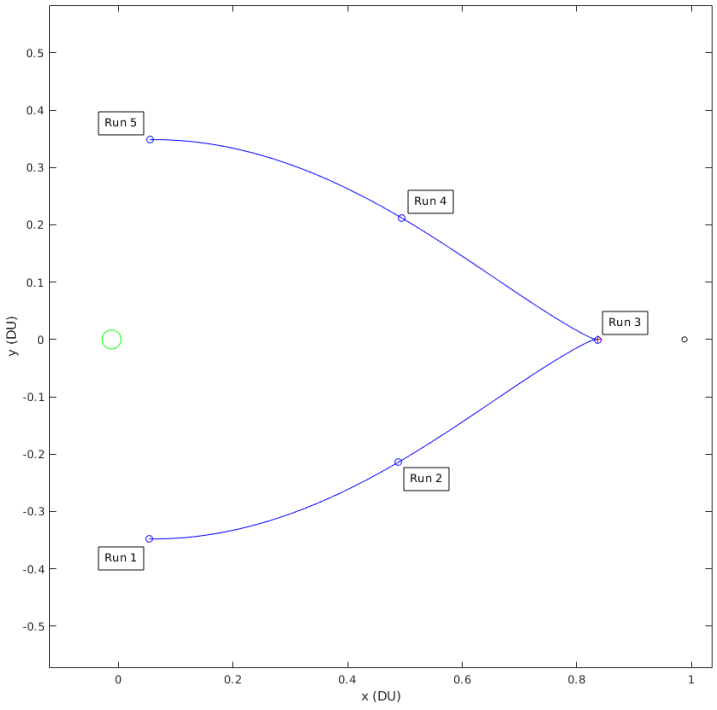

Figure 48. Trajectory for Spacecraft Transferring along the L_1 Manifolds in the Rotating Reference Frame

5.4.3. Simulation Results

The simulations for a spacecraft transferring along the L_1 manifold apply the spacecraft survivability model to analyze the threats to a notional spacecraft operating at the L_1 point. The simulations prior to the L_1 point start at negative time because the trajectory that brings a spacecraft towards L_1 was obtained by propagating the trajectory backwards in time. The simulation begins at the time of the catastrophic spacecraft mishap and continues to $t = 50$ days. Five runs were conducted for catastrophic mishaps at different locations along the L_1 manifold. The survivability results for each run are shown in Table 14. The final locations of all particles at the end of the simulation are given in Table 15. No particles end within GEO altitude, and the primary threats for a catastrophic mishap in the manifolds are to a spacecraft at L_1 and perhaps to future spacecraft that utilize the L_1 manifold. However, as the very low probability of hazards indicate, the threat to any one spacecraft is very low due to the vast distances in cislunar space.

Table 14. Survivability Results for a Spacecraft at L_1, Manifold Transfer Simulations

Run Locations	Run Number	Mishap Time (Days)	Closest Approach to Notional Spacecraft at L_1	Mean Relative Speed	Total P_{HZ}
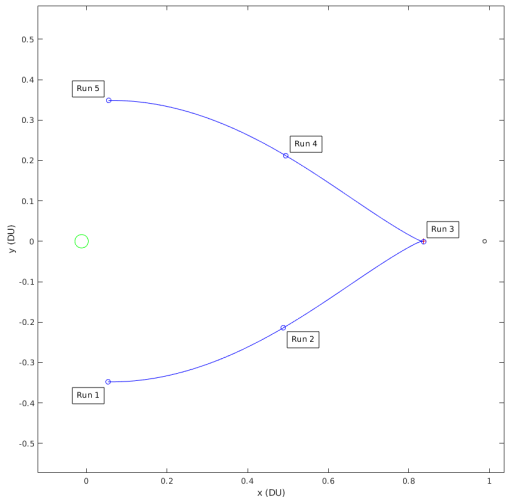	1	-13.04	186 km	140 m/s	2.676e-9 %
	2	-11.43	233 km	118 m/s	3.872e-9 %
	3	0	52 km	75 m/s	1.806e-8 %
	4	11.94	736 km	376 m/s	4.668e-12 %
	5	13.59	832 km	480 m/s	4.731e-12 %

Table 15. Status of Particles at Simulation End, Manifold Transfer Simulations

Run Number	Escaped Earth-Moon System	Impacted Moon	Impacted Earth	End in Lunar Sphere of Influence	End in Earth Sphere of Influence
1	16.94%	3.77%	0%	2.13%	77.16%
2	20.76%	4.33%	0%	2.73%	72.18%
3	1.99%	5.19%	0%	20.73%	72.08%
4	0.80%	0.30%	0%	0.27%	98.63%
5	1.21%	1.37%	0%	0%	97.42%

Snapshots of selected simulation runs are shown in Figure 49. In all runs, the debris particle cloud stretches to fill the L_1 manifolds (which were shown in Figure 28). For runs that occur prior to the L_1 point, particles with large enough energy levels can cross the L_1 point and continue towards the Moon, while the remaining particles travel along the unstable manifold back towards Earth. The particles that continue towards the Moon could suggest possible hazards to lunar orbiting spacecraft since many of the particles can remain near the Moon for at least 50 days. The particles that continue back towards Earth could also create some risk because they can remain in the manifold long enough to eventually

return to the L_1 point. This occurs for particles in Runs 4 and 5, which started after L_1, as the non-zero P_{HZ} in Table 14 indicates. The particles that return to L_1 do so at much greater velocities, likely due to perturbations that have increased the particle velocity relative to L_1. Overall, a mishap at any location along the L_1 manifold could create small but measurable threats to a spacecraft operating at L_1, a spacecraft traveling through the L_1 manifold, or a spacecraft operating in a distant lunar orbit.

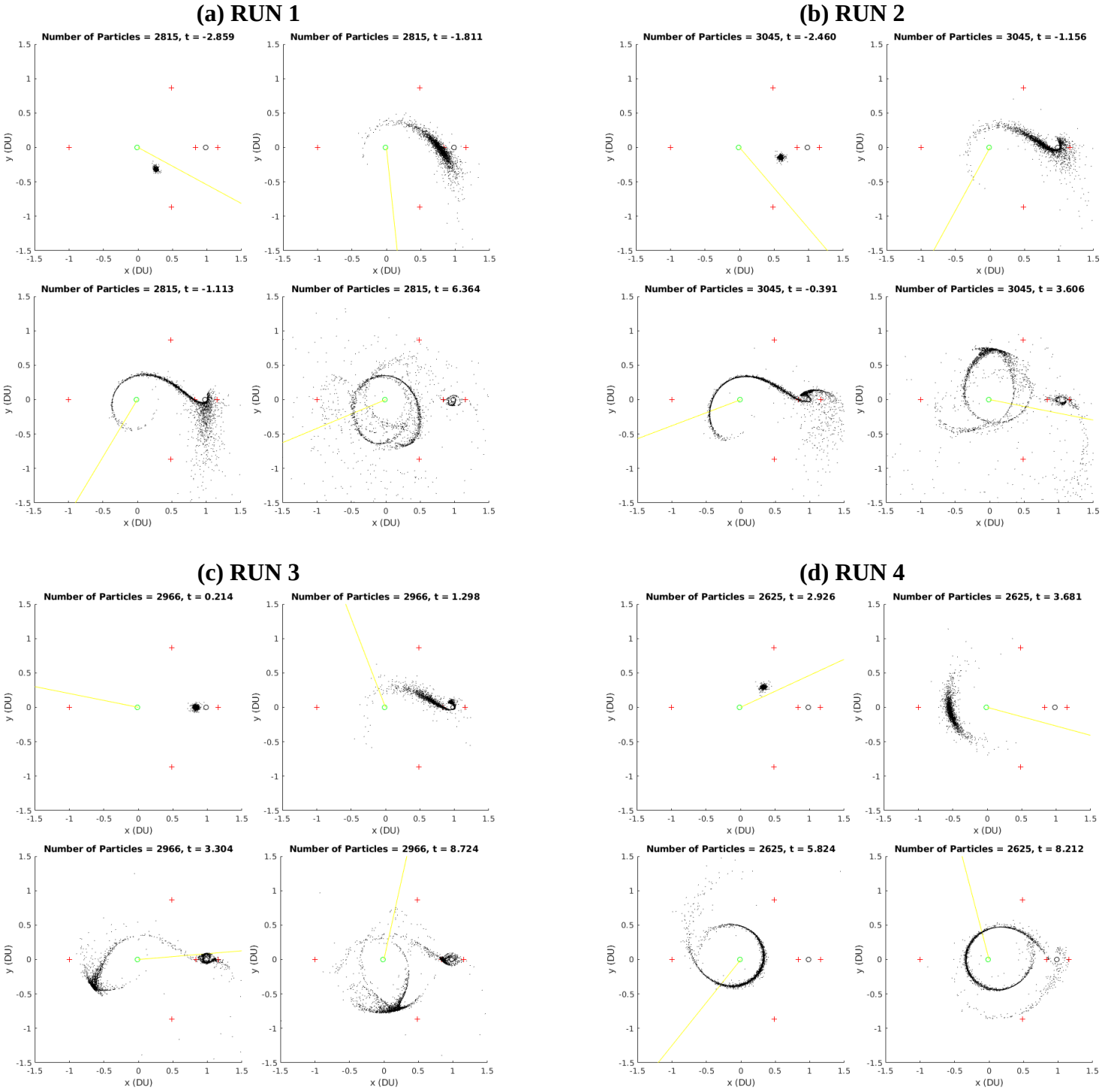

Figure 49. Snapshots of Selected Runs, Manifold Transfer Simulations: (a) Run 1; (b) Run 2; (c) Run 3; (d) Run 4

5.4.4. Conclusion

Catastrophic spacecraft mishaps in the L_1 manifold would pose little threat to spacecraft closer to Earth, but they could pose some risk to future spacecraft that utilize the unique dynamics of cislunar spacecraft for mission operations. The L_1 manifold can enable transfers to the lunar region for less fuel than a conventional Hohmann transfer, and the L_1 point could be an appealing location for future spacecraft due to its high vantage point over the Earth and lower orbital altitudes. Debris would circulate through these regions indefinitely if a mishap occurred in the L_1 manifold. In addition, some debris could threaten spacecraft in lunar orbits. However, the risk to any particular spacecraft would be extremely low due to the vast distances in cislunar space.

5.5. Case Study: Mishap at the Stable Earth-Moon Lagrange Points

5.5.1. Motivation

In this case study, the study of debris near L_4 and L_5 conducted in Chapter IV was modified so that the source of the debris is natural instead of artificial. The study of the Kordylewski clouds in Chapter IV demonstrated that natural debris can remain at the stable Lagrange points for long periods of time, suggesting that artificial debris from a catastrophic spacecraft mishap could also accumulate at these points. This could become problematic if the L_4 and L_5 points become more crowded with spacecraft in the future. Therefore, this case study simulates catastrophic spacecraft mishaps at L_4 and L_5 and analyzes the resulting threats to spacecraft operating at L_4 and L_5, respectively.

5.5.2. Initial Conditions

The spacecraft that suffer the catastrophic mishaps are assumed to be fixed at the L_4 or L_5 points prior to the explosions. Since the spacecraft remain fixed, the BCR4BP trajectory model was not used to generate the trajectory of the spacecraft. One run of the simulation was conducted for a spacecraft mishap at L_4 and one run was conducted for a spacecraft mishap at L_5.

5.5.3. Simulation Results

The simulation for a catastrophic spacecraft mishap at L_4 applies the survivability model to a different notional spacecraft also operating at L_4, while the simulation for a catastrophic spacecraft mishap at L_5 applies the survivability model to a notional spacecraft operating at L_5. Both simulations start with the catastrophic mishap at $t = 0$ and continue for 365 days. The survivability results for the runs at L_4 and L_5 are shown in Table 16. The total P_{HZ} is higher for these cases than any of the previously discussed L_1 manifold cases due to the stability of L_4 and L_5. As shown in Table 17, about a third of the particles remain within a 200,000-radius of the Lagrange point after a year for the runs at L_4 and L_5. This creates a continuous hazard to the notional spacecraft, although the risk remains low due to the vast distances in cislunar space.

Table 16. Survivability Results for Spacecraft at L_4/L_5, Stable Lagrange Point Simulations

Run	Mishap Time (Days)	Closest Approach to Notional Spacecraft	Mean Relative Speed	Total P_{HZ}
L_4	0	270 km	38 m/s	6.377e-8
L_5	0	462 km	40 m/s	4.314e-8

Table 17. Status of Particles at Simulation End, Stable Lagrange Point Simulations

Run	Escaped Earth-Moon System	Impacted Moon	Impacted Earth	End in Lunar Sphere of Influence	End Within 200,000 km of L_4/L_5	End Elsewhere in Earth Sphere of Influence
L_4	27.03%	5.90%	0%	0.50%	33.80%	32.76%
L_5	34.44%	4.09%	0%	0.17%	29.81%	31.49%

Figure 50 shows snapshots of the L_4 and L_5 simulations runs, and the debris particles move similarly for each case. The particles initially expand rapidly due to the explosion, then many begin to fall back towards their respective Lagrange point. The particles that do not escape are initially confined to an area roughly equivalent to the ZVCs associated with the Jacobi Constants of the L_4 and L_5 points. These ZVCs were shown in the bottom right corner of Figure 6, and look similar to the particle distributions shown in the upper right corners of Figure 50(a) and Figure 50(b). As solar perturbations act on the particles, the particles begin to expand and contract about L_4 and L_5 on a regular cycle, like what was noted in the study of the Kordylewski clouds by Slíz-Balogh, Barta, and Horváth [8]. The particles spin about the Lagrange point in the rotating frame with pinwheel-like arms that periodically collapse and expand. The velocities of the trapped particles that pass within the 10,000 km danger zone of the notional spacecraft relative to the spacecraft also vary according to a regular cycle between about 20 and 70 m/s. This cyclical pattern matches the cycle in the masses of particles within the danger zone, with lighter particles, which are given more ΔV from the explosion, tending to enter the danger zone with higher speeds relative to the notional spacecraft.

Over time, particles are ejected from L_4 and L_5 due to the destabilizing effect of solar gravity, but nearly 1,000 particles remain trapped at the end of the year-long simulation in each case. In a real-world mission, the significant number of particles that remain near these points may increase the need for spacecraft operators to monitor the area around the notional spacecraft for debris. Difficulties tracking debris at such great distances from Earth may make it more likely that the spacecraft will have to maneuver to avoid debris, despite the low debris density relative to orbital environments closer to Earth.

(a) Mishap at L_4 **(b) Mishap at L_5**

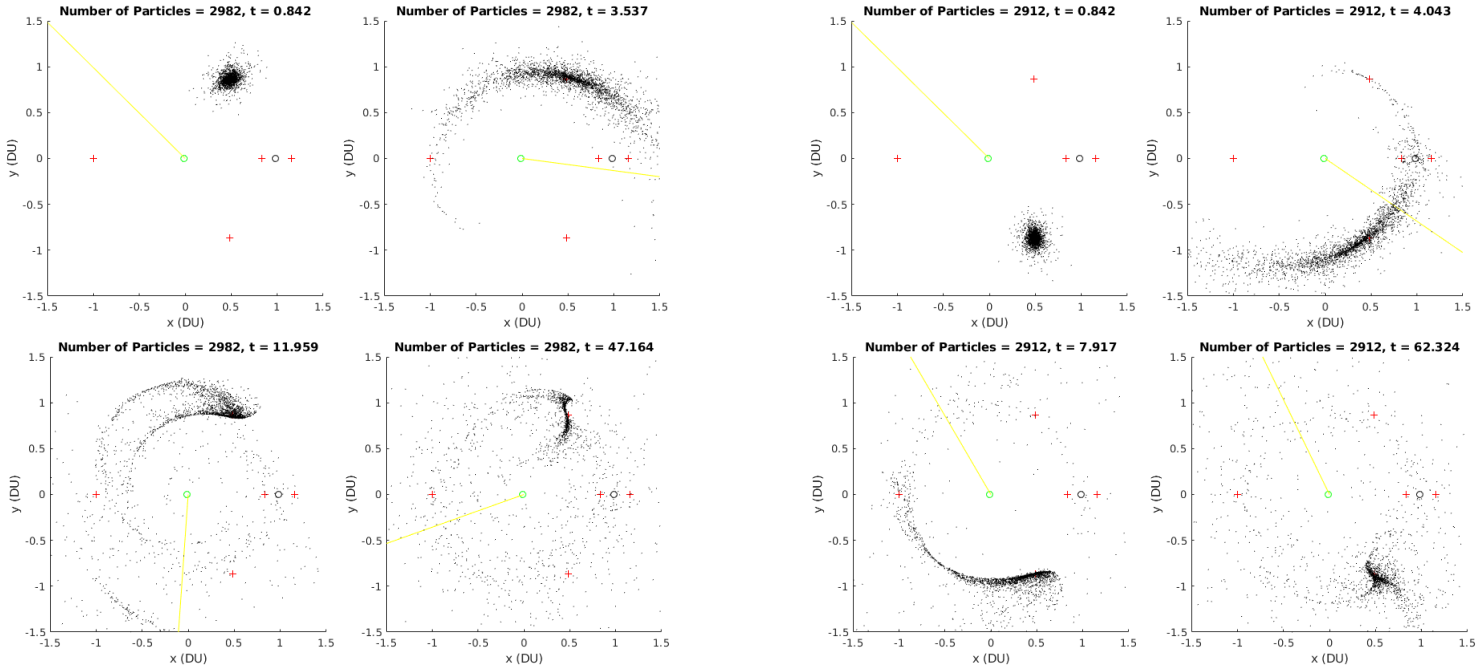

Figure 50. Snapshots of Selected Runs, Stable Lagrange Point Simulations: (a) Mishap at L_4; (b) Mishap at L_5

5.5.4. Conclusion

This case study demonstrated that catastrophic spacecraft mishaps at L_4 and L_5 would pose some risks to other spacecraft operating at those points. L_4 and L_5 could be an appealing location for future spacecraft due to their stability, but much of the debris from a catastrophic spacecraft mishap at either point would be also stable at those points for at least a year following the explosion. This results in a much higher probability of hazard to the notional spacecraft than any prior simulation runs. Debris circulating these points would also likely be difficult to track from Earth due to the great distance, making it difficult to maneuver a spacecraft to avoid debris. However, like the other case studies, the risk is still low, and debris would only become problematic if these points become more crowded in the future or if repeated mishaps occur.

5.6. Case Study: Mishap in Lunar Orbit

5.6.1. Motivation

The final artificial debris case study analyzes threats from debris following a catastrophic spacecraft mishap in lunar orbit. Greater numbers of spacecraft may begin to operate in lunar orbit to support lunar exploration and colonization in the coming years, increasing the need to study the risks resulting from a catastrophic spacecraft mishap. An improved understanding of the risks from artificial debris in lunar orbit enables an understanding of the possible importance of proper debris management techniques in the lunar environment. Depending on the risks from artificial debris in lunar orbit, disposal strategies like those used at end-of-life for Earth-orbiting spacecraft may be necessary for spacecraft orbiting the Moon.

5.6.2. Initial Conditions

For the debris simulation, the spacecraft that suffers the catastrophic mishap in lunar orbit is initially located in a 110 km circular orbit around the Moon, which was the lunar parking orbit utilized in the Apollo 11 mission [84]. The catastrophic mishap was simulated for the four different catastrophic mishap locations shown in Figure 51.

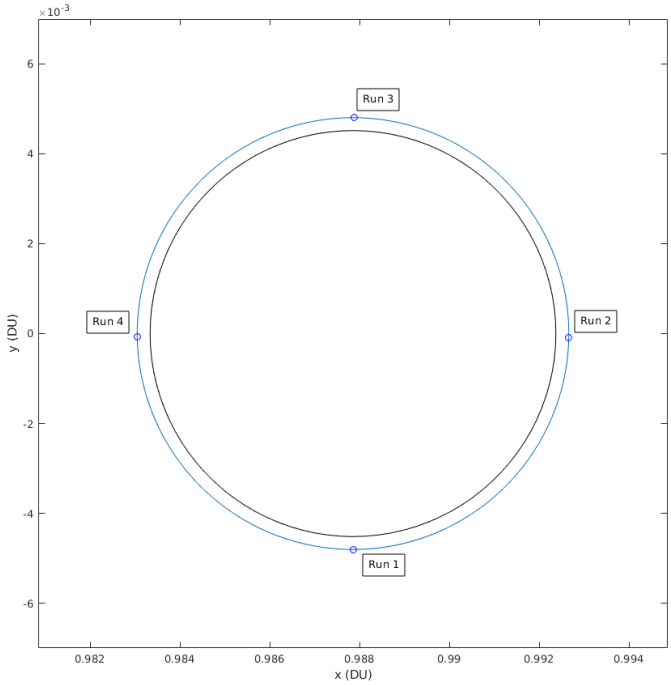

Figure 51. Lunar Orbit Trajectory for Spacecraft Suffering Catastrophic Mishap, with Locations of Mishap Marked

Debris risks were analyzed for a notional spacecraft also located in a 110 km circular orbit around the Moon. This spacecraft is always located at the "Run 1" position shown in Figure 51 at the start of the simulation. This means that the notional spacecraft is at the same location as the spacecraft which suffers the catastrophic mishap in Run 1, and is 90º, 180º, and 270º behind the exploding spacecraft in Runs 2, 3, and 4, respectively. Due to the significantly smaller range of particle motion in the lunar region, the size of the notional spacecraft's danger zone is 10 km in this simulation, with a hazard zone radius of 500 m.

5.6.3. Simulation Results

The motion of debris following the catastrophic mishap was simulated for one day. Because the non-spherical nature of the lunar gravity field was not incorporated in this simulation, the trajectory simulation would not be accurate over longer time periods. The survivability results for the notional spacecraft in lunar orbit are shown in Table 18. These probabilities of hazard are far higher than any of the previously examined case studies, with a maximum risk of about 0.003% for Run 1, and risks of between 0.000185% and 0.000371% for Runs 2-4. These probabilities would likely create concern in a real-world mission, especially since they are for a simulation lasting only one day. The debris hazard would continue for far longer than the one-day simulation.

Table 18. Survivability Results for a Spacecraft in Lunar Orbit, Mishap in Lunar Orbit Simulations

Run Locations	Run Number	Mishap Time (Days)	Closest Approach to Notional Spacecraft	Mean Relative Speed	Total P_{HZ}
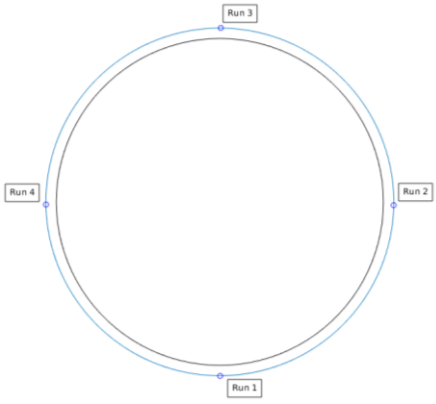	1	0	0.182 km	32 m/s	2.993e-3 %
	2	0	0.933 km	76 m/s	3.717e-4 %
	3	0	0.803 km	90 m/s	1.845e-4 %
	4	0	1.420 km	46 m/s	3.505e-4 %

Snapshots of all runs in the simulation are shown in Figure 52. The Moon is shown to-scale in these snapshots, and the green line represents the direction to the Earth. The motion was simulated in the rotating Earth-Moon reference frame, so the Earth is always located

in the negative x direction. The yellow line indicates the direction to the Sun relative to the Moon. The blue star represents the location of the notional spacecraft.

The motion of the debris particles is very similar across all runs. In all runs, the debris particles expand to form a particle cloud in the moments immediately following the catastrophic mishap. As the particles move farther around the Moon, the leading edge of the particle cloud bends towards the Moon, while the trailing edge of the cloud bends away from the Moon. The particle cloud is stretched into a thin line as it continues in its orbit. The leading edge of the cloud is at a lower altitude and circles the Moon more quickly than the trailing edge of the cloud, causing the leading edge to eventually overtake the trailing edge. This causes a spiral-like shape with bands of increased debris density. Similar behavior has also been noted in studies of debris-generating events in Earth orbits [85]. The debris cloud stretches to encircle the Moon several times, filling a range of lunar orbital altitudes with debris.

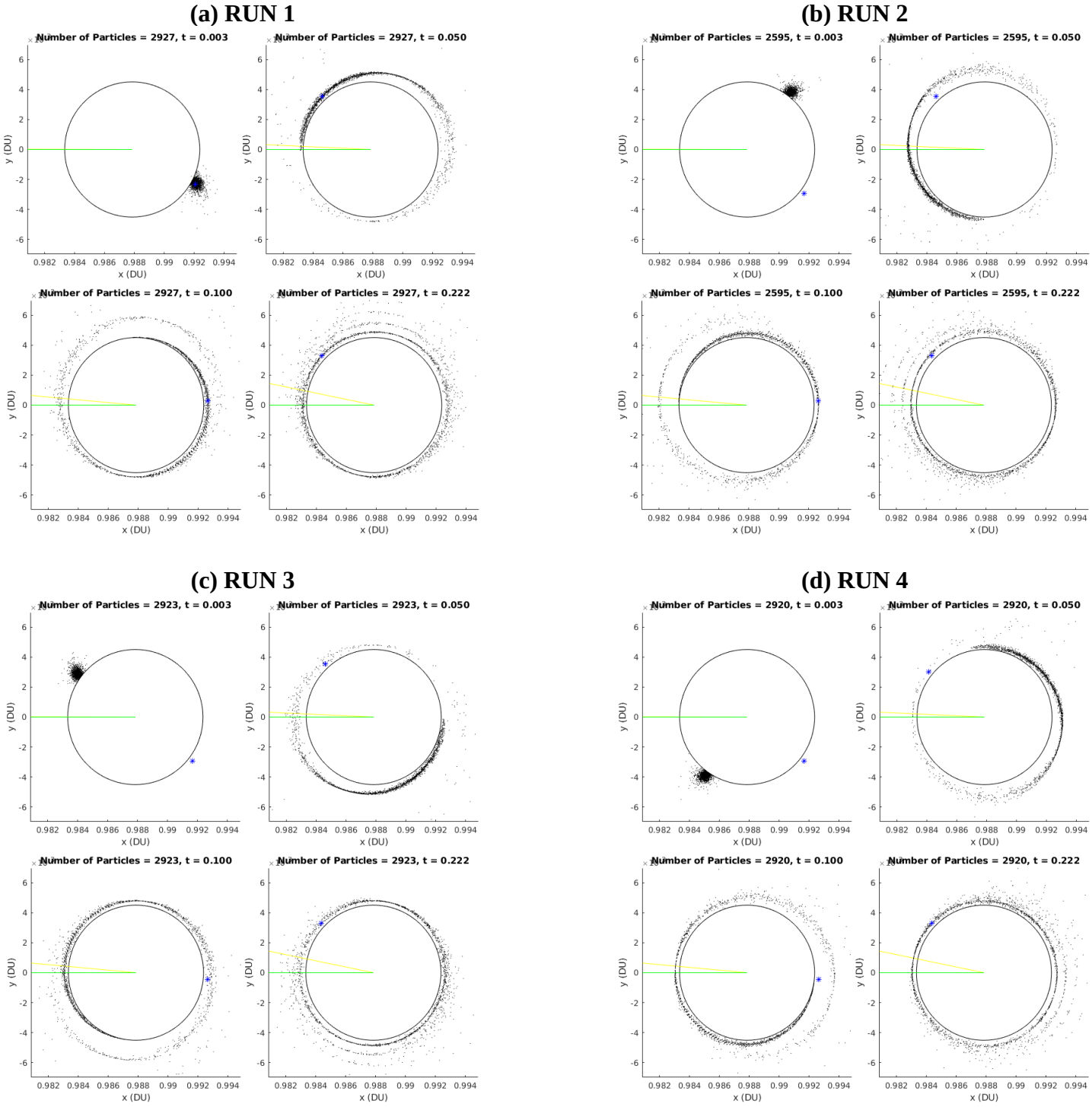

Figure 52. Snapshots of Mishap in Lunar Orbit Simulations: (a) Run 1; (b) Run 2; (c) Run 3; (d) Run 4

The status of particles at the end of the simulation is shown in Table 19. For all runs, about 30% of particles impacted the lunar surface. The particles that impact the Moon could be concerning due to the possible contamination of the lunar environment or potential threats to future lunar colonies, in particular, power generation and remote sensing infrastructure. A plot of the number of lunar impacts over time for Run 1 is shown in Figure 53. The number of impacts to the lunar surface reaches a peak about 15 minutes following the explosion, then declines slowly between 30 minutes and 1 hour following the explosion. All runs exhibited very similar trends in the number of impacts over time. A three-dimensional visualization of the locations of impacts for Run 1 on the lunar sphere for is shown in Figure 54. A ring of debris impacts forms below the former ground track of the spacecraft. The same behavior was present for all runs. Finally, Figure 55 provides polar plots of the number of lunar surface impacts by longitudinal location around the Moon, relative to the longitudinal location of the Run 1 catastrophic mishap. The angular location of the mishap is shown with a red dot on these plots. For each run, the region containing the most significant number of lunar impacts covers an angle of about 120º, or about a third of the way around the Moon.

Table 19. Status of Particles at Simulation End, Mishap in Lunar Orbit Simulations

Run Number	Escaped Earth-Moon System	Impacted Moon	Impacted Earth	End in Lunar Sphere of Influence	End in Earth Sphere of Influence
1	0%	28.80%	0%	71.19%	0%
2	0%	27.01%	0%	72.99%	0%
3	0%	28.67%	0%	71.33%	0%
4	0%	29.97%	0%	70.03%	0%

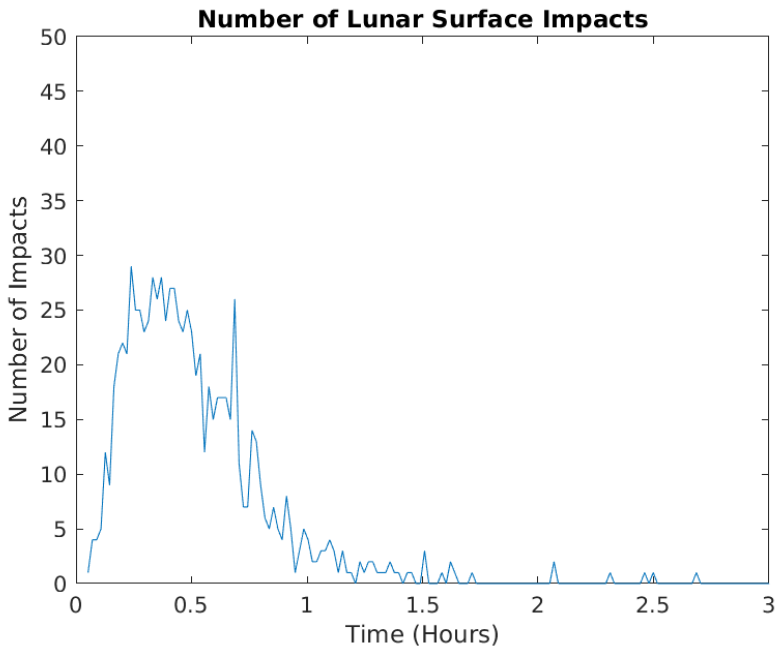

Figure 53. Time of Lunar Surface Impacts, Lunar Orbit Mishap Run 1

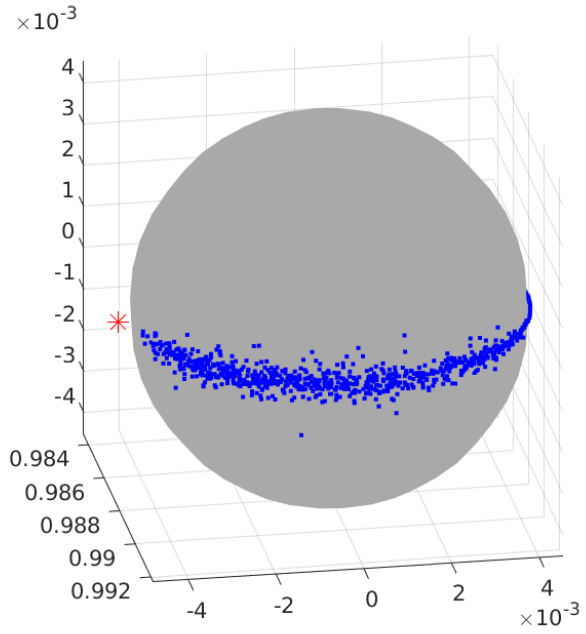

Figure 54. Location of Lunar Surface Impacts, Lunar Orbit Mishap Run 1

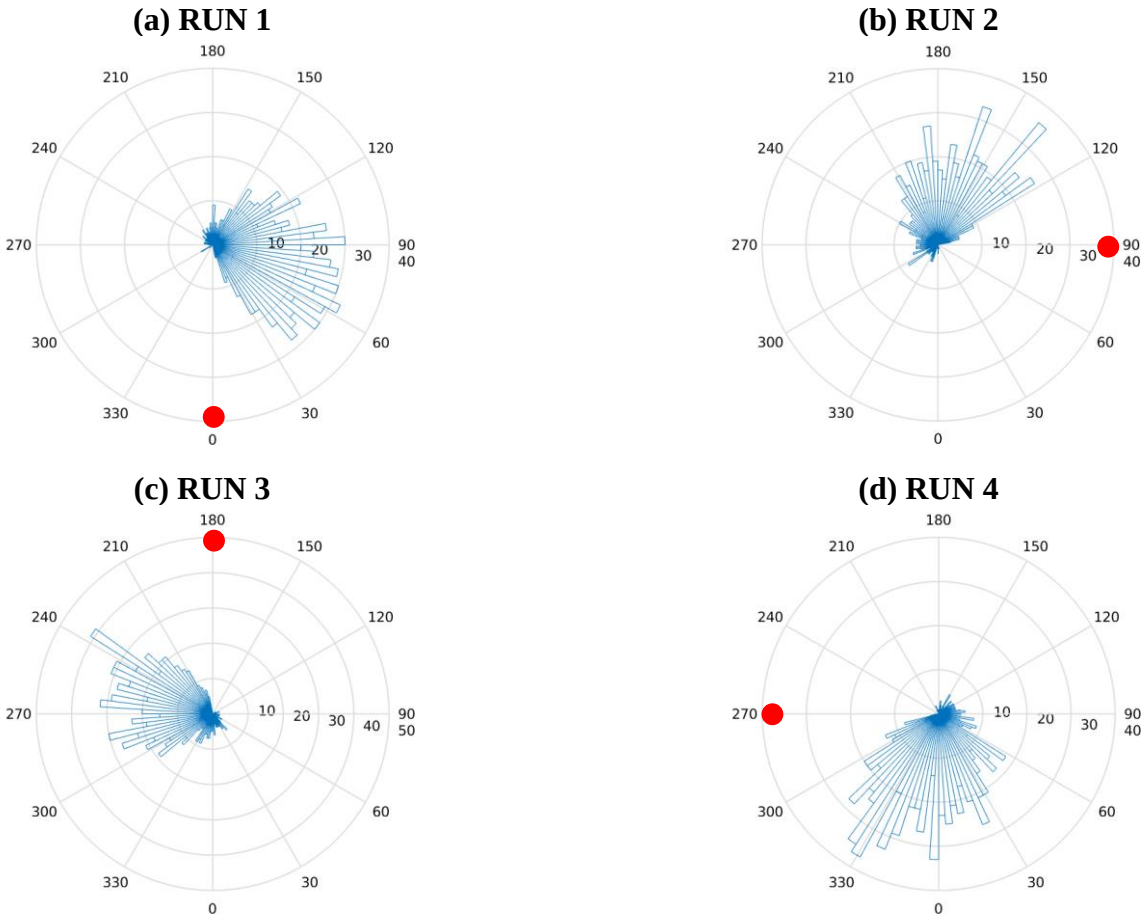

Figure 55. Polar Plots of the Number of Lunar Impacts by Longitudinal Location, Relative to Run 1 Mishap Location: (a) Run 1; (b) Run 2; (c) Run 3; (d) Run 4

5.6.4. Conclusion

A mishap in lunar orbit resulted in far greater threats to a notional spacecraft operating in the vicinity of the mishap than any of the other debris case studies examined in this research. The gravity well of the Moon causes the debris to remain within a small region following the catastrophic mishap, within which it can continue to threaten the notional spacecraft. In the other cislunar case studies, the debris expanded to fill much greater volumes immediately following the explosion. Lunar mishaps could create even more risk to a particular spacecraft than mishaps in the LEO or GEO environments due to the smaller

size of orbits around the Moon, which could give more opportunities for close approaches. The debris may also last longer in orbit due to the lack of atmospheric drag around the Moon. Future studies could utilize a more robust lunar trajectory model to analyze a variety of lunar catastrophic mishap scenarios over longer time periods to further quantify the risk of such events.

A lunar orbit catastrophic mishap causes hundreds of particles to impact the Moon's surface. These particles could cause unwanted contamination of the lunar environment or threaten future lunar infrastructure such as manned colonies. The lack of an atmosphere means that all particles would strike the lunar surface at high speeds, potentially resulting in significant clouds of dust from the disturbed lunar regolith. A future study could use a more advanced trajectory model that incorporates the non-spherical gravitational field of the Moon and the elevation of the lunar terrain to analyze lunar impacts over longer time periods.

5.7. Summary

This chapter has provided the results of five artificial debris case studies. Each case study resulted in unique risks to other cislunar spacecraft. Mishaps at the collinear Lagrange points, at the stable Lagrange points, and in the L_1 manifold resulted in slight risks to other cislunar spacecraft; a mishap during an Apollo-like transfer would pose the greatest risk to currently operational spacecraft near Earth; and a mishap in lunar orbit would pose significant risks to another spacecraft operating at the same lunar orbital altitude. In the next chapter, the overall conclusions and significance of this research are provided, along with recommendations for future research.

VI. Conclusions and Recommendations

6.1. Conclusion of Research

This research simulated the motion of debris particles in cislunar space for a variety of catastrophic spacecraft mishap scenarios and analyzed the resulting debris collision risks to spacecraft operating elsewhere in cislunar space. Using data from a prior catastrophic spacecraft mishap, the NOAA 16 battery explosion, a statistical model for the masses and velocities of debris particles released in the explosion was developed and used to simulate catastrophic spacecraft mishaps in cislunar space. The trajectories of these particles were then simulated in a four-body gravitational model to observe their motion in cislunar space. Finally, a spacecraft survivability model with a novel logistic curve model for the probability of kill with a hit was developed and applied to notional spacecraft operating elsewhere in cislunar space to quantify the risks resulting from catastrophic spacecraft mishaps in this orbital regime.

Each cislunar debris case study resulted in simulated debris risks to unique regions of cislunar space. The introductory case study of debris in the Kordylewski clouds (Section 5.2) showed slight debris collision risks to spacecraft operating at the stable Lagrange points due to natural debris accumulation. A case study of catastrophic spacecraft mishaps at the stable Lagrange points (Section 5.5) repeated this analysis for artificial debris, also finding slight risks due to debris accumulation. Both case studies found that the risk is cyclical, peaking at times when solar perturbations act to collapse the particle cloud.

The case studies of explosions at the collinear Lagrange points L_1 and L_2 (Section 5.2) and in the L_1 manifold (Section 5.4) showed risks to other regions of cislunar space due to debris that fills the L_1 manifold and moves towards the Earth or Moon. Compared to a catastrophic spacecraft mishap at L_2, A mishap at L_1 created more risk to lunar spacecraft, such as the NASA's planned Lunar Gateway space station, due to the significant number of particles that move towards the lunar region following the mishap. Although the risks to other notional cislunar spacecraft are low in each case, the debris following a mishap at either L_1 or L_2 would circulate cislunar space indefinitely due to the lack of atmospheric drag, thus potentially creating long-term debris hazards.

The case study of a catastrophic mishap while a spacecraft is on an Apollo-like transfer (Section 5.3) was unique in that it led to notable risks to spacecraft in the crowded orbits near Earth. Up to 657 particles had a final perigee after 50 days that was within GEO altitude, suggesting that these particles would intersect orbits with currently operational spacecraft at high velocities with each perigee passage. These particles would also decay very slowly due to atmospheric drag due to their extremely high apogees. This would make a debris scenario like the Apollo 13 event potentially problematic if it occurred today.

Finally, the simulation of a catastrophic spacecraft mishap in lunar orbit showed significant risks to other spacecraft in lunar orbit and potentially to infrastructure on the lunar surface. The risk of a hazardous encounter with a debris particle to a spacecraft in the same orbit as the mishap was a maximum of 0.003% over just one day. The risks would be exacerbated in an environment with many lunar spacecraft. Tracking debris particles would also be difficult or impossible, making it unlikely that a spacecraft could accurately maneuver to avoid debris. In addition, risks to the lunar surface could result from the

mishap due to the hundreds of particles that impact the Moon. These particles strike a wide region of the Moon, polluting the lunar environment or potentially threatening lunar infrastructure.

Table 20 provides a summary of all simulations conducted as part of this research.

Table 20. Summary of Cislunar Debris Simulations

Debris Scenario	Notional Spacecraft	Peak P_{HZ}	Primary Risks
Natural debris at L_4	At L_4	5.565e-8 %	Slight, cyclical collision risk
Natural debris at L_5	At L_5	5.713e-8 %	Slight, cyclical collision risk
Mishap at L_1	1) Lunar Gateway 2) At L_2 3) In L_1 Manifold	1) 3.987e-10 % 2) 4.401e-11 % 3) 6.783e-10 %	Threats to lunar orbit Accumulation in manifolds Long-lasting debris
Mishap at L_2	1) Lunar Gateway 2) At L_1 3) In L_1 Manifold	1) 9.221e-11 % 2) 1.218e-9 % 3) 2.937e-11 %	Accumulation in manifolds Long-lasting debris
Mishap during Apollo-like Transfer	N/A	N/A	Hundreds of intersections with LEO/GEO Long-lasting debris
Mishap in L_1 Manifold	At L_1	1.806e-8 %	Threats to lunar orbit Accumulation in manifolds Long-lasting debris
Mishap at L_4	At L_4	6.377e-8 %	Debris accumulation Long-lasting debris
Mishap at L_5	At L_5	4.314e-8 %	Debris accumulation Long-lasting debris
Mishap in Lunar Orbit	In Lunar Orbit	2.993e-3 %	High collision risk Debris accumulation in lunar orbit Lunar surface impacts Long-lasting debris

6.2. Significance of Research

This research has provided one of the first analyses of artificial debris beyond traditional Earth orbits, enabling an increased understanding of the debris-related consequences of spacecraft mishaps in the cislunar region. This understanding will be valuable due to the increasing number of planned missions to the Moon. The importance of keeping cislunar space free from hazardous artificial debris may begin to grow as orbits in this region become more crowded, especially with the potential for manned missions in the near future as part of NASA's Artemis Program.

The variety of cislunar debris case studies show that it may be important to consider methods for avoiding debris-generating events in cislunar mission design, especially for certain types of missions. In particular, missions to the stable Lagrange points may need to consider the use of a disposal technique following end-of-life to reduce the risk of a significant particle-generating event at L_4 or L_5, which could lead to debris accumulation at these points. Spacecraft at L_1 or L_2 may also need to be maneuvered away from these points at end-of-life to avoid debris that moves towards the Moon or that fills the manifolds of the Earth-Moon system.

This research also provided the first study of the risks to spacecraft from natural debris accumulation in the Kordylewski clouds at the stable Lagrange points. Although the risk is assessed to be low, the cyclical nature of the risk indicates that trajectories that minimize collisions with natural debris could be designed for future space missions to these points. The analysis techniques conducted in this research may be useful for re-assessing the threats from the Kordylewski clouds in the future as understanding of the density, mass, and behavior of particles in the clouds improves.

The debris analysis techniques developed in this research could be applied to study other types of catastrophic spacecraft mishaps in the future, including those in orbits closer to Earth. This research developed new techniques for debris analysis, including a statistical model for the particles generated in a catastrophic mishap, and a new survivability analysis technique with a logistic curve model for the probability of kill with a hit. This logistic curve model could be refined in the future to enable an improved modeling of the relationship between particle mass and velocity to the damage suffered by a spacecraft in a collision. These models could be applied to analyze debris risks in a wide variety of catastrophic spacecraft mishap scenarios.

6.2.1. Publications and Scholarly Efforts

The following list of publications and scholarly efforts illustrates the impactful nature of this research on the wider community.

Journal Publications

1. Boone, N. R., Bettinger, R. A., "Spacecraft Survivability in the Natural Debris Environment near the Stable Earth-Moon Lagrange Points," *Advances in Space Research,* 2021 [accepted for publication].

Conference Papers Accepted on Basis of Full Paper Review

1. Bettinger, R. A., Boone, N. R., Hamilton, N. S., Little, B. D., "Spacecraft Charging Vulnerability near the Stable Earth-Moon Lagrange Points," Paper presented at the *2021 IEEE Aerospace Conference,* Big Sky, MT, 6-13 March 2021.
2. Boone, N. R., Bettinger, R. A., "Debris Propagation Following a Catastrophic Spacecraft Mishap at the Collinear Earth-Moon Lagrange Points." Paper presented at the *2021 IEEE Aerospace Conference*, Big Sky, MT, 6-13 March 2021.

Conference Papers Accepted on Basis of Abstract Review

1. Boone, N. R., Bettinger, R. A., "Cislunar Debris Propagation Following a Catastrophic Spacecraft Mishap." Paper presented at the *2021 AIAA Science and Technology Forum and Exposition*, Nashville, TN, 11-15 January 2021.
2. Boone, N. R., Bettinger, R. A., "Spacecraft Survivability near the Stable Earth Lagrange Points." Paper presented at the *2020 AAS/AIAA Astrodynamics Specialist Conference*, Lake Tahoe, CA, 9-12 August 2020.

Scholarly Presentations

1. Boone, N., Bettinger, R. A., "Debris Propagation Following a Catastrophic Mishap in Lunar Orbit," Presented at the *46th AIAA Dayton-Cincinnati Aerospace Sciences Symposium (DCASS)*, Dayton, OH, March 2021.

6.3. Recommendations for Future Research

The analysis conducted in the present research could be improved or expanded with follow-on research. The presently limited number of studies of cislunar debris leave many relatively unexplored topics, and recommendations for future research include:

1. Expand the probability of kill with a hit model to include both particle mass and particle velocity in determining the potential to destroy a spacecraft. For the artificial debris simulations, the present study included only particle mass as a factor in calculating the probability of kill with a hit. Adding particle velocity would lead to a more accurate measure of the probability of hazard.
2. Simulate debris particles for a longer time period, observing the motion of debris over years or decades following the catastrophic spacecraft mishap. Simulating

debris particle motion over longer time periods may provide insight into stable orbits where debris would tend to accumulate or increase understanding of the longevity of cislunar debris. This research could also analyze how long it will take debris that has exited the Earth-Moon system to return to the system. The results of this research could also be used to infer the possible current orbits of fragments from the Apollo 13 disaster.

3. Conduct additional case studies with different orbit types or different notional spacecraft. New case studies that could be examined include catastrophic mishaps in a NRHO or other types of halo orbits, in GEO graveyard orbits, in a stable Distant Retrograde Orbit around the Moon, or in highly elliptical Earth orbits.
4. Vary the type of initial catastrophic spacecraft mishap to observe how the resulting debris distribution changes for a variety of cislunar orbits. The catastrophic mishaps studied could include fuel tank explosions, satellite collisions, and ASAT tests.
5. Analyze options for end-of-life disposal of cislunar spacecraft. Proper end-of-life disposal of cislunar spacecraft could help reduce the risk of debris hazards in cislunar space. Based on the research from Section 5.5 on debris at the stable Earth-Moon Lagrange points, proper disposal of spacecraft operating at these points after mission completion should be considered to avoid debris accumulation. In addition, stable regions of cislunar space that are optimal for long-term storage of debris or hazardous waste could be investigated in future studies. The validity of selected debris disposal orbits could be verified by simulating a catastrophic spacecraft mishap in those orbits and verifying that debris does not create hazards to other spacecraft.

6. Conduct a full analysis of debris in lunar orbits. The study of a catastrophic mishap in lunar orbit presented in Section 5.6 was limited and included neither the non-spherical nature of the Moon's gravity field nor the elevation of the lunar terrain, which would be important factors in low lunar orbits. Minimal prior research exists on the dynamics or management of debris in lunar orbit, and studies of this nature may become useful as lunar orbit becomes more crowded. A study of debris in lunar orbit would provide information about how long it takes for space debris to decay to the lunar surface in the absence of atmospheric drag, where on the lunar surface debris particles would be most likely to strike, and methods for disposal of spacecraft at end-of-life. Disposal techniques for injecting spacecraft into a lunar graveyard orbit or directing spacecraft towards a certain disposal region on the lunar surface could be developed to support future lunar debris management.
7. Improve understanding of the Kordylewski clouds at L_4 and L_5 by modeling the mass flux into and out of the Earth-Moon system. This would provide increased insight into the true particle density of these clouds and their behavior over time.
8. Simulate a significant number of particles distributed throughout cislunar space to identify stable regions that are likely locations for accumulations for natural or artificial debris. The results of this study could be used to identify regions of cislunar space with increased debris risk or cislunar orbits that could be useful for long-term debris disposal.
9. Study tracking of cislunar debris and the risks from operating in an environment where debris particles cannot be tracked accurately. Examine strategies for cislunar debris avoidance.

10. Simulate a full counterspace campaign in cislunar space. Model the catastrophic spacecraft mishap as a collision between multiple interceptors and multiple, notional resident objects in cislunar space, then model the motion of the resulting debris and determine the threats to other spacecraft.
11. Analyze interplanetary debris, such as debris in Mars orbits. Debris in Martian orbit could be a useful topic due to the increased exploration of Mars expected in the coming years, and the gravitational influence of the two Martian moons could lead to unique behavior following a catastrophic spacecraft mishap.

Bibliography

[1] David, Leonard. "US Military Eyes Strategic Value of Earth-Moon Space," *Space.com*, 29 August 2019. URL https://www.space.com/us-military-strategic-value-earth-moon-space.html.

[2] Kelso, T. "Analysis of the 2007 Chinese ASAT Test and the Impact of its Debris on the Space Environment." Paper presented at the *8th Advanced Maui Optical and Space Surveillance Technologies Conference*, Maui, Hawaii, 12-15 September 2007.

[3] Henry, C. "India ASAT debris spotted above 2,000 kilometers, will remain a year or more in orbit," *SpaceNews*, 9 April 2019. URL https://spacenews.com/india-asat-debris-spotted-above-2200-kilometers-will-last-a-year-or-more/.

[4] Braun, V., S. Lemmens, B. Reihs, H. Krag, and A. Horstmann. "Analysis of Breakup Events." Paper presented at the *7th European Conference on Space Debris*, Darmstadt, Germany, 18-21 April 2017.

[5] Kessler, Donald J. and Burton G. Cour-Palais. "Collision Frequency of Artificial Satellites: The Creation of a Debris Belt," *Journal of Geophysical Research* 83, no. A6: 2637–2646 (1978).

[6] Namazyfard, Hossein. "Computational Exploration of the Cislunar Region and Implications for Debris Mitigation." MS Thesis: Department of Aerospace Engineering, The University of Arizona, Tucson, Arizona, April 2019.

[7] Bandyopadhyay, Priyankar, Ram Krishan Sharma, Ashish Tewari. "Space Debris Hazards from Fragmentations in Collinear Earth-Moon Points." Paper

presented at the *5th European Conference on Space Debris*, Darmstadt, Germany, 30 March to 2 April 2009.

[8] Slíz-Balogh, Judit, András Barta, and Gábor Horváth, "Celestial Mechanics and Polarization Optics of the Kordylewski Dust Cloud in the Earth-Moon Lagrange Point L5, Part I: 3D Celestial Mechanical Modelling of Dust Cloud Formation," *Monthly Notices of the Royal Astronomical Society* 480: 5550-5559 (2018).

[9] Meirovitch, Leornard. *Methods of Analytical Dynamics*. Mineola, NY: Dover Publications, 2007.

[10] Huang, Su-Shu. "Very Restricted Four-Body Problem," *NASA TN D-501*. Goddard Space Flight Center, Washington D.C.: National Aeronautics and Space Administration, 1960.

[11] Koon, Wang Sang, Martin W. Lo, Jerrold E. Marsden, and Shane D. Ross. *Dynamical Systems, the Three-Body Problem, and Space Mission Design*. Springer, 2007.

[12] Davis, Diane C., Kenza K. Boudad, Sean M. Phillips, and Kathleen C. Howell. "Disposal, Deployment, and Debris in Near Rectilinear Halo Orbits." Paper presented at the *29th AAS/AIAA Space Flight Mechanics Meeting*, Ka'anapali, Maui, Hawaii, 13-17 January 2019.

[13] Boudad, Kenza Katiane. "Disposal Dynamics from the Vicinity of Near Rectilinear Halo Orbits in the Earth-Moon-Sun-System." MS Thesis: Department of Aeronautics and Astronautics, Purdue University, West Lafayette, Indiana (2018).

[14] Salnikova, T.V., S. Ya. Stepanov. “Mathematical Model of Formation of Kordylewski Cosmic Dust Clouds,” *Doklady Physics* 60, no. 7: 323-326 (2015).

[15] Kawakatsu, Yasuhiro. “Study on the Characteristics of Two-burn Translunar Trajectory,” *Transactions of the Japan Society for Aeronautical and Space Sciences, Space Technology Japan* 5: 9-15 (2007).

[16] Kawakatsu, Yasuihiro, Ken Nakajima, Masahiro Ogasawara, Yutaka Kaneko, and Yoshisada Takizawa. “SELENE Translunar Trajectory and Lunar Orbit Injection,” *Acta Astronautica* 47, nos. 2-9: 467-473 (2000).

[17] Ostman, Joshua A. “Cislunar Trajectory Generation with Sun-Exclusion Zone Constraints Using a Genetic Algorithm and Direct Method Hybridization.” MS Thesis, AFIT-ENY-MS-19-S-081. School of Engineering and Management, Air Force Institute of Technology (AU), Wright-Patterson AFB, OH, August 2019. (AD1083338)

[18] Parker, Jeffrey S. and Rodney L. Anderson. *Low-Energy Lunar Trajectory Design*. Hoboken, NJ: Wiley, 2014.

[19] Luu, Kim and Chris Sabol. “Effects of Perturbations on Space Debris in Supersynchronous Storage Orbits.” *AFRL-VS-PS-TR-1998-1093*. Kirtland Air Force Base, New Mexico: Air Force Research Laboratory Space Vehicles Directorate, 1998.

[20] Friesen, Larry J., Albert A. Jackson, Herbert A. Zook, and Donald J. Kessler. “Results in Orbital Evolution of Objects in the Geosynchronous Region,” *Journal of Guidance, Control, and Dynamics* 15, no. 1: 263-267 (1992).

[21] Rosengren, Aaron J., Daniel J. Scheeres, and Jay W. McMahon. “The Classical Laplace Plane as a Stable Disposal Orbit for Geostationary Satellites,” *Advances in Space Research* 53, no. 8: 1219-1228 (2014).

[22] Xu, Luyuan. “Chang'e 4 relay satellite, Queqiao: A bridge between Earth and the mysterious lunar farside.” URL https://www.planetary.org/blogs/guest-blogs/2018/0519-change-4-relay-satellite.html

[23] Dejevsky, Mary. “Far side of the moon: China's Chang'e 4 probe makes historic touchdown.” URL https://www.theguardian.com/science/2019/jan/03/china-probe-change-4-land-far-side-moon-basin-crater

[24] Liang, Yuying, Ming Xu, and Shijie Xu. “The Classification of Cislunar Trajectories and its Applications in the Earth-Moon System,” *Astrophysics and Space Science* 361, no. 1 (2016).

[25] Davis, Diane C., Sean M. Phillips, Kathleen C. Howell, Srianish Vutukuri, and Brian P. McCarthy. “Stationkeeping and Transfer Trajectory Design for Spacecraft in Cislunar Space.” Paper presented at the *2017 AAS/AIAA Astrodynamics Specialist Conference*, Columbia River Gorge, Stevenson, WA, 20-24 August 2017.

[26] Li, Weipeng, Hai Huang, and Fujun Peng. “Trajectory Classification in Circular Restricted Three-Body Problem Using Support Vector Machine,” *Advances in Space Research* 56, no. 2: 273-280 (2015).

[27] Dahlke, Jacob A. “Optimal Trajectory Generation in a Dynamic Multi-Body Environment Using a Pseudospectral Method.” MS Thesis: AFIT-ENY-MS-18-

M-248. School of Engineering and Management, Air Force Institute of Technology (AU), Wright-Patterson AFB, OH, March 2018. (AD1056557)

[28] Aravind R., Saurabh Harsh, and Priyankar Bandyopadhyay. "Mission to Retrograde Geo-equatorial Orbit (RGEO) Using Lunar Swing-by." Paper presented at the *2012 IEEE Aerospace Conference*, Big Sky, Montana, 3-10 March 2012.

[29] Brick, John N. "Military Space Mission Design and Analysis in a Multi-Body Environment: An Investigation of High-Altitude Orbits as Alternative Transfer Paths, Parking Orbits for Reconstitution, and Unconventional Mission Orbits." MS Thesis, AFIT-ENY-MS-17-M-246. School of Engineering and Management, Air Force Institute of Technology (AU), Wright-Patterson AFB, OH, March 2017. (AD1040181)

[30] Casoliva, Jordi, Josep M. Mondelo, Benjamin F. Villac, Kenneth D. Mease, Esther Barrabes, and Merce Olle. "Families of Cycler Trajectories in the Earth-Moon System." Paper presented at the *AIAA/AAS Astrodynamics Specialist Conference and Exhibit*, Honolulu, Hawaii, 18-21 August 2008.

[31] Collins, Alexander R. and Kirk W. Johnson. "Development of Cislunar Space Logistics Networks for Satellite Constellation Support Using Event-Driven Generalized Multi-Commodity Network Flows." Paper presented at the *AIAA SciTech 2020 Forum*, Orlando, Florida, 6-10 January 2020.

[32] Pan, Xiao, Ming Xu, and Ramil Santos. "Trajectory Optimization for Solar Sail in Cislunar Navigation Constellation with Minimal Lightness Number," *Aerospace Science and Technology* 17: 559-567 (2017).

[33] Jones, Brian L. “A Guidance and Navigation System for Two Spacecraft Rendezvous in Translunar Halo Orbit.” Ph.D Dissertation: The University of Texas at Austin, Austin, Texas, 1993.

[34] Jones, Brain L. and Robert H. Bishop. “Rendezvous Targeting and Navigation for a Translunar Halo Orbit,” *Journal of Guidance, Control, and Dynamics* 17, no. 5: 1109-1114 (1994).

[35] Whitley, Ryan and Roland Martinez. “Options for Staging Orbits in Cislunar Space.” Paper presented at the *2016 IEEE Aerospace Conference,* Big Sky, Montana, 5-12 March 2016.

[36] McGuire, Melissa L., Laura M. Burke, Kurt J. Hack, Nathan J. Strange, Timothy P. McElrath, Daman F. Landau, Gregory Lantoine, and Pedro Lopez. “Potential Cislunar and Interplanetary Proving Ground Excursion Trajectory Concepts.” Paper presented at the *2016 IEEE Aerospace Conference*, Big Sky, Montana, 5-12 March 2016.

[37] Colombo, Camilla, Francesca Letizia, Stefania Soldini, Hugh Lewis, Elisa Maria Alessi, Alessandro Rossi, Massimiliano Vasile, Massimo Vetrisano, Willem Van der Weg, and Markus Landgraf. “End-of-Life Disposal Concepts for Libration Point and Highly Elliptical Orbit Missions.” Paper presented at the *2nd Conference on Dynamics and Control of Space Systems*, Rome, Italy, 24-26 March 2014.

[38] Armellin, Roberto, P. Di Lizia, M. Rasotto, G. Di Mauro, and M. Landgraf. “Disposal Strategies for Spacecraft in Lagrangian Point Orbits.” Paper presented

at the *24th AAS/AIAA Space Flight Mechanics Meeting*, Santa Fe, New Mexico, 26-30 January 2014.

[39] Alessi, Elisa Maria, Camilla Colombo, and Markus Landgraf. "Re-Entry Disposal Analysis for Libration Point Orbit Mission." Paper presented at the *24th International Symposium on Space Flight Dynamics*, Laurel, Maryland, 5-9 May 2014.

[40] Andreu, M.A., "New Results on Computation of Translunar Halo Orbits of the Real Earth-Moon System," *Libration Point Orbits and Applications*: 225-237 (2003).

[41] Jorba-Cuscó, Marc, Ariadna Farrés and Àngel Jorba. "Two Periodic Models for the Earth-Moon System," *Frontiers of Applied Mathematical Statistics* 4, no. 32: 2018.

[42] Wen, Xin, Wenhao Zhang, Laohu Yuan, Jiafu Liu, and Wei Li. "A Neural Networks Controller for Mixed Formation of Satellites and Space Debris." Paper presented at the *2015 Fifth International Conference on Instrumentation and Measurement, Computer, Communication and Control*, Qinhuangdao, China, 18-20 September 2015.

[43] Ren, Yuan and Jinjun Shan. "Low-Energy Lunar Transfers Using Spatial Transit Orbits," *Communications in Nonlinear Science and Numerical Simulation* 19, no. 3: 554-569 (2014).

[44] Xu, Ming, Yan Wei, and Shijie Xu. "On the Construction of Low-Energy Cislunar and Trans-lunar Transfers Based on the Libration Points," *Astrophysics and Space Science* 348, no. 1: 65-88 (2013).

[45] Burbank, Paige B., Burton G. Cour-Palais, and William E. McAllum. “A Meteoroid Environment for Near-Earth, Cislunar, and Near-Lunar Operations,” *NASA TN D-2747*. Houston, Texas: National Aeronautics and Space Administration, 1965.

[46] Davidson, John R. and Paul E. Sandorff. “Environmental Problems of Space Flight Structures: II. Meteoroid Hazard,” *NASA TN D-1493*. Langley Station, Hampton, Virginia: NASA Langley Research Center, 1963.

[47] Singer, S.F. “Interplanetary Dust Near the Earth,” *Nature* 192, no. 4800: 321-323 (1961).

[48] Hyde, T.W. and W.M. Alexander. “Transport Dynamics Calculated Under the Full Mie Scattering Theory for Micron and Submicron Lunar Ejecta in Selenocentric, Cislunar, Geocentric Space.” Paper presented at the *19th Lunar and Planetary Science Conference*, Houston, Texas, 14-18 March 1988.

[49] Altobelli, N., E. Grün, and M. Landgraf. “A New Look into the Helio Dust Experiment Data: Presence of Interstellar Dust Inside the Earth’s Orbit,” *Astronomy and Astrophysics* 448: 243-252 (2006).

[50] Taylor, Michael W. “Orbital Debris: Technical and Legal Issues and Solutions.” LL.M Thesis: Institute of Air and Space Law Faculty of Law, McGill University, Montreal, Canada, August 2016.

[51] Johnson, Nicholas L. “A New Look at the GEO and Near-GEO Regimes: Operations, Disposals, and Debris.” Paper presented at the *62nd International Astronautical Congress*, Cape Town, South Africa, 3-7 October 2011.

[52] Keay, C.S. L. “Pollution Potentials in Interplanetary Space,” *Advances in Space Research* 21, no. 11: 1603-1606 (1998).

[53] Friedlander, Alan. “Disposal Methods.” Paper presented at *Nuclear Thermal Propulsion: A Joint NASA (DOE) DOD Workshop*, NASA Lewis Research Center, Cleveland, Ohio, January 1991.

[54] Salnikova, T. and S. Stepanov. “Existence of the Elusive Kordylewski Cosmic Dust Clouds,” *Acta Astronautica* 163, Part A: 138-141 (2019).

[55] Pohle, Frederick V. “The Least Density of a Spherical Swarm of Particles, with an Application to Astronomical Observations of K. Kordylewski,” *MRC Technical Summary Report #351*. Madison, Wisconsin: Mathematics Research Center, United States Army, The University of Wisconsin, 1962.

[56] Pohle, Frederick V. “A Dynamical Model for Kordylewski Cloud Satellites,” *AIAA Journal* 2, no. 10: 1818-1820 (1964).

[57] Salnikova, T.V., S. Ya. Stepanov, and A. I. Shuvalova. “Probabilistic Model of Kordylewski Clouds,” *Doklady Physics* 61, no. 5: 243-246 (2016).

[58] Salnikova, Tatiana and Sergey Stepanov. “On the Kordylewski Cosmic Dust Clouds.” Paper presented at the *2016 International Conference “Stability and Oscillations of Nonlinear Control Systems” (Pyatnitskiy’s Conference)*, Moscow, Russia, 1-3 June 2016.

[59] Slíz-Balogh, Judit, András Barta, and Gábor Horváth, “Celestial Mechanics and Polarization Optics of the Kordylewski Dust Cloud in the Earth-Moon Lagrange Point L5, Part II: Imaging Polarimetric Observation: New Evidence for the

Existence of the Kordylewski Dust Cloud," *Monthly Notices of the Royal Astronomical Society* 482: 762-770 (2019).

[60] Landgraf, M. and R. Jehn. "Space Debris Hazards from Explosions in the Collinear Sun-Earth Lagrange Points." Paper presented at the *Third European Conference on Space Debris*, Darmstadt, Germany, 19 - 21 March 2001.

[61] Ball, Robert E. *The Fundamentals of Aircraft Combat Survivability Analysis and Design*. AIAA (American Institute of Aeronautics & Astronautics), 2003.

[62] Ball, Robert E. "Combining Safety and Survivability for Future Spacefaring," *Aerospace America* 10, no. 48: 16-20 (2010).

[63] Bettinger, Robert A. and Joshuah A. Hess. "Fractionated Spacecraft Survivability following a Catastrophic Explosion." Paper presented at the *AIAA SciTech 2020 Forum*, Orlando, Florida, 6-10 January 2020.

[64] Chobotov, V. A. and D. B. Spencer. "Debris Evolution and Lifetime Following an Orbital Breakup," *Journal of Spacecraft and Rockets* 28, no. 6: 670-676 (1991)

[65] Dickey, Michael R. and Robert D. Culp. "Determining Characteristic Mass for Low-Earth-Orbiting Debris Objects," *Journal of Spacecraft and Rockets* 26, no. 6: 460-464 (2012).

[66] "NOAA 16 Satellite Breakup Leaves Dozens of Debris in Orbit," *SpaceFlight 101*, 5 December 2019. URL https://spaceflight101.com/noaa-16-satellite-breakup-leaves-dozens-of-debris-in-orbit/

[67] Elvidge, Michael E. "A Stochastic Method for Calculating Spacecraft Vulnerability to Low Earth Orbit Debris." MS Thesis: Department of

Mechanical and Aerospace Engineering, Ottawa-Carleton Institute for Mechanical and Aerospace Engineering, Ottawa, Canada, August 1994.

[68] Yasaka, Tetsuo, Toshiya Hanada, and Hiroshi Hirayama. "Low-Velocity Particle Impact on Spacecraft," *Acta Astronautica* 47, No. 10: 763-770 (2000).

[69] Alhamzi, Omar H. and Yashwant K. Malaiaya. "Prediction Capabilities of Vulnerability Discovery Models." Paper presented at the *2006 Reliability and Mainatainability Symposium*, Newport Beach, CA, 23-26 January 2006.

[70] Okamura, Hiroyuki, Masataka Tokuzane, and Tadashi Dohi. "Optimal Security Patch Release Timing Under Non-Homogeneous Vulnerability-Discovery Processes." Paper presented at the *20th International Symposium on Software Reliability Engineering*, Karnataka, India, 16-19 November 2009.

[71] Lee, Seongkwan Mark, Tschangho John Kim, and Seung Lim Kang. "Development of Fragility Curves for Bridges in Korea," *KSCE Journal of Civil Engineering* 11, No. 3: 165-174 (2007).

[72] Bangerjee, S. and M. Shinozuka. "Nonlinear Static Procedure for Seismic Vulnerability Assessment of Bridges," *Computer-Aided Civil and Infrastructure Engineering* 22, No. 4: 293-305 (2007).

[73] Brandt-Erichsen, David. "Brief History of the L5 Society," *National Space Society*, 1994. URL https://space.nss.org/brief-history-of-the-l5-society/

[74] Kaplan, Spencer. *Eyes on the Prize: The Strategic Implications of Cislunar Space and the Moon*. Center for Strategic & International Studies, 2020.

[75] Xu, Ming, Jinlong Wang, Shengli Liu, Shijie Xu. "A New Constellation Configuration Scheme for Communicating Architecture in Cislunar Space," *Mathematical Problems in Engineering* (2013).

[76] Lee, Sanguk, Jae Hoon Kim, and Seong-Pal Lee. "Communications Satellite System by using Moon Orbit Satellite Constellation," *Journal of Astronomy & Space Sciences* 20, no. 4: 313-318 (2003).

[77] McKnight, Darren S. and Frank R. Di Pentino. "New Insights on the Orbital Debris Collision Hazard at GEO," *Acta Astronautica* 85: 73-82 (2013).

[78] Mars, Kelli. "More About Gateway," NASA.gov, 18 August 2020. URL https://www.nasa.gov/johnson/exploration/gateway.

[79] Foust, Jeff. "NASA Cubesat to Test Lunar Gateway Orbit," *SpaceNews.com*, 16 September 2020. URL https://spacenews.com/nasa-cubesat-to-test-lunar-gateway-orbit/.

[80] Williams, Jacob, David Lee, Ryan Whitley, Kevin Bokelmann, Diane Davis, and Christopher Berry. "Targeting Cislunar Near Rectilinear Halo Orbits for Human Space Exploration." Paper presented at the *27th AAS/AIAA Space Flight Mechanics Meeting*, San Antonio, Texas, 5-9 February 2017.

[81] Garcia, Mark. "Space Debris and Human Spacecraft," NASA.gov, 26 September 2013. URL https://www.nasa.gov/mission_pages/station/news/orbital_debris.html

[82] Dunbar, Brian, "Apollo 13," NASA.gov, July 2009, https://www.nasa.gov/mission_pages/apollo/missions/apollo13.html

[83] Keel, William C., “Telescopic Tracking of the Apollo Lunar Missions,” Bill Keel’s Space Bits, Department of Physics and Astronomy at the University of Alabama, https://pages.astronomy.ua.edu/keel/space/apollo.html

[84] Riché, L. J., G. M. Colton, and T. A. Guillory. *Apollo 11 Flight Plan*. Houston, Texas: National Aeronautics and Space Administration, Manned Spaceflight Center, 1969.

[85] Healy, Liam, Scott Kindl, Christopher Binz. “Spatial Density Maps from a Debris Cloud.” Paper presented at the *17th Advanced Maui Optical and Space Surveillance Technologies Conference*, Maui, Hawaii, 20-23 September 2016.